

# Reading Report

## *Photocatalytic Ammonia Synthesis from Nitrate Using InP Quantum Dots Under Visible Light Irradiation*

under the Guidance of Prof. Pramod Pilai

Agam Baruah

09 May 2025 to 24 July 2025

### Abstract

This report explores a novel visible light-driven strategy for sustainable ammonia ( $\text{NH}_3$ ) synthesis using surface-engineered Indium phosphide (InP) quantum dots (QDs) as photocatalysts. The key objective is to selectively reduce nitrate ( $\text{NO}_3^-$ ) to ammonia under ambient conditions, addressing the limitations of conventional UV-based systems and competing hydrogen evolution reactions (HER). Trimethylammonium (TMA) ligands on InP QDs create an electrostatically favorable microenvironment that enhances nitrate adsorption and suppresses HER by managing local proton availability. Under 450 nm irradiation, the system achieves 94%  $\text{NH}_3$  selectivity within two hours, with apparent quantum yields of 1.45% for nitrate and 3.7% for nitrite reduction. The nitrate to nitrite step is identified as the rate-determining step. Isotope-labeling studies with  $^{15}\text{NO}_3^-$  and  $\text{D}_2\text{O}$  confirm water as the sole proton source. Under natural sunlight, the system produced  $91 \pm 30 \mu\text{M}$   $\text{NH}_3$  with  $26.5 \pm 7.7\%$  nitrate conversion, demonstrating practical viability. This approach offers a promising route to decentralized, lower-emission ammonia production. Further improvements in quantum efficiency, surface engineering, and process design could position InP QD-based photocatalysis as a viable alternative to the Haber Bosch process.

**Keywords:** Photocatalysis, Nitrate Reduction, Quantum Dots, InP, Ammonia Synthesis

## Contents

<b>1</b>	<b>Introduction</b>	<b>1</b>
1.1	Context and Importance . . . . .	1
1.2	Current Challenges and Knowledge Gaps . . . . .	2
1.3	QDs as Photocatalysts . . . . .	2
1.4	Reaction Mechanism . . . . .	3
1.5	Surface Modification of QDs . . . . .	4
1.6	Core/Shell InP/ZnS QDs . . . . .	4
1.7	Objective and Significance . . . . .	5
<b>2</b>	<b>Methods</b>	<b>5</b>
2.1	Photocatalytic Light Source Setup . . . . .	6
2.1.1	Light Sources . . . . .	6
2.1.2	Reactor . . . . .	6
2.1.3	Intensity & Power: Calculation and Measurement . . . . .	6
2.1.4	Challenges . . . . .	6
2.1.5	Key Steps . . . . .	7
2.2	Post Reaction Analysis . . . . .	7
2.2.1	Quantization of Ammonia . . . . .	7
2.2.2	Optimization of Reaction Parameters . . . . .	7
2.3	Temperature Effects in Photocatalysis . . . . .	9
2.3.1	Optimization of Temperature . . . . .	9
2.3.2	Relevance to Global Warming . . . . .	10
<b>3</b>	<b>Result And Discussion</b>	<b>10</b>
3.1	Determination of Band Position of InP QDs . . . . .	10
3.2	Electrostatic Channeling by QDs . . . . .	11
3.3	Control experiments . . . . .	11
3.4	Photocatalytic Experiments with Isotope-Labeled Nitrate . . . . .	11

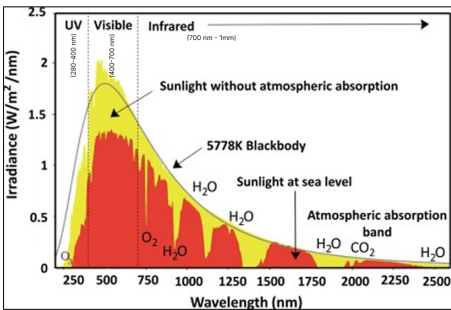
3.5	Mass Spectrometric (MS) Analysis . . . . .	12
3.5.1	Quantization of Ammonia in the Gas Phase . . . . .	12
3.5.2	Isotopic Labeling . . . . .	12
3.6	Optimized Photocatalytic Ammonia Synthesis with InP QDs . . . . .	12
3.6.1	Optimized Reaction Conditions . . . . .	12
3.7	Sunlight-Driven Ammonia Synthesis with InP QDs . . . . .	13
3.7.1	Action Spectrum . . . . .	13
3.7.2	Photocatalytic Experiments in Sunlight . . . . .	13
3.8	Side Product Analysis . . . . .	14
3.8.1	Gaseous side-products . . . . .	14
3.8.2	Colorimetric Analysis for Organic Nitrogen Compounds . . . . .	15
3.9	Rate-determining step . . . . .	17
3.9.1	Using Nitrite as the Starting Material . . . . .	17
3.9.2	Competitive Reaction . . . . .	17
3.9.3	Isotopic Competition . . . . .	18
3.9.4	Conclusion . . . . .	18
3.10	Understanding HER as a Competing Reaction in Photocatalytic Ammonia Synthesis . . . . .	18
3.10.1	Does HER Improve the Photocatalytic Conversion? . . . . .	18
3.10.2	Further Studies . . . . .	20
3.11	Proton Source Identification . . . . .	20
3.11.1	TMA Ligands on QDs . . . . .	21
3.11.2	Water . . . . .	21
3.12	Photocatalytic Stability of [+]InP QDs . . . . .	23
3.12.1	Time-Dependent UV-Visible Absorption Study . . . . .	23
3.12.2	X-Ray Photoelectron Spectroscopy (XPS) Analysis . . . . .	23
3.13	Recyclability in QD Systems . . . . .	24
3.13.1	With Core-Only InP QDs . . . . .	24
3.13.2	With Core/Shell InP QDs . . . . .	25
3.14	Proposed Reaction Mechanism . . . . .	26
3.14.1	Understanding the Operating Pathway . . . . .	26
3.14.2	Performance Comparison with Other Photocatalysts . . . . .	27
3.15	Comparative Assessment with Haber-Bosch . . . . .	27
<b>4</b>	<b>Conclusion</b> . . . . .	<b>28</b>
<b>Appendix</b>		<b>28</b>
<b>A</b>	<b>Technical Concepts and Background</b> . . . . .	<b>28</b>
A.1	Anisotropy . . . . .	28
A.2	Carrier Mobility . . . . .	28
A.3	Classes of QDs . . . . .	29
A.4	Core-only QDs . . . . .	29
A.5	Effective Mass . . . . .	29
A.6	Growth of QDs . . . . .	29
A.7	Haber-Bosch Process . . . . .	30
A.8	Long-lived Charge Separation . . . . .	30
A.9	Magic-Sized Clusters (MSCs) . . . . .	30
A.10	Molar Extinction Coefficient . . . . .	31
A.11	Nucleation . . . . .	31
A.12	Photostability . . . . .	31
A.13	Quantum Dots (QDs) . . . . .	31
A.14	Quantum Efficiency . . . . .	31
A.15	Relation between Electronegativity and Charge Separation . . . . .	32
A.16	Retention . . . . .	32
A.17	Surface Chemistry Tunability . . . . .	32
A.18	Tunable Electronic Properties . . . . .	33
A.19	Valence Bond Theory . . . . .	33

<b>B Analytical and Instrumental Techniques</b>	<b>33</b>
B.1 Electrochemical Setup For Determination of Band Positions . . . . .	33
B.2 Fourier Transform Infrared Spectroscopy (FTIR) . . . . .	33
B.2.1 Basic Principles of FTIR . . . . .	33
B.3 Gas Chromatography . . . . .	33
B.3.1 Principle . . . . .	33
B.3.2 Key Components . . . . .	33
B.3.3 Thermal Conductivity Detector (TCD) . . . . .	33
B.4 Glutamate dehydrogenase (GLDH) Assay . . . . .	34
B.4.1 Mechanism . . . . .	34
B.4.2 Components and Their Roles . . . . .	34
B.4.3 NADH . . . . .	34
B.4.4 alpha-Ketoglutarate . . . . .	34
B.4.5 Analysis . . . . .	34
B.5 <sup>1</sup> H-NMR Spectroscopy . . . . .	35
B.6 Ion Chromatography (IC) . . . . .	35
B.7 Mass Spectrometric (MS) Analysis . . . . .	36
B.8 X-ray Photoelectron Spectroscopy (XPS) . . . . .	36
B.8.1 Fundamental Principles . . . . .	36
B.8.2 Instrumentation . . . . .	37
B.8.3 Analysis . . . . .	37
<b>C Experimental Supplements</b>	<b>37</b>
C.1 Calculations for the Determination of Band Positions . . . . .	37
C.2 Boltzmann Distribution and Ion Concentration Theory . . . . .	38
C.3 Errors and Corrections . . . . .	39
C.4 Materials and Reagents . . . . .	39
C.4.1 InCl . . . . .	39
C.4.2 ZnCl . . . . .	40
C.4.3 Tris(dimethylamino)phosphine . . . . .	40
C.4.4 Oleylamine . . . . .	40
C.4.5 11-Mercaptoundecanoic acid (MUA) . . . . .	40
C.4.6 Potassium nitrate . . . . .	40
C.4.7 TMA . . . . .	40
C.5 Synthesis of Red Emitting InP Core QDs . . . . .	41
C.5.1 Mixing Procedure . . . . .	41
C.5.2 Reaction at High Temperature . . . . .	41
C.5.3 Quenching and Purification . . . . .	41
C.6 Ligand Exchange for Aqueous Dispersion . . . . .	41
C.6.1 Objective . . . . .	41
C.6.2 Procedure for [+]InP QDs . . . . .	41
C.6.3 Procedure for [-]InP QDs . . . . .	42
C.7 Quantum Yield Calculations . . . . .	43

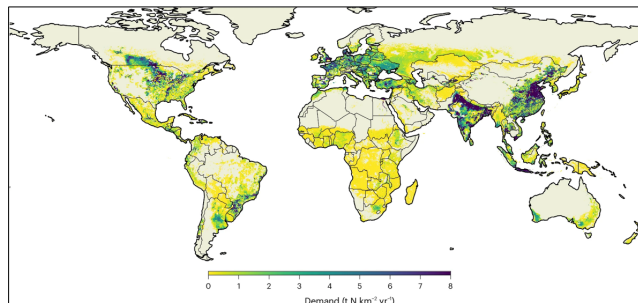
# 1 Introduction

## 1.1 Context and Importance

Ammonia ( $\text{NH}_3$ ) is an essential industrial chemical, mainly as fertilizer<sup>69</sup>, with global demand above 190 million metric tons in 2023 and projected to reach 200 Mt by 2030 due to population growth<sup>42</sup>(see 1b). Industrial  $\text{NH}_3$  is mainly produced via the energy- and carbon-intensive Haber-Bosch process (A.7), which emits 1.6–2.0 tons of  $\text{CO}_2$  per ton of  $\text{NH}_3$  due to fossil fuel-based hydrogen and is a major point source of greenhouse gases. Thus, it becomes crucial to develop sustainable, low-energy, and low-carbon alternatives for  $\text{NH}_3$  synthesis. It is not only a scientific challenge, but also a critical societal challenge. While the conventional Haber-Bosch process produces  $\text{NH}_3$  at an energy cost of approximately \$195–\$197 per tonne using natural gas, emerging green methods such as chemical looping or photocatalysis aim to reduce costs further, with some projections as low as \$153 per tonne, though practical implementation remains challenging. (See Appendix A for technical terms and background concepts.)



(a)



(b)

Figure 1: (a) Spectral distribution of solar radiation at the Earth’s surface, showing the relative intensity across UV, visible, and IR regions. (b) Geographic distribution of nitrogen fertilizer demand in 2023, highlighting regions with the highest agricultural NH<sub>3</sub> consumption. The map uses color coding to indicate demand intensity (million tonnes/year). This rising demand underlines the urgent need for sustainable and decentralized NH<sub>3</sub> production routes.

## 1.2 Current Challenges and Knowledge Gaps

The conversion of NO<sub>3</sub><sup>-</sup> and NO<sub>2</sub><sup>-</sup> to NH<sub>3</sub> has gained significant attention in recent years due to the following reasons:

1. It emerges as a vital source for NH<sub>3</sub> synthesis.
2. It offers a method of wastewater treatment for water bodies contaminated with nitrogen.
3. It provides an opportunity for local fertilizer production in regions with high NO<sub>3</sub><sup>-</sup> and NO<sub>2</sub><sup>-</sup> contamination and fertilizer demand.

Due to the surplus availability of solar energy, light-assisted synthesis from nitrate and nitrite sources is a promising approach. However, there are two bottlenecks:

1. Many known existing photocatalysts are UV-spectrum-dependent, rather than visible light-dependent, due to their large energy bandgap. But the solar energy reaching Earth is predominantly in the visible range (42.3%)<sup>20</sup>, and only a small fraction is in the UV range (8%)(see 1a). This makes the process inefficient for real-world applications, limiting its practicality. These values are based on the ASTM G173-03 standard reference spectra. Additionally, UV light sources are less energy efficient and cause material degradation over time, which limits the scalability of the model for industrial ammonia production. Hence, there is a pressing need to develop visible light active photocatalysts that align better with the solar spectrum and are scalable. The photocatalytic conversion of nitrate to ammonia using [+]InP QDs described in the report has a yield of up to 94% on being irradiated with 450 nm LED lights for 2 hours, which is quite impressive.
2. The methods discovered till now for the desired conversion are found to have poor selectivity i.e., the process inefficiently converts nitrates/nitrites to ammonia leading to accumulation of undesired byproducts such as nitrogen gas (N<sub>2</sub>), nitrous oxide (N<sub>2</sub>O), or hydrogen (H<sub>2</sub>) leading to decrease in the ammonia yield and increase in the energy and thereby cost required to separate the byproducts to get pure ammonia. This compromises the scalability and economic viability of the process. When a catalyst facilitates the conversion of nitrite or nitrate to ammonia, it requires a steady supply of protons and electrons at the surface. However, these protons and electrons often participate in the competing hydrogen evolution reaction (HER), producing hydrogen gas instead of reducing nitrogen species. Since HER is both kinetically favorable and thermodynamically easier, it significantly reduces the yield of ammonia, thereby lowering the overall efficiency of the process. A comprehensive discussion of the mechanistic details and selectivity challenges, including the role of competing hydrogen evolution reactions (HER), is provided in subsection 4.11<sup>8,49,55,61</sup>.

These challenges highlight the need for rationally designed visible light photocatalysts for efficient and selective NH<sub>3</sub> formation from NO<sub>3</sub><sup>-</sup> and NO<sub>2</sub><sup>-</sup>.

## 1.3 QDs as Photocatalysts

QDs can be used as visible light photocatalysts for the conversion of NO<sub>2</sub><sup>-</sup>/NO<sub>3</sub><sup>-</sup> to NH<sub>3</sub>, beyond the Haber Bosch process. III-V InP QDs are employed as visible light photocatalysts under ambient conditions owing to their tunable electronic and absorption profiles, long-lived charge separation, flexibility in surface chemistry tunability, high carrier mobility, high molar extinction coefficient, high photostability, and nontoxic nature compared to heavy metal-based QDs (like CdSe)<sup>2,41</sup>. Their unique surface chemistry and band structure make them excellent candidates for photocatalysis. The surface of each InP QD is rich in In atoms, which serve as catalytic sites that bind and activate nitrite

Characteristics QDs	CdS	CdSe	ZnSe	InP
Band Gap ( $E_g$ ) (in eV)	2.42	1.76	2.70	1.35
Light absorption*	Visible	Visible	UV/Visible	Visible
Toxicity	High	High	Moderate	Low

Table 1: Comparative analysis of InP QDs against other QDs.(Wavelength of the photon absorbed by the nanoparticles is given by:  $\lambda = \frac{1240}{E_g}$ , where  $\lambda$  and  $E_g$  are the wavelength (nm) and band gap energy (eV), respectively.)

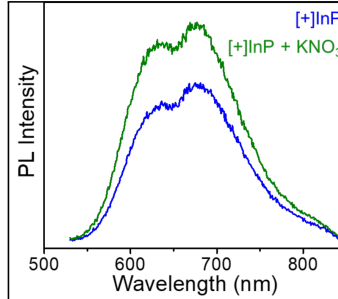


Figure 2: Photoluminescence studies revealing the enhancement in PL intensity of core-only [+] InP QD upon addition of 0.5 mM  $\text{NO}_3^-$  ions.

and nitrate ions by positioning them correctly for the reduction reaction to proceed efficiently. The interaction creates a favorable microenvironment on the surface of the QD, which promotes the desired stepwise mechanism of the reduction of nitrites/nitrates and suppresses unwanted side reactions such as HER<sup>21,49</sup>. The photoexcited charge carriers are generated upon visible light absorption by QDs and channel these charge carriers efficiently to the  $\text{NO}_2^-/\text{NO}_3^-$  ions. The InP is composed of a group III element (In) and a group V element(P). The difference in electronegativity between In and P is relatively small, enabling efficient charge separation (see A.15 for detailed discussion) and reducing recombination in the QD, which is critical for multi-electron processes like photocatalysis. Moreover, the covalent nature of II-V QDs makes them structurally more robust and relatively less toxic than ionic II-VI QDs. This covalent character and enhanced charge transfer capability result in higher quantum yields and improved photocatalytic performance.

#### 1.4 Reaction Mechanism

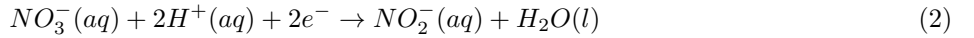
The mechanism of photocatalytic ammonia synthesis proceeds via the following steps:

- Upon absorption of visible light, QDs generate charge carriers (electron-hole pairs), which are efficiently separated due to their covalent crystal structure, minimizing recombination and enhancing photocatalytic activity.  $\text{NO}_2^-/\text{NO}_3^-$  ions in solution are attracted to the surface of InP QDs.
- In atoms on the QD surface bind the oxyanion( $\text{NO}_3^-$  or  $\text{NO}_2^-$ ) via formation of In-O bonds, positioning for reduction (promotional effect).  $\text{NO}_3^-$  forms two In-O coordination bonds where oxygen atoms from the  $\text{NO}_3^-$  ion donate lone pairs of electrons to the empty orbitals ( $5p_x$  &  $5p_y$ ) of In and undergoes subsequent deoxygenation<sup>1</sup>.

It is observed that the PL<sup>2</sup> intensity (see 2) of the [+]InP QDs increased upon adding nitrate ions, indicating strong binding between them, which alters their electronic structure.

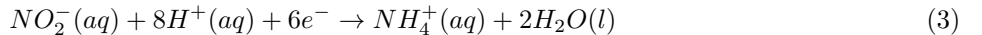


- Deoxygenation:  $\text{NO}_3^-$  ions are reduced to nitrite by accepting electrons and protons:



This step is both energetically demanding and rate-determining.

- The formed  $\text{NO}_2^-$  undergoes further reduction, accepting more electrons and protons to form  $\text{NH}_3$ .



This step proceeds with near 100% efficiency under visible light once nitrite is formed.  $\text{H}_2\text{O}$  is the proton source for the reduction reactions, confirmed by appropriate control experiments and isotope-labeling studies<sup>29</sup>. It is detected as  $\text{NH}_4^+$  due to protonation in aqueous solution. This results in a high yield of  $\text{NH}_3$ .

<sup>1</sup>It is revealed by DFT. Density Functional Theory (DFT) is a quantum-mechanical computational method that bypasses the complexity of solving the many-body Schrodinger equation by focusing on the electron density as a set of three-dimensional single-electron functions describing the probability of finding electrons in space, rather than a wavefunction of the system.

<sup>2</sup>Photoluminescence Intensity (PI) refers to the amount of light emitted by a material when it undergoes photoluminescence.

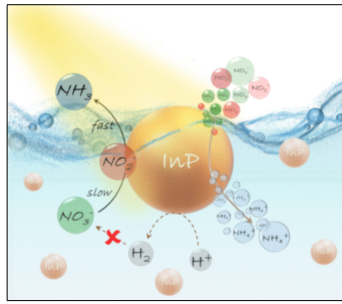


Figure 3: Mechanism of visible-light-driven ammonia synthesis using InP QDs.

- Here,

$$\phi(\%) = \frac{\text{No. of } e^- \text{ consumed}}{\text{Number of photons absorbed}} \times 100\% = \frac{8 \times \text{No. of } NH_3 \text{ molecules formed}}{\text{Number of photons absorbed}} \times 100\% \quad (4)$$

The conversion of  $NO_3^-$  to NH is a multi-electron process. Reducing  $NO_3^-$  to  $NH_3$  requires 8  $e^-$ , so the maximum quantum efficiency<sup>3</sup> is 12.5% ( $1/8 \times 100$ ) if every photogenerated  $e^-$  is used productively. Competing reactions and recombination events further lower the quantum efficiency to 1.45 and 3.7 % for  $NO_3^-$  and  $NO_2^-$ , respectively, at 450 nm.

- The favorable catalyst-reactant interactions and surface properties of InP QDs overrule the HER. This leads to 94% selectivity for  $NH_3$  formation in 2 hours under visible light (at 450 nm) at room temperature.

The  $e^-$  transfer can happen from photoexcited [+] InP QDs to the absorbed  $NO_3^-$  ions, as well as through the TMA ligands<sup>31,53</sup>.

## 1.5 Surface Modification of QDs

Surface modification of QDs is crucial to enhancing their photostability and photocatalytic performance. Ligands are species that bind to the surface of the QDs, profoundly influencing their stability, reactivity, optical properties, and photocatalytic aggregation. During synthesis, organic molecules like amines or carboxylates coordinate with the In atom on the QD surface. These ligands passivate the surface and stabilize the nanocrystals. Positively charged ligands (e.g., amines) create a localized positive surface charge on the QD surface, which electrostatically attracts anionic reactants like  $NO_3^-$  and  $NO_2^-$ , facilitating their binding to catalytic In sites and promoting photocatalytic activity by increasing their local concentration near the In catalytic sites. The positive ligands act as 'gate openers', attracting anions and enabling their binding to the catalytic sites. Whereas, negative ligands act as 'gate blockers', repelling anions and preventing reactant binding, thereby shutting down photocatalytic activity. It was found that the photocatalytic ammonia synthesis was completely inhibited by coating the QDs with negative ligands. Thus, ligands are crucial as gatekeepers in regulating the photocatalytic properties of the QDs. This ligand-controlled gating ensures selectivity by promoting the desired reaction and suppressing competing pathways such as HER. It also allows precise control over the photocatalytic activity by simply changing the ligand shell<sup>4</sup>. The zeta potential of [+] InP QDs was measured as  $+24.0 \pm 8.5 mV$ , while [-] InP QDs showed  $37.0 \pm 6.9 mV$ , indicating effective surface charge modulation. It is crucial to select properly surface-engineered ligands to maximize the charge separation and transfer to the reactants. Bio-compatibility of InP. InP QDs are found to have low intrinsic toxicity and bio-compatibility, making them an ideal visible light photocatalyst for the process. Studies show that even when accumulated in major organs after injection in an animal model, they do not cause acute toxic effects or organ damage. They have been widely used in bioimaging and biomedical applications, such as tumor targeting and minimal adverse effects in animal studies. The toxicity and bio-compatibility of the QDs can be further improved by modifying their surface with specific ligands, reducing the release of potentially harmful ions, and enhancing colloidal stability<sup>34</sup>. This supports the development of sustainable, green alternatives to the original Haber-Bosch process.

## 1.6 Core/Shell InP/ZnS QDs

The photocatalytic reaction system can be further improved by introducing core/shell InP/ZnS QDs. Coating the InP core with the ZnS shell passivates the surface defects and dangling bonds of the QDs, which are sites of charge carriers and recombination (HER), leading to an increase in yield and chemical stability. This allows QDs to maintain their structure and function through multiple reaction cycles. The ZnS shell creates a favorable interface for the spatial separation of photogenerated electron-hole pairs. It helps in configuring charge carriers within the InP core but also facilitates their extraction when a suitable scavenger is present. This suppresses the recombination and increases the

<sup>3</sup> Assuming the Stark-Einstein law and no competing reaction

<sup>4</sup>Ligand shell is the protective and functional organic layer that coats the inorganic core of a QD or other nanocrystals during synthesis and remains associated with it in the solution.

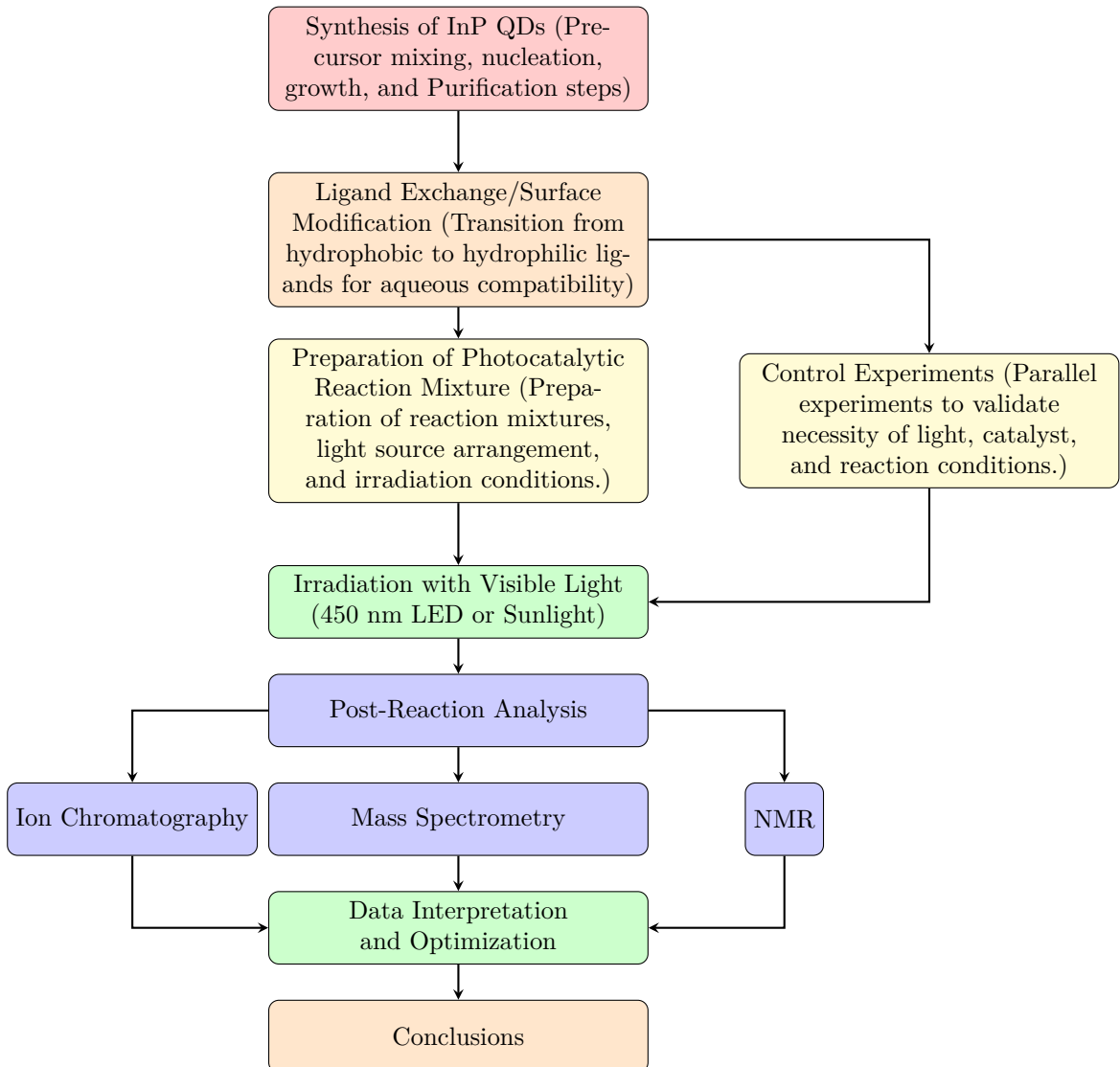


Figure 4: Overview of the experimental methodology for visible-light-driven nitrate reduction using InP QDs.

yield of the reaction system. Hole scavengers (e.g., methanol, ascorbic acid) are species that react rapidly with the photogenerated holes, suppressing HER and allowing the  $e^-$  to accumulate and participate in the reaction. It minimizes side reactions. This overall enables the QDs to retain photocatalytic activity for at least 4 consecutive cycles and 75% retention in subsequent cycles.

## 1.7 Objective and Significance

This study aims to validate the efficacy of InP QDs for  $\text{NH}_3$  generation under visible light and to uncover the mechanistic principles underpinning this process. Its significance is underscored by its potential to provide a sustainable, scalable alternative to the Haber-Bosch process. This approach offers real-world scalability, with lower toxicity and higher bio-compatibility of InP QDs supporting compliance with regulatory standards and enhancing public acceptance. This strategy aligns with the Sustainable Development Goals by reducing fossil fuel reliance, greenhouse gas emissions, and promoting decentralized fertilizer production. Future work may involve scaling the system under natural sunlight or exploring ternary QD systems with improved selectivity. Altogether, the use of InP QDs presents a highly promising, low-toxicity alternative for visible-light-driven ammonia synthesis. The following subsections elaborate on the synthetic methodology and characterization protocols.

## 2 Methods

Almost all reagents (mentioned in C.4) are purchased from Sigma-Aldrich and were used without any purification, except TMA, which was synthesized via a reported procedure<sup>59</sup>, as reported in the original article. However, the publication does not specify the purity, form, or storage conditions of the chemicals. For standard laboratory practice and reproducibility, it is generally recommended to use the highest available purity and follow the manufacturer's specified guidelines for storage conditions for each reagent.

Wavelength (nm)	Energy (eV)
450	2.76
532	2.33
580	2.14

Table 2: Energy (eV) of photons with different wavelengths (nm)

## 2.1 Photocatalytic Light Source Setup

### 2.1.1 Light Sources

Two blue LEDs with a wavelength of 450 nm were positioned 1 cm from the reaction cuvette on both sides, to ensure even light distribution and eliminate 'hot spots'. The wavelength matches the bandgap of InP QDs, enabling efficient generation of electron-hole pairs. Green (532 nm) and Yellow (580 nm) LEDs were also used for further wavelength-dependent studies. It is to test the QDs' activity for less energetic photons. These two wavelengths are used as controls. The energy of a photon is given by the relation:

$$E = \frac{hc}{\lambda} \quad (5)$$

where,

- $E$ : Energy of the photon (in eV)
- $h$ : Planck's constant=  $4.13587 \times 10^{-15}$  eV · s
- $c$ : Speed of light=  $3 \times 10^8$  m/s
- $\lambda$ : Wavelength (in m)

### 2.1.2 Reactor

A 4 mL long-neck quartz cuvette with high UV-Vis transparency is used for real-time reaction monitoring. Quartz cuvettes are chemically inert (preventing interference with photocatalytic reactions) and withstand prolonged irradiation (resistant to photochemical degradation).

### 2.1.3 Intensity & Power: Calculation and Measurement

Precise power measurement is done by the Gentec EO MAESTRO optical power meter with a photodiode/thermopile sensor. It ensures consistent light intensity across experiments. It measures irradiance with <3% uncertainty using calibrated detectors. The MAESTRO is calibrated for 450 nm using a reference detector. For each LED,

- Total power for each LED= 10 W (For both LEDs, the total power= 20 W)
- 

$$Irradiance = \frac{\text{LED power (mW)}}{\text{Illuminated area(cm}^2)} = \frac{10000mW}{100cm^2} \approx 100mWcm^{-2} \quad (6)$$

(Thus, the total irradiance for all wavelengths= 200 mWcm<sup>-2</sup>)

- Distance from the reaction cuvette= 1 cm
- Distance from the reaction cuvette= 1 cm

### 2.1.4 Challenges

1. LEDs generate heat at a proximity of 1 cm. However, short irradiation time can reduce this.
2. Quartz/water interfaces can cause bending of light due to refraction and partial attenuation of the incident light as it passes through the quartz reactor window. It leads to the non-uniformity of photons falling on the solution and reduced effective photon flux on the catalyst. To compensate for light bending through quartz, the photon flux inside the reactor was calibrated using a chemical actinometer placed in the reaction vessel. The transmission spectrum of the quartz window was measured, and all quantum yield calculations were corrected for the measured transmittance at 450 nm.

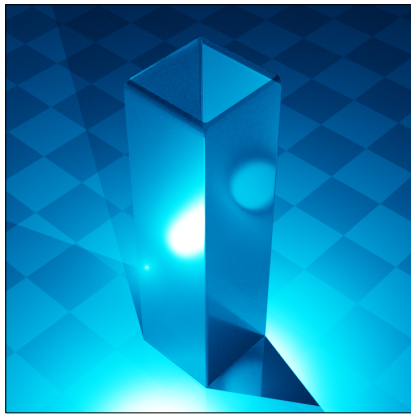


Figure 5: Bending of light by quartz

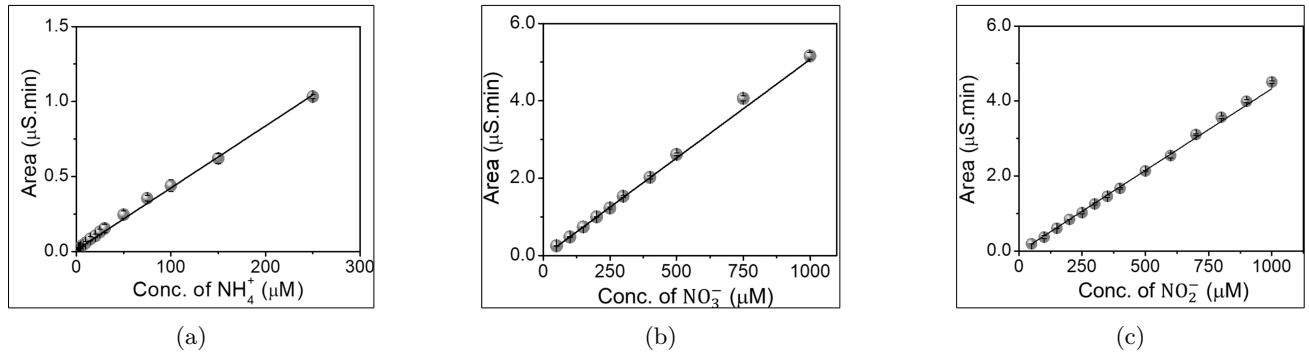


Figure 6: (a–c) Ion chromatography calibration curves for (a)  $\text{NH}_4^+$ , (b)  $\text{NO}_3^-$ , and (c)  $\text{NO}_2^-$ , respectively. Each plot was generated using standard solutions with varying concentrations.

### 2.1.5 Key Steps

In a 4 mL long-necked quartz tube, [+] InP QDs ( $2.5 \mu\text{M}$ , 0.5 mol%) and  $\text{KNO}_3/\text{KNO}_2$  (0.5 mM) reaction mixture in  $\text{H}_2\text{O}$  was mixed with a total volume of 3 mL throughout the studies and pH at 5. Acidic pH facilitates proton availability for  $\text{NH}_3$  formation and maintains  $\text{NH}_3$  as  $\text{NH}_4^+$ , preventing volatile  $\text{NH}_3$  loss. It was purged with Argon. Ar purging is performed to remove dissolved  $\text{O}_2$  and prevent competitive  $\text{e}^-$  consumption and undesired oxidation reactions. The reaction mixture was then irradiated for 2 h.

## 2.2 Post Reaction Analysis

### 2.2.1 Quantization of Ammonia

Accurate quantization of  $\text{NH}_3$  is challenging due to the low concentration of  $\text{NH}_3$ , environmental contamination risks, and interference by other components. Colorimetric methods like Nessler's reagent and the indophenol blue method suffer from major limitations. These methods are often associated with large errors as they are heavily dependent on precise pH control, particularly at low concentrations. They are often associated with false signals due to the residual catalysts or organic byproducts. However, Ionic chromatography and  $^1\text{H}$  NMR overcome these limitations and emerge as suitable for post-reaction analysis, by avoiding any interference from the reaction mixture. 500  $\mu\text{L}$  of the reaction mixture is injected.  $\text{NH}_4^+$  interacts weakly with the column and elutes first (~8.5 min), while other ions elute later. A conductivity detector measures ions as they exit the column, yielding a chromatogram. The area under the peak at the retention time of ~8.5 min was used for the calculation of  $\text{NH}_4^+$  concentration. Standard solutions of  $\text{NH}_4^+$  are run to create a reference for calibration. A similar analysis was carried out for  $\text{NO}_3^-$  and  $\text{NO}_2^-$  conversions as well to calculate the total conversion yields.

### 2.2.2 Optimization of Reaction Parameters

From the above table, it can be inferred that with the increase in the catalyst particles, more active sites will be available, leading to potentially faster reaction rates. Thus, with the increase in the concentration of [+] InP QDs, there was a gradual increase in the  $\text{NH}_4^+$  formation. Even though 1.0 mol% gave the maximum  $\text{NH}_4^+$  production, 0.5 mol% has been used for all the subsequent experiments due to cost-effectiveness, resource conservation, and scalability concerns. It maintains reproducibility and reduces synthesis time and cost. From the graphs, it can be inferred that with the increase in substrate concentration, there was an increase in ammonia concentration and eventually attained

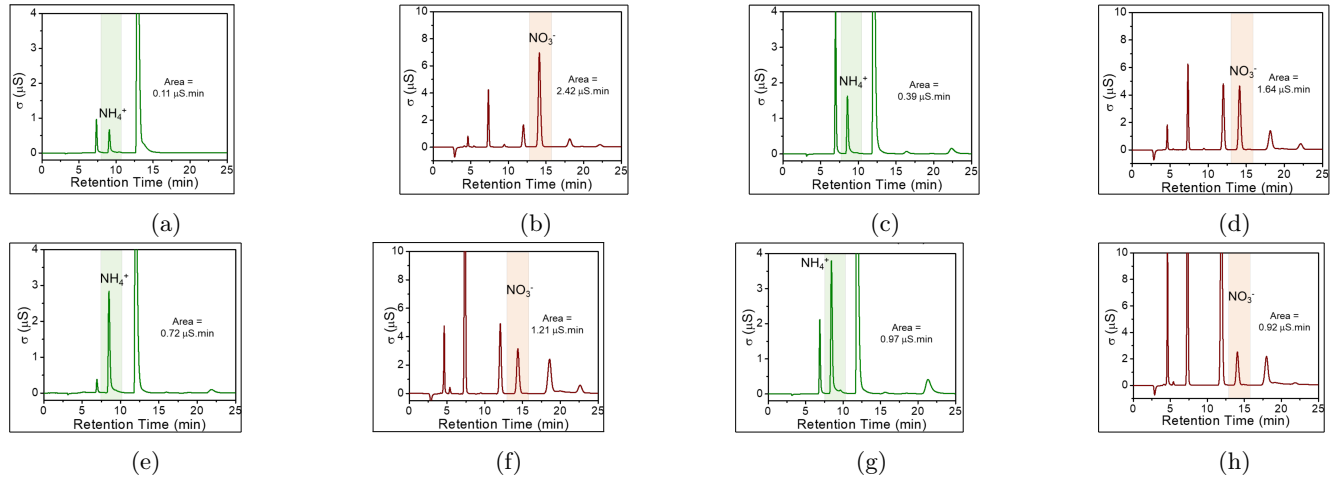


Figure 7: (a–h) Ion chromatograms of photocatalytic reactions with varying InP QD concentrations (0.1, 0.3, 0.5, and 1.0 mol%). Each sub-figure shows cation or anion detection corresponding to the respective QD loading. (Note: The original article<sup>29</sup> does not report replicate number ( $n$ ), error bars, or statistical analysis. For reproducibility, such details should be included in future studies.)

Catalyst Loading	$\text{NH}_4^+$ Peak Area ( $\mu\text{S} \cdot \text{min}$ )	% Increase
0.1 mol%	0.11	—
0.3 mol%	0.36	2.27
0.5 mol%	0.72	1.00
1.0 mol%	0.87	0.21

Table 3: Variation in  $\text{NH}_3$  production with different catalyst loading concentrations. (Original data didn't include error metrics; values represent mean observations)

$\text{KNO}_3^+$ Loading	$\text{NH}_4^+$ Peak Area ( $\mu\text{Smin}$ )	% Increase
0.25 mol%	0.35	—
0.5 mol%	0.68	94
0.75 mol%	0.54	54
1.0 mol%	0.51	46

Table 4: Variation in  $\text{NH}_3$  production with different concentrations of  $\text{KNO}_3^+$ . (Original data did not include error metrics; values represent mean observations.)

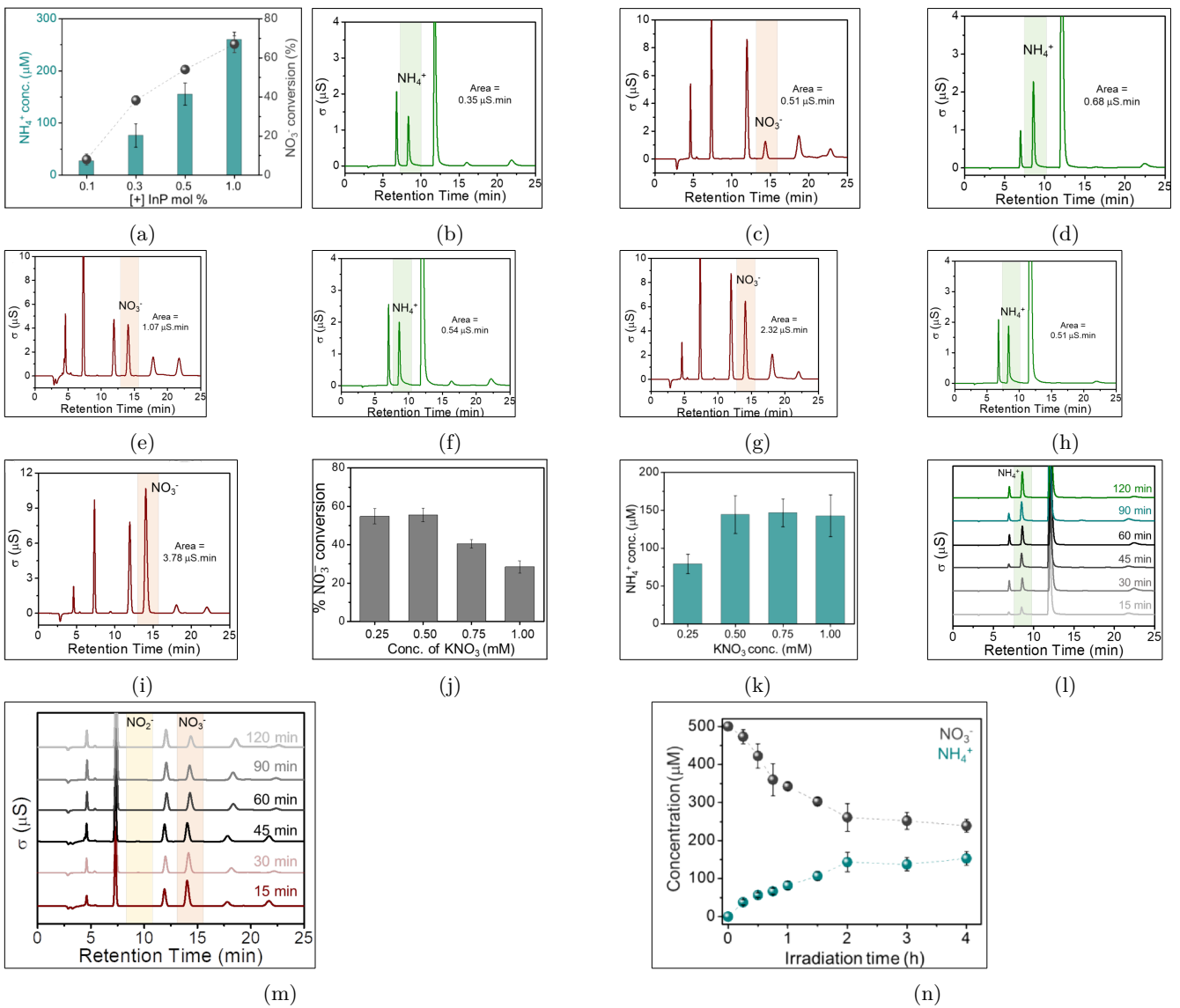


Figure 8: (a) NH<sub>4</sub><sup>+</sup> concentration and NO<sub>3</sub><sup>-</sup> conversion vs. InP QD amount. (b)–(c) Cation and anion chromatograms for 0.25 mM KNO<sub>3</sub>. (d)–(e) Cation and anion chromatograms for 0.50 mM KNO<sub>3</sub>. (f)–(g) Cation and anion chromatograms for 0.75 mM KNO<sub>3</sub>. (h)–(i) Cation and anion chromatograms for 1.00 mM KNO<sub>3</sub>. (j) Total NO<sub>3</sub><sup>-</sup> conversion vs. KNO<sub>3</sub> concentration. (k) NH<sub>4</sub><sup>+</sup> yield vs. KNO<sub>3</sub>. (l) NH<sub>4</sub><sup>+</sup> peak growth with time. (m) NO<sub>3</sub><sup>-</sup> decrease over time. (n) Final product NH<sub>4</sub><sup>+</sup> concentration over 2 hours.

a saturation state of all active sites on the [+] InP QDs. As a result, a further increase in KNO<sub>3</sub> concentration did not increase NH<sub>4</sub><sup>+</sup> production. From the graphs, it can be inferred that a two-hour irradiation establishes the optimal reaction duration for the reaction mixture containing 2.5 μM [+] InP QDs and 0.5 mM KNO<sub>3</sub>. Further irradiation provides diminishing returns. The absence of detectable NO<sub>2</sub><sup>-</sup> intermediates confirms rapid conversion to ammonia..

## 2.3 Temperature Effects in Photocatalysis

Photocatalysis NH<sub>3</sub> synthesis using InP QDs is performed at room temperature and ambient pressure. It is rooted in the fundamental photo-physical and photo-kinetic processes governing the activity and selectivity of QD photocatalysis.

### 2.3.1 Optimization of Temperature

At room temperature, the thermal energy is optimal for the efficient charge separation within the InP QDs. If the temperature is too low, carrier mobility may be insufficient, slowing down the surface reactions. However, increasing the temperature above room temperature introduces several detrimental effects:

1. Higher temperature increases the lattice vibration within the QS, which in turn may increase the rate of HER, without producing useful chemical work. This will result in a reduction of charge carriers available for nitrate reduction, lowering the overall efficiency.

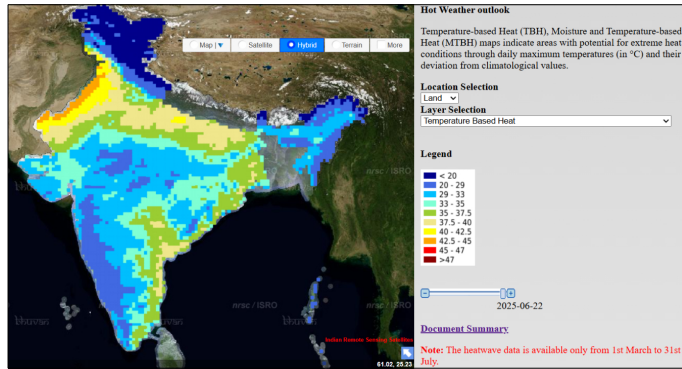


Figure 9: Temperature-based Heat map of India<sup>28</sup>

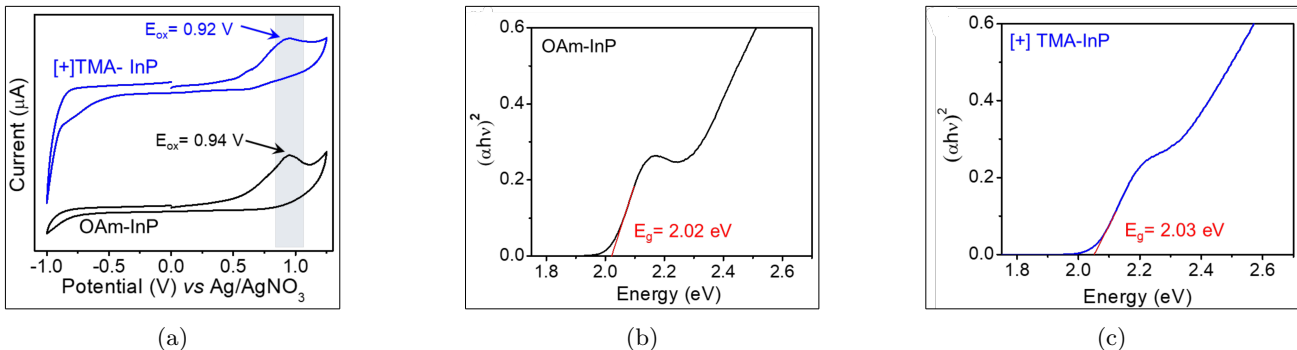


Figure 10: (a) As the [+] InP QD film was made from an aqueous suspension, a water oxidation peak was observed at 0.65 V in addition to the peak corresponding to the valence band of [+] InP. The water oxidation peak was validated by recording the CV of the electrolyte in the water-acetonitrile mixture (green voltammogram). (b) Tauc plot of OAm-InP QDs. (c) Tauc plot of [+] TMA-InP QDs.

- Increasing the temperature will increase the thermal energy of the charge carriers, leading to degradation of surface ligands attached to the QDs. This reduces the selectivity of the photocatalyst for NH<sub>3</sub>.

### 2.3.2 Relevance to Global Warming

As global temperatures rise due to climate change, maintaining optimal room temperature conditions for photocatalytic processes may become challenging, especially in regions lacking climate control infrastructure. High ambient temperature necessitates additional cooling, increasing the energy footprint and potentially offsetting the sustainability benefits of the process. Higher temperatures accelerate the degradation of QD ligands and the core/shell interface, shortening the catalyst lifetime. Future research should therefore focus on engineering QDs and surface ligands for enhanced thermal stability to ensure robust performance even as environmental conditions fluctuate.

## 3 Result And Discussion

### 3.1 Determination of Band Position of InP QDs

**Cyclic voltammetry (CV)** measured oxidation and reduction potential to determine the valence bond energy by ramping the potential of a working electrode linearly versus time. Whereas, the **Tauc plot** is used to calculate the optical band gap from the ultraviolet-visible absorption data<sup>5</sup>. The absolute energies of the valence and conduction bands (see A.19) of the InP QDs were calculated through the combination of cyclic voltammetry and UV-vis absorption measurements (see B.1 for the experimental setup). it can be inferred that the oxidation peak potentials corresponding to the peaks on the CV are as follows.

- OAm-InP QDs: 0.94 V vs. Ag/AgNO<sub>3</sub>.
- [+]-TMA-InP QDs: 0.92 V vs. Ag/AgNO<sub>3</sub>.

The relative reference electrode potential (E<sub>ref</sub>) was calculated to be 4.65 eV, using the ferrocene/ferrocenium couple as the internal standard. On calculating, the conduction band was found to be -3.57 and -3.54 eV vs vacuum for [-]InP QDs and [+]InP QDs, respectively (see C.1 for calculations).

<sup>5</sup>It is a graph prepared based on light absorption data to estimate the band gap.

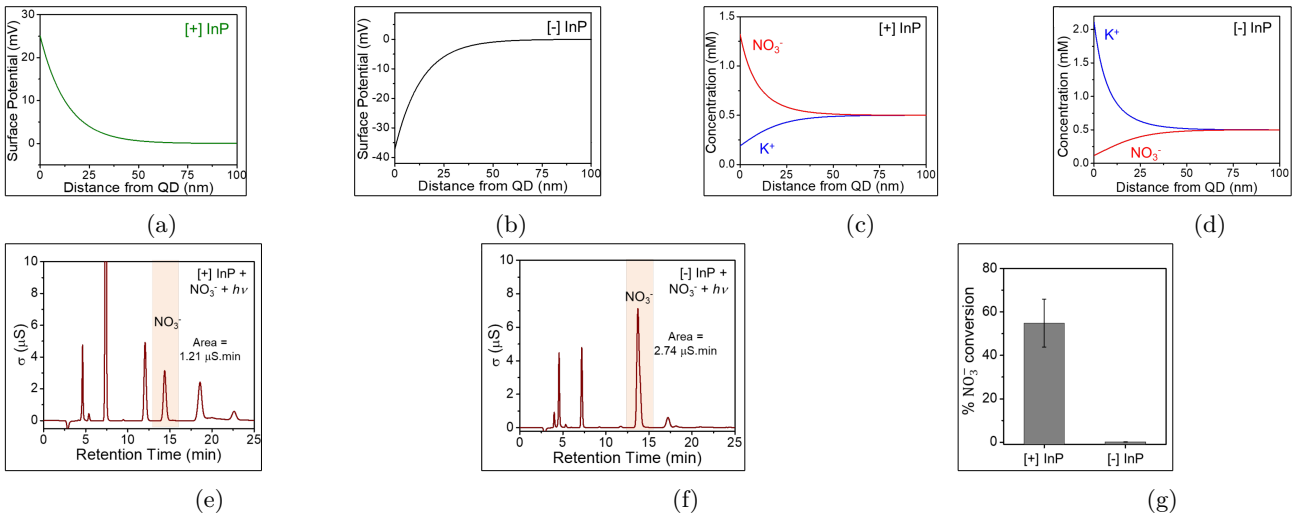


Figure 11: (a–d) Surface potential and ion concentration distributions near [+] and [-] InP QDs. (e–f) Anion chromatograms for  $\text{NO}_3^-$  quantification with respective QDs. (g) Comparative  $\text{NO}_3^-$  reduction efficiency under visible light (450 nm, 2 h).

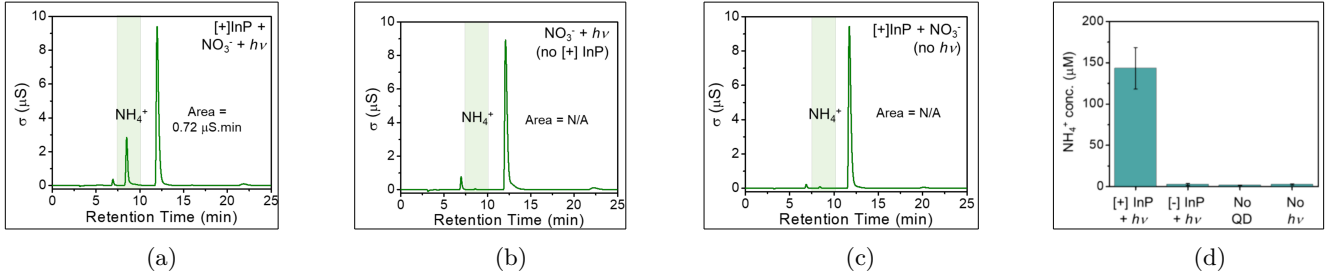


Figure 12: (a–d) Control experiments highlighting the necessity of both light and [+] InP QDs for  $\text{NH}_4^+$  generation.

### 3.2 Electrostatic Channeling by QDs

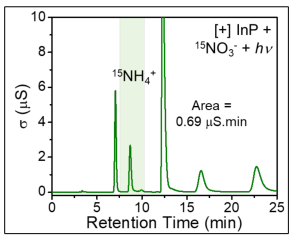
The concentration of ions near the QD surface follows a Boltzmann distribution (see C.2). From the graphs (see 11), it can be inferred that [+] InP QDs have high local  $[\text{NO}_3^-]$  within the Debye length and [-] InP QDs repel  $\text{NO}_3^-$ , confirming its charge-dependent activity. A mere change of surface ligands from [+]TMA to [-]MUA completely switches off the photocatalytic conversion. This proves the favorable catalyst-reactant interactions through the change of QD surface ligands. The area under signal 14.5 min corresponds to the amount of  $\text{NO}_3^-$  after the photocatalytic conversion. This area was lower for the photocatalytic reaction performed with TMA-capped [+]InP QDs compared to MUA-capped [-]InP QDs.

### 3.3 Control experiments

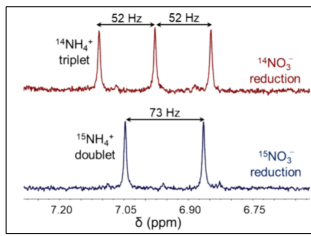
Control experiments are essential to understand the mechanism of a reaction. The optimized reaction conditions have the reaction system acting as the positive control, where a strong ammonia peak at 8.5 min is observed. This confirms that ammonia production occurs robustly when all components work together. No detectable ammonia peak was seen in the absence of a catalyst. It eliminates the possibility of direct photolysis and confirms that the [+] InP QDs are essential to harness light energy. Similarly, no detectable ammonia peak was observed in the absence of light. The flat baseline proves that the [+] InP QDs alone cannot catalyze the reaction in the dark. This eliminates spontaneous reduction and background contamination. From the series of control experiments, it can be confirmed ed the necessity of light and [+] InP QDs as a catalyst for the reaction to occur.

### 3.4 Photocatalytic Experiments with Isotope-Labeled Nitrate

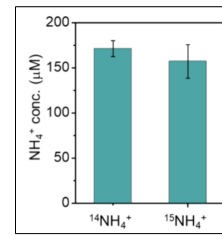
$^{14}\text{N}$  has a nuclear spin of 1, i.e., the proton attached to  $^{14}\text{N}$  has its NMR signal split into three peaks (triplets), whereas  $^{15}\text{N}$  has a nuclear spin of 1/2, i.e., the proton attached to the  $^{15}\text{N}$  atom has two orientations, splitting its NMR signal into two peaks (doublet). To confirm that the  $\text{NH}_3$  comes from the reaction mixture, not contamination,  $^{15}\text{NO}_3^-$  has been used instead of  $^{14}\text{NO}_3^-$  with the reaction mixture acidified to a pH 1-2 with HCl. If the catalyst works, it will produce  $^{15}\text{NH}_3$  instead of  $^{14}\text{NH}_3$ . The doublet (two peaks) in the  $^1\text{H}$ -NMR spectroscopy confirms  $\text{NO}_3^-$  as the sole source of  $\text{NH}_3$ .



(a)

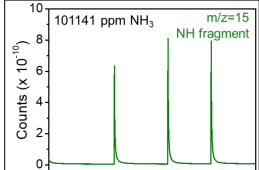


(b)

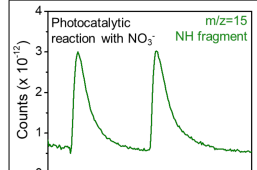


(c)

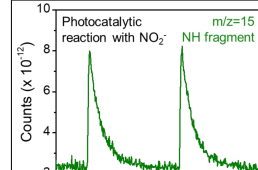
Figure 13: (a) Ion chromatogram showing the formation of  $^{15}\text{NH}_4^+$  from isotope-labeled  $^{15}\text{NO}_3^-$ . (b)  $^1\text{H}$  NMR spectra of  $^{14}\text{NH}_4^+$  and  $^{15}\text{NH}_4^+$  from photocatalytic reduction by  $[+]$  InP QDs. (c) Bar diagram comparing  $^{14}\text{NH}_4^+$  and  $^{15}\text{NH}_4^+$ , confirming  $\text{NO}_3^-$  as the sole N source.



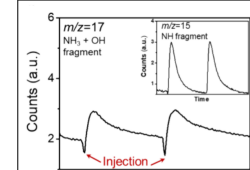
(a)



(b)



(c)



(d)

Figure 14: (a) Gas-phase mass analysis of standard  $\text{NH}_3$  gas (conc. 101141 ppm). (b) Gas-phase mass analysis of photocatalytic reaction performed with  $[+]$  InP QDs and  $\text{NO}_3^-$ . (c) Gas-phase mass analysis of photocatalytic reaction performed with  $[+]$  InP QDs and  $\text{NO}_2^-$ . (d) Mass analysis of gases in the headspace after the photocatalytic reaction using  $^{14}\text{NO}_3^-$ .  $m/z = 17$  confirms presence of  $^{14}\text{NH}_3$ .

### 3.5 Mass Spectrometric (MS) Analysis

#### 3.5.1 Quantization of Ammonia in the Gas Phase

The quantification of gaseous  $\text{NH}_3$  in the reactor headspace was performed using a BELMASS II quadrupole mass spectrometer.  $\text{H}_2\text{O}$  is also present in the reaction mixture, so it is important to prevent false positives from  $\text{H}_2\text{O}$  and its fragments:  $\text{H}_2\text{O}^+$  ( $m/z = 18$ ),  $\text{OH}^+$  ( $m/z = 17$ ) and  $\text{O}^+$  ( $m/z = 16$ ) which may mix up with fragments of  $\text{NH}_3$ ;  $\text{NH}_3^+$  ( $m/z = 17$ ) and  $\text{NH}_2^+$  ( $m/z = 16$ ). So,  $\text{NH}^+$  fragment ( $m/z = 15$ ) is considered as it is unique to  $\text{NH}_3$  and does not overlap with  $\text{H}_2\text{O}$  fragments-derived signals. 0.4 mL of 101141 ppm of  $\text{NH}_3$  gas was injected using a gas-tight syringe thrice, and the average area under the  $m/z = 15$  was analyzed. The areas under the curves were compared for standard and photocatalytic reactions.

Average area under the peak for  $m/z = 15$  in standard  $\text{NH}_3 = 2.035 \times 10^{-9} \pm 6.3 \times 10^{-10}$

Average area under the peak  $m/z = 15$  after the photocatalytic reaction =  $2.86 \times 10^{-11} \pm 3.7 \times 10^{-10}$

Moles of  $\text{NH}_3$  in headspace =  $0.37 \pm 0.11 \mu\text{mol}$

Moles of aqueous-phase  $\text{NH}_4^+$  (via ion chromatography) =  $0.43 \pm 0.08 \mu\text{mol}$

Total  $\text{NH}_3$  yield =  $(0.37 \pm 0.11 + 0.43 \pm 0.08) \mu\text{mol} = 0.80 \pm 0.19 \mu\text{mol}$  ( $\sim 6.8 \text{ ppm}$ ,  $\sim 430 \mu\text{molg}^{-1}$ )

Total  $\text{NO}_3^-$  converted =  $0.85 \pm 0.1 \mu\text{mol}$

$$\text{Selectivity}_{\text{NO}_3^-} (\%) = \frac{\text{Total } \text{NH}_3}{\text{Converted } \text{NO}_3^-} \times 100 = \frac{0.80}{0.85} \times 100 \approx 94\% \quad (7)$$

Similarly,

$$\text{Selectivity}_{\text{NO}_2^-} (\%) \approx 91\% \quad (8)$$

This proves the excellent selectivity of  $[+]\text{InP}$  QD catalysts towards  $\text{NH}_3$  production.

#### 3.5.2 Isotopic Labeling

The presence of ammonia gas in the headspace was further validated by isotopically labeled  $^{15}\text{NO}_3$  as mass signals corresponding to  $^{15}\text{NH}_3$  were observed.

### 3.6 Optimized Photocatalytic Ammonia Synthesis with InP QDs

#### 3.6.1 Optimized Reaction Conditions

Catalyst concentration of  $2.5 \mu\text{M}$  (0.5 mol%)  $[+]$  InP with a substrate concentration of  $0.5 \text{ mM KNO}_3$  for a reaction time of 2 hours of visible light irradiation is identified as the ideal parameter for the reaction system. Under this optimized condition, in aqueous phase,  $143 \pm 25 \mu\text{M}$  ( $\sim 2.5 \text{ ppm}$ ,  $\sim 160 \mu\text{molg}^{-1}$ )  $\text{NH}_3$  is produced,  $52.2 \pm 7.4\%$  ( $261.2 \pm 3.7 \mu\text{M}$ )

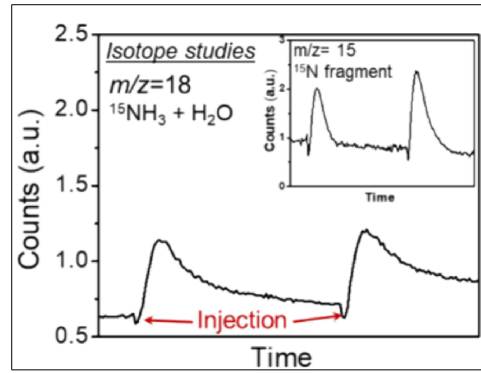


Figure 15: Mass analysis of the gases in the headspace after the photocatalytic reaction was performed with  $^{15}\text{NO}_3^-$  as the N-source.  $m/z = 18$  indicate the presence of  $^{15}\text{NH}_3$  in the gaseous phase from  $^{15}\text{NO}_3^-$

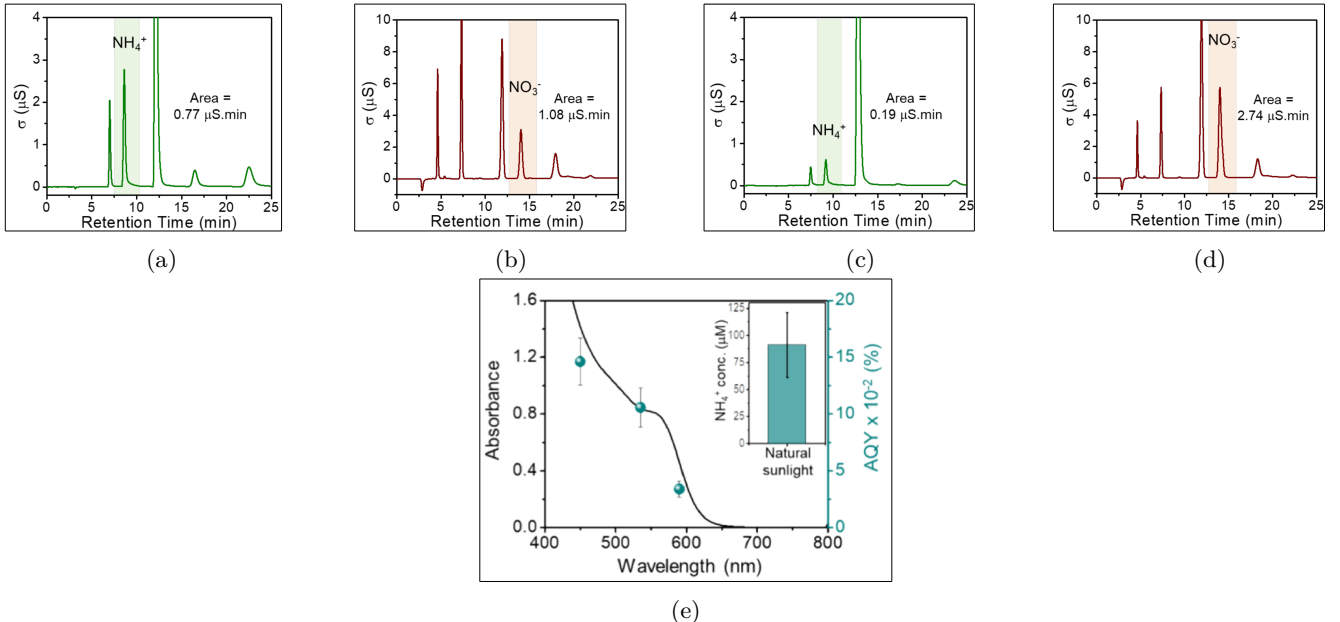


Figure 16: (a) Cation chromatograms under 532 nm light ( $2 \times 10$  W LEDs,  $200 \text{ mW/cm}^2$ ). (b) Anion chromatograms under 532 nm light (same conditions) (c) Cation chromatograms under 580 nm light (same conditions) (d) Anion chromatograms under 580 nm light (same conditions) (e) Action spectra showing  $\text{NH}_4^+$  formation vs. wavelength with  $[+]$  InP QDs. Inset: Solar feasibility.

of  $\text{NO}_3^-$  has been converted. The yield of  $\text{NH}_4^+$  was estimated to be  $57.5 \pm 9.3\%$  in the aqueous phase<sup>9,38,39</sup>. Not all  $\text{NO}_3^-$  ions are converted to  $\text{NH}_3$ . It could be attributed to the incomplete extraction of photoexcited charge carriers from  $[+]$  InP QD photocatalyst, as a significant amount of photoexcited  $e^-$  is diverted to HER.

### 3.7 Sunlight-Driven Ammonia Synthesis with InP QDs

#### 3.7.1 Action Spectrum

The action spectrum illustrates the effectiveness of different light wavelengths in driving a chemical reaction, as measured by the apparent quantum yield (AQY). The above action spectra confirm the active participation of  $[+]$  InP QDs as catalysts. With a decrease in the wavelength of the light, the energy of the photons increases, thereby enhancing overall conversion<sup>50,58</sup>.

#### 3.7.2 Photocatalytic Experiments in Sunlight

In the above laboratory setup, a monochromatic light source is used; however, practical applications must operate under natural sunlight conditions, as utilizing solar energy reduces operational costs for its potential industrial applications. Photocatalytic reactions were performed under direct sunlight.  $[+]$  InP QDs and  $\text{KNO}_3$  ( $\text{NO}_3^-$  source) were mixed in a cuvette, which was exposed for 2 hours. The light intensity of the sunlight was measured to be  $95 \text{ mWcm}^{-2}$ .  $[+]$  InP QDs can absorb multiple wavelengths from the sunlight, but the quantum efficiency increases with a decrease in the wavelength of the light. Under the direct sunlight,  $91 \pm 30 \mu\text{M}$  of  $\text{NH}_4^+$  was formed and  $26.5 \pm 7.7\%$  of  $\text{NO}_3^-$  was converted within 2 hours. However, the photocatalytic performance under direct sunlight is subject to several



Figure 17: (a) IC for  $\text{NH}_4^+$  quantification after photocatalytic reaction with [+] InP QDs under natural sunlight (2 h). (b) IC for  $\text{NO}_3^-$  quantification after photocatalytic reaction with [+] InP QDs under natural sunlight (2 h).

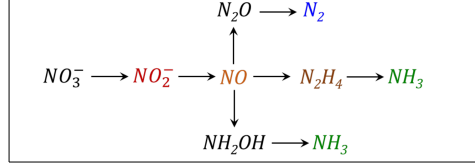


Figure 18: Schematic representation of probable products formed during nitrate reduction

challenges:

- Variation in intensity:** LEDs have constant intensity throughout the experiment, whereas the intensity of sunlight naturally fluctuates due to cloud cover, atmospheric conditions, and changes in solar angle. Lower sunlight intensity means fewer photons available for exciting electrons in the QDs. During summer, light intensity is higher and longer daylight hours, whereas performance during Winter is reduced.
- Spectral differences:** As seen above (in 3.7.1), the quantum efficiency of the photocatalytic process increases with a decrease in wavelength as the energy of the photons increases. However, most of the spectral distribution of solar radiation on Earth is of higher wavelengths ( $>400$  nm), leading to lower quantum efficiency. This hinders the overall performance of the photocatalytic process.
- Coherence properties:** LEDs are highly coherent light sources, whereas sunlight is incoherent light. This led to variations in photon arrival patterns.

These challenges render the direct quantitative comparison between photocatalytic performance under direct sunlight and monochromatic LEDs misleading. This bridges the gap between laboratory research and practical implementation. The sole purpose of performing the photocatalytic reduction under sunlight was to showcase the feasibility in real-world conditions and strengthen the translational aspect of [+] InP QD-based  $\text{NH}_3$  synthesis.

### 3.8 Side Product Analysis

The photocatalytic reaction, being a multi-electron and multi-proton process, creates several undesirable intermediate species (mainly N-oxides) with different stabilities for each electron addition<sup>14,67</sup>. Different reduction routes can lead to various nitrogen-containing products. The stable intermediates accumulate if the process stops partway. Most commonly observed products include<sup>62,67</sup>:

- Nitrite ( $\text{NO}_2^-$ ): 2-electron reduction intermediate (analyzed using ion chromatography)
- Hydroxylamine ( $\text{NH}_2\text{OH}$ ): 6-electron reduction intermediate (analyzed with colorimetry assay)
- Hydrazine ( $\text{N}_2\text{H}_2$ ): Nitrogen-nitrogen coupled product (analyzed with colorimetry assay)
- Nitrogen gas ( $\text{N}_2$ ): Complete deoxygenation product (analyzed with mass spectrometry)
- Other  $\text{NO}_x$  gases: Various nitrogen oxides (analyzed with mass spectrometry)

#### 3.8.1 Gaseous side-products

##### $\text{N}_2$

For the target ion  $\text{N}_2^+$ ,  $\frac{m}{z} = 28$

From the mass spectrometric analysis, a negligible amount of  $\text{N}_2$  was found in the reactor's headspace. Similarly,



Figure 19: (a) Analysis of common gaseous side product  $\text{N}_2$  through mass spectrometry. (b) Analysis of isotopically labeled  $^{15}\text{N}_2$  through mass spectrometry.

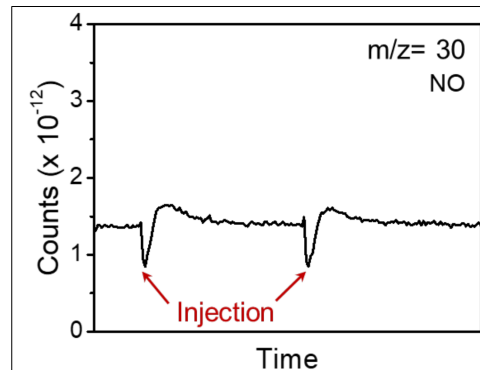


Figure 20: Analysis of the common gaseous side product  $\text{NO}$  through mass spectrometry

for headspace analysis with isotope-labeled  $^{15}\text{NO}_3^-$ ,  $^{15}\text{N}_2^+$ ,  $\frac{m}{z}=30$ . From the mass spectrometric analysis, a negligible amount of  $^{15}\text{N}_2$  was found in the reactor's headspace. This overall rules out the reductive pathway of



## NO

For the target ion  $\text{NO}^+$ ,  $\frac{m}{z} = \frac{14+16}{1} = 30$

From the mass spectrometric analysis, a negligible amount of NO was found in the reactor's headspace. Similarly, for headspace analysis with isotope-labeled  $^{15}\text{NO}_3^-$ ,  $^{15}\text{NO}^+$ ,  $\frac{m}{z} = 31$ . From the mass spectrometric analysis, a negligible amount of  $^{15}\text{NO}$  was found in the reactor's headspace. This rules out the incomplete reduction stopping at the NO step. This confirms the selective formation of  $\text{NH}_3$ .

### 3.8.2 Colorimetric Analysis for Organic Nitrogen Compounds

#### $\text{NH}_2\text{OH}$

The 8-hydroquinone colorimetric assay is used for the identification of hydroxylamine<sup>15</sup>.

#### Procedure:

- Mix analyte solution (1 mL), PBS (1 mL), and 11% 8-hydroxyquinoline.
  - Analyte is the photocatalytic reaction mixture being tested for the presence of hydroxylamine, containing QDs, nitrates, nitrites, and other potential side products.
  - PBS or phosphate-buffered saline is a commonly used buffer solution (pH 7.4), containing P salts ( $\text{Na}_2\text{HPO}_4$ ,  $\text{NaH}_2\text{PO}_4$ ) and NaCl. It is widely used in analytical chemistry as it maintains optimal conditions for the colorimetric reaction to occur.
  - 8-Hydroxyquinoline (also known as 8-quinolinol) serves as a chromogenic reagent that selectively reacts with hydroxylamine to form a colored complex. It acts as a bidentate ligand with the nitrogen and oxygen atoms of the hydroxyl group as the chelation sites
- Add 0.1 M  $\text{Na}_2\text{CO}_3$  (1 mL) with vigorous shaking.
- Heating at  $100^\circ\text{C}$  results in the formation of a coordinate complex of bright bluish-green color
- Monitor absorption at 706 nm ( $\lambda_{max}$  of the complex formed)

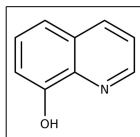


Figure 21: 8-Hydroquinoline



Figure 22: (a)Absorption spectra of the reaction mixture with a known concentration (0–250  $\mu$ M) of NH<sub>2</sub>OH. (b)Absorption spectrum of the reaction mixture after photocatalytic reduction of NO<sub>3</sub><sup>-</sup> to NH<sub>4</sub><sup>+</sup> with [+] InP QDs.

## Result

On comparing the absorption spectrum of the reaction mixture after photocatalytic reduction of NO<sub>3</sub><sup>-</sup> to NH<sub>4</sub><sup>+</sup> with [+]InP QDs for 2 hours with the calibration curve (plotted with concentration range of 0-250 $\mu$ M NH<sub>4</sub><sup>+</sup> solutions), it can be concluded that there was negligible formation of hydroxylamine. It can be inferred from the absence of an absorption peak at 706 nm. **N<sub>2</sub>H<sub>2</sub>**

The standard Watt-Chrisp spectrophotometric method was used for the identification of hydrazine<sup>24</sup>.

## Procedure:

- The coloring agent is prepared by dissolving 4-(dimethylamino)benzaldehyde in concentrated. Sulfuric acid and ethanol. Here, conc. H<sub>2</sub>SO<sub>4</sub> acts as a catalyst and acidic medium for the reaction, and ethanol acts as the solvent and enhances solubility.
- An equal volume of the reaction mixture and coloring agent is mixed.
- Incubate it for 20 minutes at room temperature for the color to develop. If hydrazine is present, the solution will turn yellow with an absorption peak at 458 nm due to the formation of a 4-(Dimethylamino)benzaldehyde-hydrazine coordination complex.

## Result:

The calibration curves were plotted from standard hydrazine solutions (0-3 ppm). Upon comparing the absorption spectrum of the reaction mixture after 2 hours of photocatalytic reaction with the known concentrations, it can be concluded that a negligible amount of hydrazine was formed. It can be inferred from the absence of an absorption peak at 485 nm. The absence of any side products indicates that a direct reduction pathway is being followed, without any reductive coupling or incomplete reduction. [+]InP QDs selectively reduce NO<sub>3</sub><sup>-</sup> to ammonia.

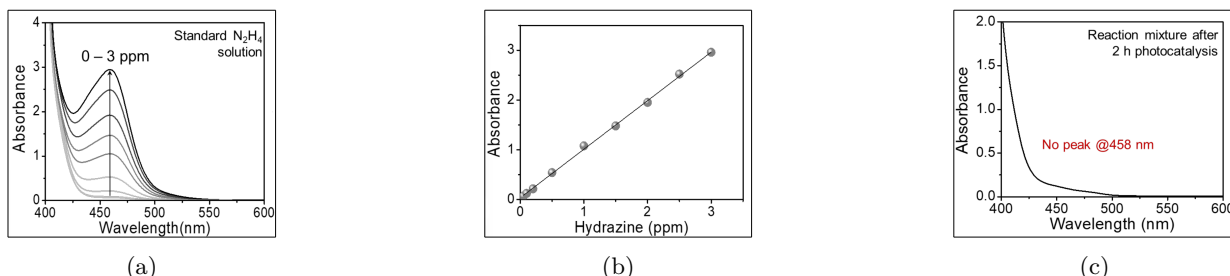


Figure 23: (a)Absorption spectra of the reaction mixture with a known concentration (0–3 ppm) of N<sub>2</sub>H<sub>2</sub>. (b)Calibration plot obtained from absorption data. (c)Absorption spectrum of the photocatalytic reaction mixture consisting of [+] InP QDs and KNO<sub>3</sub> after 2 h of light irradiation.



Figure 24: (a) Cation ion chromatogram for the reaction mixture. (b) Anion ion chromatogram for the reaction mixture. The  $\text{NO}_2^-$  peak disappeared completely, indicating 100% conversion.

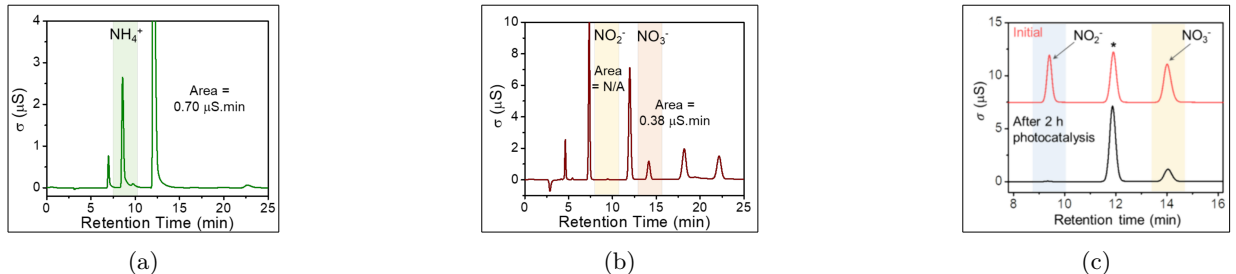
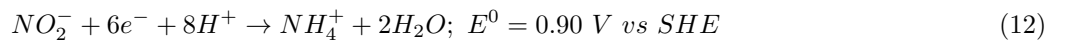


Figure 25: (a) Cation ion chromatograms depicting the formation of  $\text{NH}_4^+$  and conversion of  $\text{NO}_2^-$  and  $\text{NO}_3^-$ . (b) Anion ion chromatograms depicting the formation of  $\text{NH}_4^+$  and conversion of  $\text{NO}_2^-$  and  $\text{NO}_3^-$ . No  $\text{NO}_2^-$  accumulates as it is consumed. (c) Ion chromatograms for competitive photocatalytic experiments with an equimolar mixture of  $\text{NO}_2^-$  and  $\text{NO}_3^-$  as N-source. The asterisk marks  $\text{Cl}^-$  ions. [+] InP QDs preferentially reduce nitrite over nitrate.

### 3.9 Rate-determining step

For the conversion of nitrate to ammonia, the initial two-electron reduction of  $\text{NO}_3^-$  to  $\text{NO}_2^-$  is the most energetically challenging step.



It can be explained by looking at the standard electrode potential ( $E_0$ ). A higher value of  $E^0$  (0.90 V) leads to a favorable reaction, i.e., easier to accept an electron, whereas a lower value (0.49 V) means it's much harder to reduce  $\text{NO}_3^-$  to  $\text{NO}_2^-$ .

#### 3.9.1 Using Nitrite as the Starting Material

On running the photocatalytic reaction, using nitrite instead of nitrate as the starting material under the same optimized conditions, it is observed that:

- The conversion from  $\text{NO}_2^-$  to  $\text{NH}_4^+$  was strikingly completed within 1 hour of visible-light illumination.
- The converted ammonia amount was found to be higher  $280 \pm 25 \mu\text{M}$  ( $\sim 5.5 \text{ ppm}$ ,  $\sim 320 \mu\text{mol g}^{-1}$ ) compared to  $143 \pm 25 \mu\text{M}$  that obtained from  $\text{NO}_3^-$ .
- The quantum efficiency is found to be higher. The total ammonia produced in the aqueous and gas phase is  $1.36 \mu\text{mol}$ , about 91% of the total  $\text{NO}_2^-$  converted.

#### 3.9.2 Competitive Reaction

On running the photocatalytic reaction, using a reaction comprising of equal amount of  $\text{NO}_3^-$  and  $\text{NO}_2^-$ , it is observed (based on IC result) that 100% of  $\text{NO}_2^-$  was converted (complete conversion), whereas only 50% of  $\text{NO}_3^-$  was converted to ammonia (most of the  $\text{NO}_3^-$  remained unreacted), within 2 hours of photocatalysis. [+]InP QD photocatalyst strongly prefers to react with  $\text{NO}_2^-$  over  $\text{NO}_3^-$ , confirming that  $\text{NO}_2^-$  is much faster. It suggests that  $\text{NO}_3^-$  to  $\text{NO}_2^-$  is a probable rate-determining step.

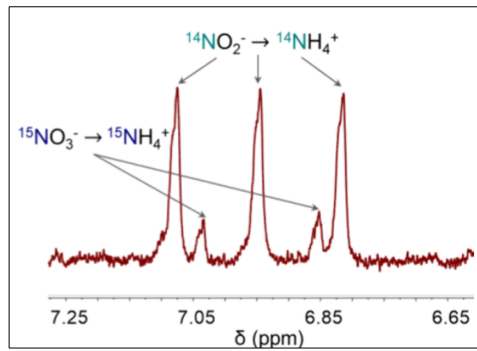


Figure 26:  $^1\text{H}$ -NMR spectra for competitive photocatalytic experiments performed with an equimolar mixture of and  $^{14}\text{NO}_2^- + ^{15}\text{NO}_3^-$  as the N-source, respectively

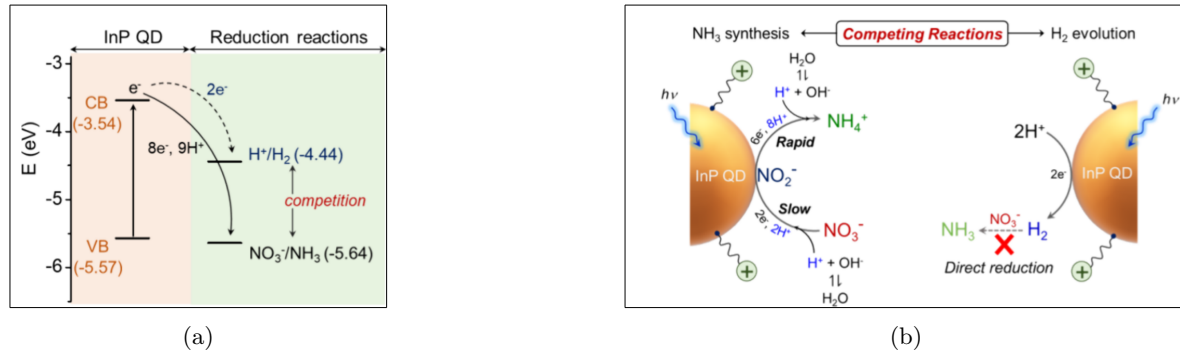


Figure 27: (a)Schematics of energy level diagrams representing the thermodynamic feasibility of possible reduction reactions with [+] InP QDs. (b)Schematics of the proposed reaction mechanism for the visible-light photocatalyzed reduction of  $\text{NO}_3^-$  to  $\text{NH}_4^+$  by [+] InP QDs.

### 3.9.3 Isotopic Competition

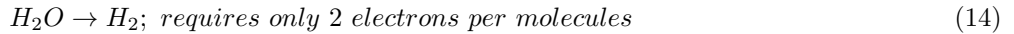
A reaction mixture comprising  $^{14}\text{NO}_2^-$  and  $^{15}\text{NO}_3^-$  in equal amount, was photocatalyzed for 2 hours. In  $^1\text{H}$ -NMR,  $^{15}\text{NO}_3^-$  shows up a doublet whereas  $^{14}\text{NO}_2^-$  shows up a triplet. On  $^1\text{H}$ -NMR, the triplet peak was found to be much larger than the doublet peak. This tells us that when both the substrates were present simultaneously,  $\text{NO}_2^-$  gets converted to  $\text{NH}_4^+$  much more readily than  $\text{NO}_3^-$ .

### 3.9.4 Conclusion

Based on the experiments, the  $\text{NO}_3^-$  to  $\text{NO}_2^-$  conversion is the probable rate-limiting step controlling the overall  $\text{NH}_3$  synthesis when  $\text{NO}_2^-$  is used as the N-source. It provides the stage for catalyst design to optimize for  $\text{NO}_3^-$  binding and activation or an alternative approach to pre-convert  $\text{NO}_3^-$  to  $\text{NO}_2^-$  using other methods.

## 3.10 Understanding HER as a Competing Reaction in Photocatalytic Ammonia Synthesis

HER is a common & fundamental challenge for photocatalytic reactions involving multiple electrons and protons. From the energy band positions of InP QDs, both reactions are thermodynamically feasible:



Since HER requires fewer electrons, it's easier for it to compete for the available electrons. It was found that 17.5%<sup>29</sup> of electrons are consumed in HER, while 82.5% are consumed in the photocatalytic reaction, reducing the overall efficiency of the photocatalytic conversion.

### 3.10.1 Does HER Improve the Photocatalytic Conversion?

Previous studies have suggested that HER may contribute to ammonia production, with  $\text{H}_2$  as a potent reducing agent for  $\text{NO}_3^-$  ions as well<sup>5,32,66</sup>. To test whether hydrogen gas contributes to the nitrate reduction, the following two sets of experiments are carried out:

#### Pre-Irradiation Test

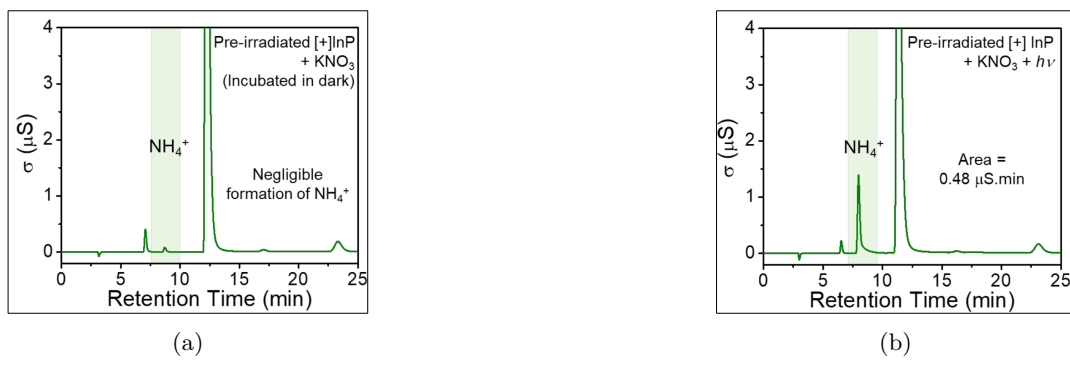


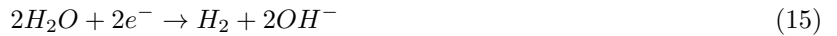
Figure 28: (a) Cation ion chromatogram in the absence of light after the addition of  $\text{KNO}_3$  in the pre-irradiated reaction mixture containing [+] InP QDs. (b) Cation ion chromatogram in the presence of light after the addition of  $\text{KNO}_3$  in the pre-irradiated reaction mixture containing [+] InP QDs.

The following procedure is followed to test whether pre-existing H<sub>2</sub> can reduce nitrate in the absence of active photocatalysis:

## Procedure:

- + InP QDs were dispersed in water (3 mL)

- The reaction mixture was irradiated with 20 W (450 nm) LEDs for 2 hours, maintaining the light intensity at 200 mWcm<sup>-2</sup> on the cuvette walls. The reaction mixture was purged with Ar gas to create an inert atmosphere. Irradiation of [+]InP QDs in water results in H<sub>2</sub> evolution through photocatalytic water splitting<sup>10</sup>, confirmed by Gas chromatography (using Agilent 7890 GC).



- 0.5 mM KNO<sub>3</sub> was added to this H<sub>2</sub>-containing reaction mixture under inert conditions.
  - The reaction mixture was incubated for 2 hours in the dark under optimized conditions, and then analyzed for NH<sub>4+</sub> formation.
  - A Similar procedure is followed for light illumination.

## Results:

- Negligible ammonia formation is observed under dark conditions, despite H<sub>2</sub> presence.
  - Significant ammonia formation is observed under light conditions.

This means that H<sub>2</sub> gas alone cannot reduce NO<sub>3</sub><sup>-</sup> to NH<sub>4</sub><sup>+</sup> without light activation of the QDs. **Direct H<sub>2</sub> purging test**

### **Procedure:**

- + InP QDs and 0.5 mM KNO<sub>3</sub> are mixed in a reaction vessel.

- H<sub>2</sub> gas is bubbled into the reaction mixture.
  - The reaction mixture was incubated for 2 hours in the dark, and analyzed for NH<sub>4</sub><sup>+</sup> formation.
  - A similar procedure is followed for light conditions.

### Results:

- No ammonia formation was observed under dark conditions.
  - Normal ammonia formation, same as without extra added H<sub>2</sub> gas.

This means that adding extra H<sub>2</sub> gas doesn't improve the reaction. It confirms that H<sub>2</sub> doesn't participate in nitrate reduction or inhibit the reaction. The same experiments were repeated using NO<sub>2</sub><sup>-</sup> instead of NO<sub>3</sub><sup>-</sup> as the starting material, with identical results. H<sub>2</sub> showed no effect on the conversion process. These results prove that photoexcited electrons from the QDs are solely responsible for the NO<sub>2</sub><sup>-</sup> / NO<sub>3</sub><sup>-</sup> reduction, and HER is simply a competitive, non-contributing side reaction. HER reduces the yield, although it does not interfere with the reaction kinetics.



Figure 29: (a) Ion chromatogram of reaction mixture purged with  $\text{H}_2$  gas in absence of light. (b) Ion chromatogram of reaction mixture purged with  $\text{H}_2$  gas in the presence of light.

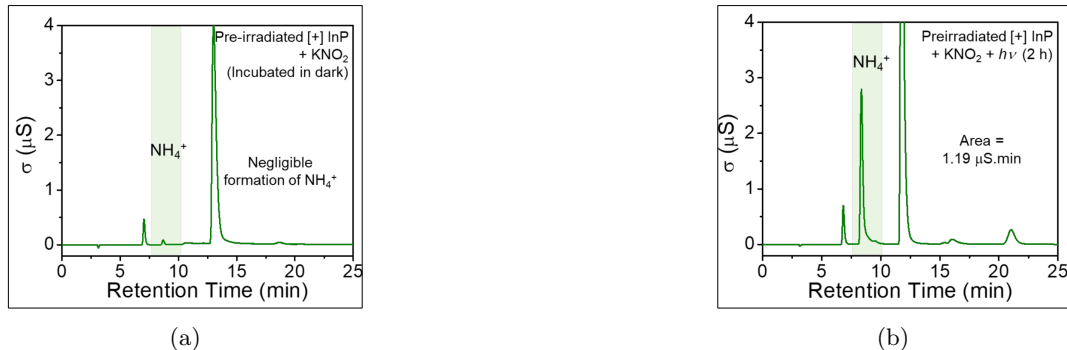


Figure 30: (a) Cation ion chromatogram in the absence of light after the addition of  $\text{KNO}_3$  to the pre-irradiated reaction mixture containing  $[+]$  InP QDs. (b) Cation ion chromatogram in the presence of light after the addition of  $\text{KNO}_3$  to the pre-irradiated reaction mixture containing  $[+]$  InP QDs.

### 3.10.2 Further Studies

Being a competitive side reaction for the desirable photocatalytic conversion, it becomes crucial for the research to increase the yield of the overall process by suppressing the HER. Two methods of suppression of HER are mentioned in the article, which are described as follows. Both approaches represent sophisticated examples of surface chemistry engineering, precisely controlling the molecular environment around catalysts to optimize their performance for specific reactions.

#### Ligand Engineering

Ligands are like 'clothes' for the QDs, which regulate how the QDs interact with their environment. Selecting a ligand with suitable properties is very crucial for the suppression of the HER. Water molecules form a hydrogen bond network around the QDs. This network serves as a 'highway' for the HER by facilitating the protons to move efficiently. By suppressing the movement of protons, HER can be suppressed.  $\text{pK}_a$  is the measure of how easily a molecule accepts/gives up protons. Higher  $\text{pK}_a$  means the molecule holds onto protons more tightly. Using a high  $\text{pK}_a$  having ligands, it aggressively grabs protons from nearby water, reducing the free protons available for HER. Many ligands have large alkyl groups that repel water, creating 'water-free' zones around the active sites on the QDs. By suppressing the HER, more photogenerated electrons become available for the desirable photocatalytic conversion of  $\text{NO}_3^-$  to  $\text{NH}_4^+$ <sup>19</sup>.

#### Surface Modification with non-catalytic ions

Non-catalytic ions are metal ions that don't help a chemical reaction to occur as they are difficult to reduce. Since they don't accept electrons easily, the electrons are most likely to be consumed in the HER or photocatalytic conversion of nitrate to ammonia. These ions occupy surface positions on the QDs where HER could occur, thus acting as a physical site blocker by reducing the surface area for HER to occur. They also create a local electronic environment unfavorable for the protons to approach (like charges repel), reducing the local concentration of protons around the QDs for HER and maintaining favorable conditions for  $\text{NO}_3^-$  reduction. These ions can be attached to QDs through several approaches, like post-synthesis modifications, incorporating small amounts of such ions during QD formation, or using specialized ligands that contain these metal ions<sup>6</sup>.

## 3.11 Proton Source Identification

In the conversion of nitrate to ammonia, 10 protons per molecule are consumed. This set the stage for the identification of the proton source involved. There are overall two potential proton sources:

1. Water

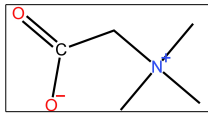


Figure 31: Betaine

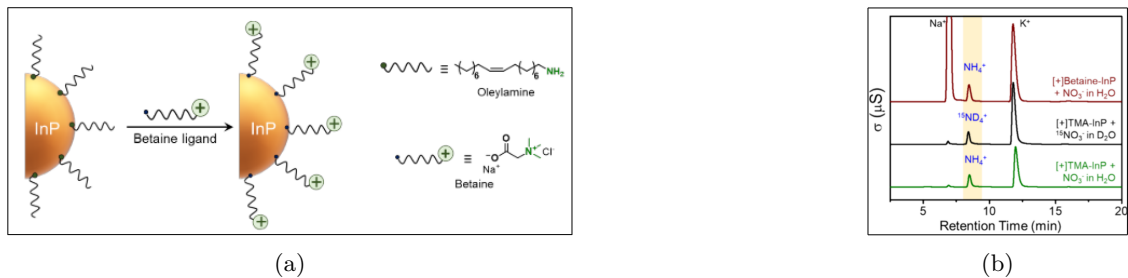


Figure 32: (a) Schematics showing the ligand exchange of InP QDs with non-thiolated betaine ligand. (b) Cation chromatograms comparing  $[+]$ -InP QDs in  $\text{D}_2\text{O}$  and non-thiolated betaine-capped InP QDs with  $[+]$ -InP QDs in  $\text{H}_2\text{O}$ .

## 2. TMA Ligands on the QDs

### 3.11.1 TMA Ligands on QDs

TMA ligands are attached to the QD surface, which contains the thiol group (-SH) that could potentially donate protons. For verification, the following experiments are conducted:

#### FTIR Analysis of Ligand Binding

FTIR analysis is used to understand how TMA ligands bind to InP QDs. The studies confirm that it binds as X-type thiolate ( $\text{R-S}^-$ ) rather than neutral thiols ( $\text{R-SH}$ ), i.e., it is devoid of any ionizable protons, so it can't provide protons for the reaction. It was further supported by the study by Hens and his co-workers, where the native OAm ligands participated in an acid-base reaction to form oleylammonium chloride, leaving thiolates to bind on InP QDs<sup>16</sup>.

#### Betaine Ligand Control

Betaine ( $-\text{OOC-CH}_2-\text{NMe}_3^+$ ) is a non-thiolate quaternary ammonium ligand. With Betaine, 45% conversion % is achieved in the nitrate to ammonia conversion with 2.16 ppm of  $\text{NH}_4^+$  formed in the aqueous phase. This proves that surface ligands are the proton source. These two experiments confirm that TMA is not the proton source for the photocatalytic conversion of nitrate to ammonia.

### 3.11.2 Water

#### Polar Aprotic Solvent Test

The photocatalytic conversion is performed in aprotic solvents like acetone, acetonitrile, DMF, and DMSO instead of water<sup>4</sup>. Here, acetone is chosen, supported by the report by Wu and his co-worker, which confirms that water is the sole proton source for the HER<sup>35</sup>. Being a polar aprotic solvent, it dissolves ionic compounds but does not donate protons. If water is the sole proton source, removing it should stop the ammonia formation. Likewise, no ammonia formation was observed in acetone. Even adding excess TMA ligands does not help in the ammonia formation in acetone. This strongly suggests that water is the sole proton source.

#### Deuterated Water ( $\text{D}_2\text{O}$ )

Here, the regular water ( $\text{H}_2\text{O}$ ) is replaced with heavy water ( $\text{D}_2\text{O}$ ) and  $^{15}\text{NO}_3^-$  as the nitrogen source. If water provides protons in the photocatalytic conversion, then using  $\text{D}_2\text{O}$ , deuterium should get incorporated into ammonia. This would produce  $^{15}\text{ND}_4^+$ . Mass spectroscopy is used to differentiate between the isotopic variants<sup>6</sup>. A similar ammonia yield of  $125.5 \pm 2\mu\text{M}$  is observed in heavy water (compared to  $143 \pm 25\mu\text{M}$  in water). The formation of  $^{25}\text{ND}_4^+$  was confirmed through GLDH AssayB.4. This confirmed the deuterium incorporation from  $\text{D}_2\text{O}$  in the photocatalytic conversion. Gas phase mass analysis of the photocatalytic reaction performed showed signals corresponding to  $\frac{m}{z}^{15}\text{ND}_3 = 21$  and  $\frac{m}{z}^{15}\text{ND}_2 = 19$  confirms the incorporation of deuterium from  $\text{D}_2\text{O}$  into the ammonia product.<sup>7</sup> The simultaneous occurrence of HER during the reaction provides additional support to the idea of water being the sole proton source, as both  $\text{NH}_4^+$  synthesis and HER require protons. From all the experiments performed and the discussion, it can be concluded that water is the sole proton source in the photocatalytic synthesis of ammonia with  $[+]$  InP QDs.

<sup>6</sup>  $\frac{m}{z}^{15}\text{NO}_2 = 21$  and  $\frac{m}{z}^{15}\text{D}_2\text{O} = 19$  in gas phase analysis.

<sup>7</sup> All the reactions in acetone (polar aprotic solvent) were performed using the Whatman filter paper-based dip-catalyst system. Concentrations of  $[+]$  InP and  $\text{NO}_3^-$  were maintained at 0.5 mol% and 0.5 mM, respectively. It is to be noted that the paper substrate does not affect the photocatalytic activity of  $[+]$  InP QDs when the reaction was performed in water under similar conditions (as seen in the recyclability studies).

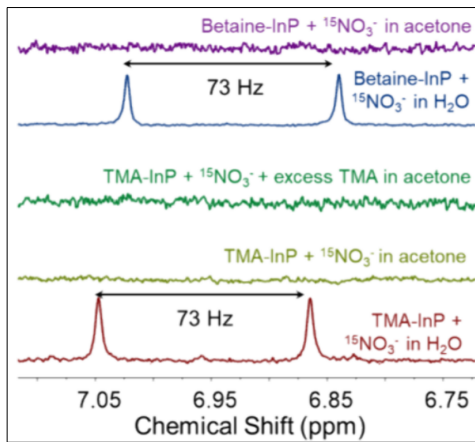


Figure 33: Comparison of  $^1\text{H}$ NMR under different reaction conditions performed with  $^{15}\text{NO}_3^-$  as the N-source.



Figure 34: (a) Gas-phase mass analysis with  $^{15}\text{NO}_3^-$  in  $\text{D}_2\text{O}$ .  $m/z = 21$  ( $^{15}\text{ND}_3$ ) confirms water as proton source. (b) Gas-phase mass analysis with  $^{15}\text{NO}_3^-$  in  $\text{D}_2\text{O}$ .  $m/z = 19$  ( $^{15}\text{ND}_2$ ) supports deuterium incorporation.

Reactions	$\text{NH}_3$ formation	Remarks
[+] InP + $^{15}\text{NO}_3^-$ in water	✓	[+] InP QD is photocatalyzing the reduction of nitrate to ammonia.
[+] InP + $^{15}\text{NO}_3^-$ in acetone*	✗	Water <i>surely</i> plays an active role. <i>May</i> act as a proton source.
[+] InP + $^{14}\text{NO}_3^-$ + excess [+] TMA in water	✓	Enhanced stability of InP QD photocatalysts in the presence of excess TMA ligand.
[+] InP + $^{15}\text{NO}_3^-$ + excess [+] TMA in acetone*	✗	Overrules the possibility of [+] TMA ligand acting as a proton source.
Betaine-InP + $^{14}\text{NO}_3^-$ in water	✓	Overrules the possibility of [+] TMA ligand acting as a proton source.
Betaine-InP + $^{15}\text{NO}_3^-$ in water	✓	Water <i>surely</i> plays an active role.
Betaine-InP + $^{15}\text{NO}_3^-$ in acetone*	✗	Water <i>surely</i> plays an active role. Overrules the possibility of [+] TMA ligand acting as a proton source.
[+] InP + $^{15}\text{NO}_3^-$ in $\text{D}_2\text{O}$	✗	Water is <i>surely</i> the proton source.

Table 5: Table summarizing the reactions performed to identify the probable proton source and hole scavenger in the photocatalytic  $\text{NO}_3^-$  reduction to  $\text{NH}_3$  by [+] InP QDs.

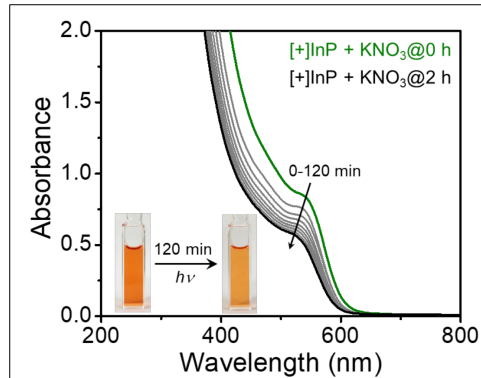


Figure 35: Time-dependent absorption profile of [+] InP QDs in the photocatalytic reaction mixture.

### 3.12 Photocatalytic Stability of [+]InP QDs

When InP QDs absorb light, electrons and holes are photogenerated. These holes must be removed quickly for the QDs to remain stable; otherwise, it will cause surface etching of the QDs or detachment of ligands from the QD surface (like in CdS QDs)<sup>16,40,57</sup>. For this purpose, hole scavengers are important. There are two potent hole scavengers:

1. [+]TMA ligand
2. Water

If any of the above is an actual hole scavenger, their oxidase products will be detected. However, no oxidized product from either was observed. This means the reaction system is devoid of any hole scavengers, which may lead to surface-etching (as discussed later). The long-term performance of [+] InP QDs photocatalysts depends critically on their stability under photo-illumination. Two key experiments:

1. Time-dependent UV-Visible absorption spectroscopy
2. X-ray photoelectron spectroscopy (XPS)

were employed to probe the photostability during the photocatalytic conversion of nitrate to ammonia.

#### 3.12.1 Time-Dependent UV-Visible Absorption Study

##### Visual Color Change

Upon the continuous irradiation by the visible light in the nitrate-containing reaction mixture, the original deep orange color of the colloidal suspension of [+] InP-QDs fades away slowly, indicating alteration of the nanocrystals over time. The inset photographs of the reaction mixture over time during the photocatalytic reaction show the loss of the vibrant orange color, confirming physical changes to the QDs.

##### Hypsochromic and hypochromic shift

The hypsochromic shift<sup>8</sup> of the first excitonic absorption peak from longer to shorter wavelengths, indicating a decrease in the size of the QDS, due to surface etching<sup>9</sup>. The hypochromic shift<sup>10</sup> of the overall absorbance intensity at the excitonic peak also decreases, indicating the reduction in the QD concentration or loss of light-absorbing material. These spectral changes were tracked at regular intervals during the photocatalytic conversion, demonstrating continuous size reduction and partial degradation of the QDs under the optimized reaction conditions. Simultaneous shifts serve as a real-time indicator of the QDs' stability.

#### 3.12.2 X-Ray Photoelectron Spectroscopy (XPS) Analysis

XPS studies were carried out before and after the photocatalytic conversion to understand and verify the chemical composition change of [+] InP QDs. Before irradiation with visible light, the 3d spectrum shows two peaks at 443.62 eV ( $3d_{5/2}$ ) and 451.22 eV ( $3d_{3/2}$ ), with 7.6 eV spin-orbit splitting corresponding to In-P bonds in pristine [+] InP QDs. Whereas, in the P 2p spectrum, two peaks at 127.54 eV ( $2p_{3/2}$ ) and 128.44 eV ( $2p_{1/2}$ ), with 0.9 eV splitting, further confirm the InP lattice, before irradiation with visible light<sup>17,52,60</sup>.

After 2 hours of the photocatalytic reaction, an additional peak between 131.94 eV and 132.84 eV appears in the P 2p spectrum, indicative of P species ( $InPO_x$ ) formation due to surface oxidation by water and dissolved oxygen. The In 3d doublet becomes wider and less defined, signaling partial oxidation of In atoms to In oxide. Control XPS on OAm-[+]

<sup>8</sup>A hypsochromic shift or blue shift occurs when an absorption peak moves to a shorter wavelength or higher energy in the spectrum. It confirms that photocatalytic conditions have partially dissolved or shrunk the QDs.

<sup>9</sup>Surface etching refers to the gradual removal or degradation of atomic layers from the surface of the [+] InP QDs. It is different from catalyst deactivation.

<sup>10</sup>A hypochromic shift describes a decrease in the intensity of a spectral band while its position remains unchanged or shifts slightly.

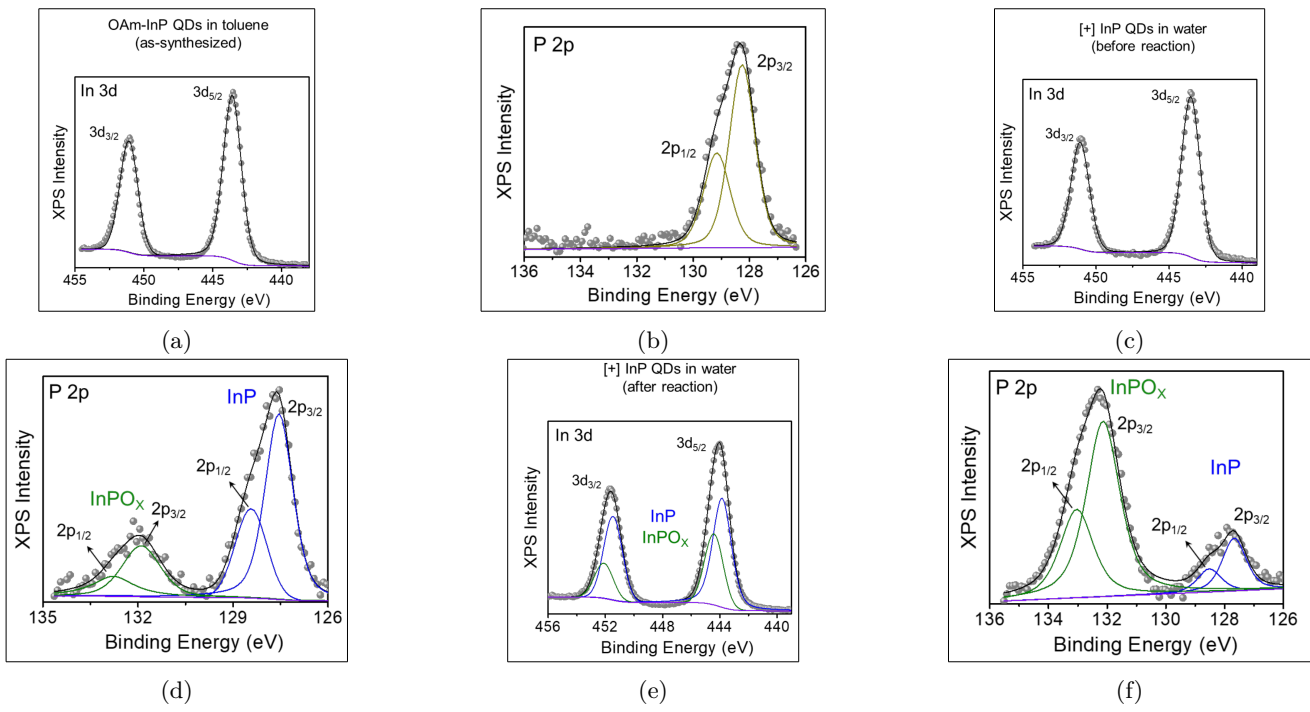


Figure 36: (a)XPS spectra for as-synthesized OAm-InP QDs before the photocatalytic reaction. (b)XPS spectra for as-synthesized OAm-InP QDs before the photocatalytic reaction. (c)XPS spectra for [+] InP QDs before the photocatalytic reaction. (d)XPS spectra for [+] InP QDs before the photocatalytic reaction. (e) XPS spectra for [+] InP QDs after the photocatalytic reaction. (f)XPS spectra for [+] InP QDs after the photocatalytic reaction.

InP showed no such oxidation, confirming that observed changes resulted from the photocatalytic conditions rather than sample preparation artifacts. Surface oxidation of InP to InPO<sub>x</sub> weakens the lattice and promotes the etching of the QD cores. Even as oxidation and etching proceed, no visible aggregation or precipitation occurs throughout the 2 hours of photocatalytic conversion; i.e., the aqueous colloidal suspension of [+] InP QDs remains stable. This implies that surface ligands maintain their steric and electrostatic stabilization despite partial degradation of the core. Progressive etching and surface oxidation of the photocatalyst [+] InP QDs reduces the density of active In-P sites and quantum confinement effects, leading to diminished photocatalytic efficiency over repeated use. It highlights the need for improved photostability strategies, such as protective shells or sacrificial hole scavengers.

### 3.13 Recyclability in QD Systems

#### 3.13.1 With Core-Only InP QDs

The recyclability of a catalyst is the ability to use it repeatedly for multiple cycles without losing its effectiveness. It is crucial for its scalability in industrial usage, its sustainability, and economic viability. Here, stable colloidal dispersion of nanoparticles was used, which can get unstable over time due to material loss, ligand stripping, irreversible aggregation, and permanent precipitation.

##### Dip-Catalyst Solution

###### Principle

The dip-catalyst system is used to demonstrate the recyclability of the photocatalyst, as it is not possible to separate the photocatalyst from the reaction mixture after each cycle, unlike in heterogeneous catalysts. There is a possibility of loss of material and loss of ligands from the QD surface, which can greatly impact the next cycle. In the dip-catalyst system, the colloidal catalyst is converted into a supported catalyst on a solid surface, creating a true heterogeneous condition where the catalyst can be physically attached and handled easily.

###### Materials used:

- 2 cm×1 cm Whatman filter paper: high-quality chemically inert laboratory papers
- OAm-InP QDs
- 0.5mM KNO<sub>2</sub> aqueous solution
- Ion chromatography device

###### Procedure:

- Small controlled droplets of OAm-InP QD solution are carefully placed on the surface of the filter paper. QDs get caught between the cellulose fibers of the paper.

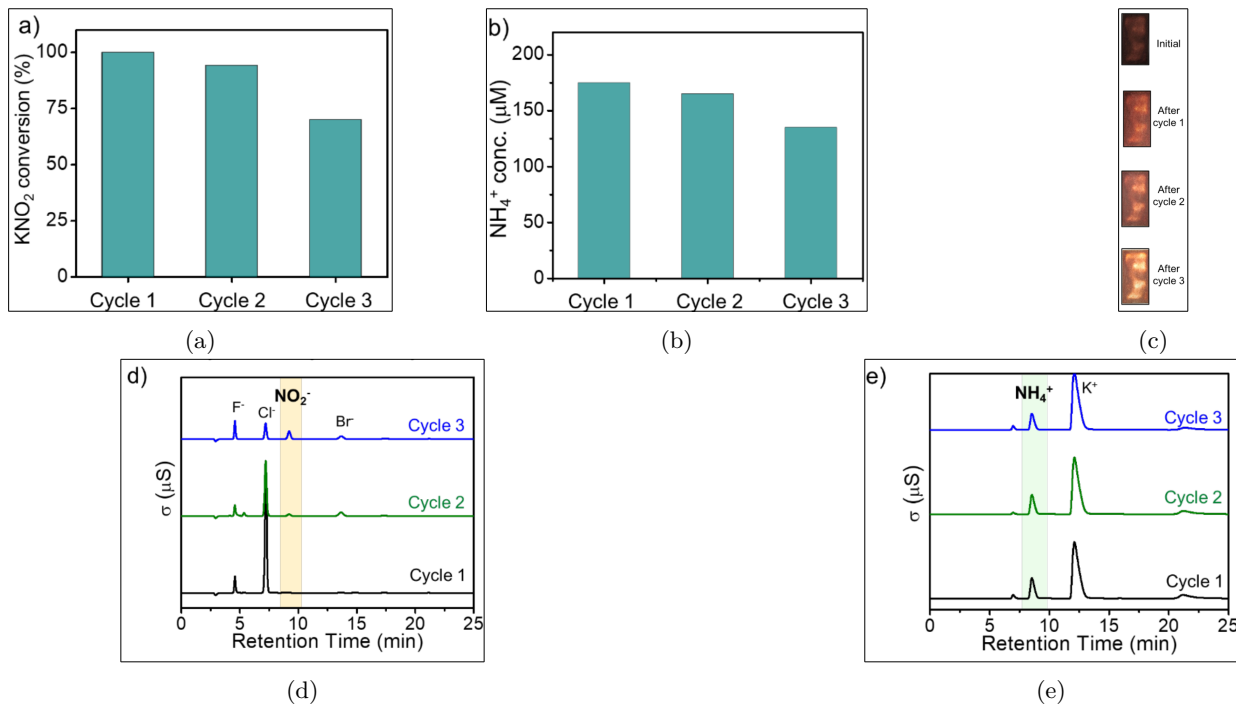


Figure 37: (a) Recyclability for NO<sub>2</sub><sup>-</sup> conversion up to three cycles. (b) Recyclability for NH<sub>4</sub><sup>+</sup> production up to three cycles. (c) Optical photographs of the InP QDs-loaded paper film after each cycle. (d) Anion chromatograms after each cycle. (e) Cation chromatograms after each cycle.

- The solvent slowly evaporates, leaving QDs physically anchored to the paper fibers. Complete removal of residual solvent is crucial.
- The paper is then carefully dipped in the fresh aqueous reaction mixture containing KNO<sub>2</sub>. Reactants can reach the [+] in p QDs through the porous surface.
- It is then irradiated with 450 nm LED lights under optimized conditions for exactly 6 hours, accounting for mass transfer limitations. Immobilized QDs have slightly reduced surface accessibility. The paper matrix may also reduce the photon flux.
- The film was removed using tweezers, washed using distilled water to remove residual products and unreacted substrate, dried under controlled conditions for the next cycle, and analyzed using IC.

#### Analysis:

On analyzing using IC, it is found that the efficiency is slightly reduced over time, with a drastic reduction after the third cycle. The NO<sub>2</sub><sup>-</sup> conversion efficiency is found to be 100%, 95%, and 70% after the first, second, and third cycles, respectively. The ammonia production shows a parallel trend with the NO<sub>2</sub><sup>-</sup> conversion. This confirms that the catalyst is becoming less effective over time. It is visually evident with the progressive discoloration of the QD-loaded film from deep orange to pale yellow.

#### 3.13.2 With Core/Shell InP QDs

As discussed above, core-only InP QDs are highly efficient for photocatalytic conversion, but efficiency reduces drastically over time due to surface etching. Coating the InP core with a shell of ZnS protects the core from direct contact with the surrounding solution, reducing the rate of surface etching. This is a type-I core/shell QD. It covers up the surface defects that could lead to instability. The charge carriers are confined within the core of InP due to the high energy barrier of the ZnS shell, which enhances its stability but makes it harder for the charge carriers to move to the surface for reaction participation. This overall reduces the yield of the photocatalytic conversion by 50% compared to only core-only InP QDs. Ethanol(E<sup>0</sup> = -4.66 eV) is an efficient hole scavenger as it reacts with holes more easily than water(E<sup>0</sup> = -5.67 eV). In addition, conversion efficiency jumped back up to 100%. It maintains the performance of core-only InP QDs but with better stability. As the reaction proceeds, ethanol is oxidized to acetaldehyde by reacting with the holes in the QDs, confirmed by a strong signal in the mass spectrometer ( $\frac{m}{z} = 44$ ) of gas phase analysis. It is harmless in this context. This made ethanol an ideal hole scavenger. The UV-visible studies show that the spectrum hardly changed over 36 hours (6 cycles, each of 6 hours) of continuous light irradiation under optimized conditions, showing that optical properties and the structure of the QDs remain intact. The colors remain constant in the dip-catalyst system as well, confirming the high stability of the core/shell InP QDs with ethanol compared to core-only InP QDs. The conversion rate of higher than 95% was found up to 4 cycles, and 75% activity was retained

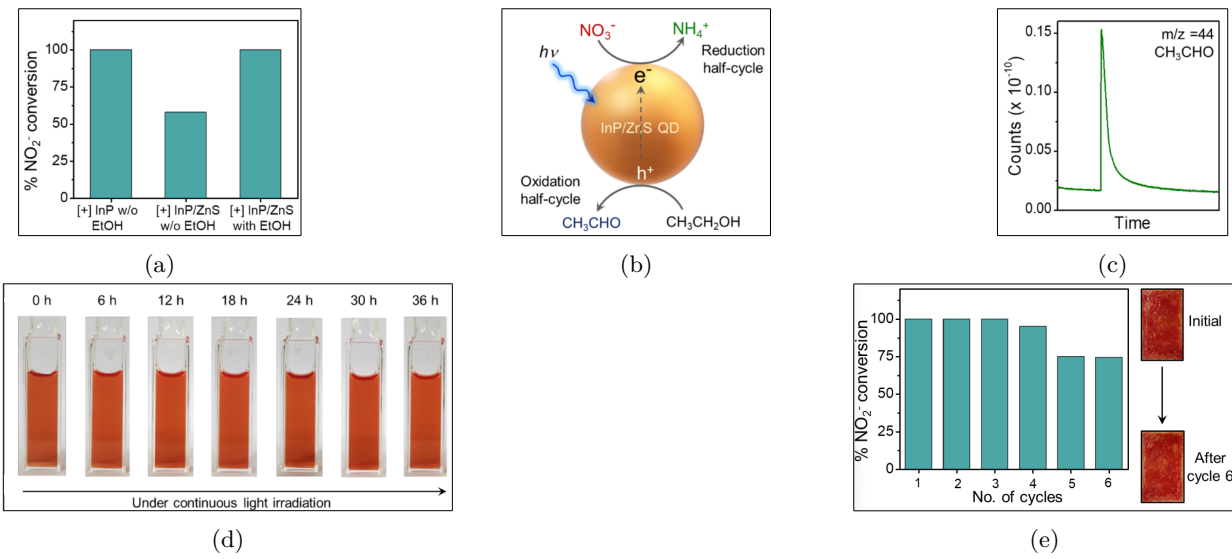


Figure 38: (a) Effect of ethanol (additional hole scavenger) on the photocatalytic activity. (b) Schematics of reduction and oxidation half-cycles with InP/ZnS QDs in the presence of ethanol. (c) Gas-phase mass analysis of the reaction was performed with ethanol. (d) Time-dependent absorption spectra of the reaction mixture with [+] InP/ZnS, KNO<sub>3</sub>, and ethanol. (e) Recyclability studies with a paper-based dip-catalyst system.

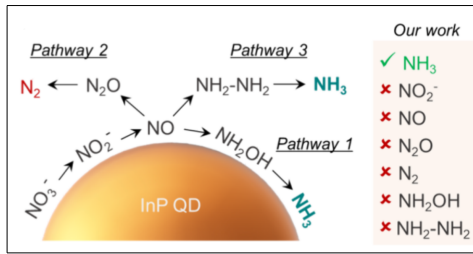


Figure 39: Schematic representation of the three major pathways involved in photocatalytic reduction of NO<sub>3</sub><sup>-</sup>

up to 6 cycles. This improves the recyclability and thus scalability of the technique, making it a potential candidate for cost-effective and practical real-world applications.

### 3.14 Proposed Reaction Mechanism

#### 3.14.1 Understanding the Operating Pathway

Based on previous studies, the photocatalytic conversion of nitrate to ammonia with [+]InP QDs can proceed through three pathways:

- **Pathway 1:**  $\text{NO}_3^-(\text{aq}) \rightarrow \text{NO}_2^-(\text{aq}) \rightarrow \text{N}_2(\text{g})$
- **Pathway 2:**  $\text{NO}_3^-(\text{aq}) \rightarrow \text{NO}_2^-(\text{aq}) \rightarrow \text{N}_2\text{H}_2(\text{aq}) \rightarrow \text{NH}_4^+(\text{aq})$
- **Pathway 3:**  $\text{NO}_3^-(\text{aq}) \rightarrow \text{NO}_2^-(\text{aq}) \rightarrow \text{NH}_2\text{OH}(\text{aq}) \rightarrow \text{NH}_4^+(\text{aq})$

Understanding the exact pathway is important as it will help in designing better catalysts and optimizing the reaction conditions for higher efficiency. As discussed earlier (see 3.8.1), there was no detection of nitrogen gas in the gas phase analysis<sup>25,51</sup>. This rules out pathway 1. So, the reaction must go through either hydrazine or hydroxylamine as intermediates, ultimately forming ammonia. To figure out which pathway is operating, each suspected intermediate, N<sub>2</sub>H<sub>2</sub> and NH<sub>2</sub>OH, is used as the starting reactant under optimized conditions with [+]InP QDs. If the [+]InP QDs convert the intermediate used as starting material instead of NO<sub>3</sub><sup>-</sup>, then this could be an intermediate in the main pathway. From IC, both materials appear to exhibit a strong NH<sub>4</sub><sup>+</sup> peak simultaneously. It means that under the optimized conditions, both the hydrazine and hydroxylamine are efficiently converted to ammonia by the [+]InP QDs, making it challenging to tell which pathway is primarily followed in the photocatalytic conversion of nitrate to ammonia. Due to first-order kinetics, the accumulation of intermediates is inhibited, and hence, they remain undetected. For direct evidence for the reaction pathway, in situ techniques are required, which remain an active area for future research.



Figure 40: (a) Cation chromatograms showing the [+] InP photocatalyzed formation of  $\text{NH}_4^+$  from  $\text{N}_2\text{H}_2$  as the starting reactant. (b) Cation chromatograms showing the [+] InP photocatalyzed formation of  $\text{NH}_2\text{OH}$  from  $\text{N}_2\text{H}_2$  as the starting reactant.

Photocatalyst	$\text{NH}_4^+$ conc.	Catalyst amount	Time	Light source	Hole scavenger	AQY
[+] InP QD (this work)	$490 \mu\text{mol g}^{-1}$ ( $\text{NO}_2^-$ to $\text{NH}_3$ )	19.6 mg	2 h	450 nm (Visible)	None	1.45% @450 nm
	$830 \mu\text{mol g}^{-1}$	19.6 mg	1 h	450 nm (Visible)	None	3.7% @450 nm
$\text{CuPd/TiO}_2$ <sup>32</sup>	$383 \mu\text{mol g}^{-1}$	100 mg	5 h	365 nm (UV)	MeOH	0.22% @365 nm
$\text{JRC-TiO}_6$ <sup>33</sup>	$384 \mu\text{mol g}^{-1}$	100 mg	24 h	UV	$\text{HCOOH}$	-
$\text{BaO-TNS}$ <sup>34</sup>	$89.8 \mu\text{mol g}^{-1}$	1 mg	12 h	UV	Ethylene glycol	0.53% @524.5 nm
$\text{Cu}_2\text{O}$ sub-nano clusters <sup>35</sup>	$3.1 \text{ mmol g}^{-1}$	2 mg	-	Simulated solar	$\text{HCHO}$	-
$\text{CdSe}$ QD <sup>20</sup>	$73.8 \mu\text{mol h}^{-1}$	2 mg	2 h	Full spectrum	Ascorbic acid	-
$\text{CdSe}$ QD <sup>20</sup>	$47 \text{ mmol g}^{-1}$	2.35 mg	2 h	440 nm (Visible)	Ascorbic acid + Na ascorbate	5.45% @440 nm
$\text{CuInS}_2$ QD <sup>20</sup>	$40 \text{ mmol g}^{-1}$	34 mg	60 h	Simulated solar	-	-

Table 6: Comparison of various photocatalysts and their respective performances.

### 3.14.2 Performance Comparison with Other Photocatalysts

As observed above, [+] InP QDs work under visible light, with no added hole scavengers, and have a high apparent quantum yield. Many other catalysts need UV light or require sacrificial hole scavengers. While our AQY (1.45%) is competitive among visible-light catalysts, it remains lower than CdSe-based systems (5.45%), highlighting a trade-off between efficiency and CdSe's toxicity.

## 3.15 Comparative Assessment with Haber-Bosch

The traditional, industrially used Haber Bosch process operates at high temperatures of  $400 - 500^\circ\text{C}$  and very high pressures of 150-300 atm. For the process, iron-based, highly robust catalysts are used. It produces ammonia at a global scale exceeding 150 Mt per year. However, this process is highly energy-intensive (approximately 35 GJ per ton of ammonia) and is a significant source of carbon dioxide emissions (approximately 2.0 tons of carbon dioxide per ton of ammonia produced) due to its reliance on hydrogen derived from fossil fuels. On the contrary, the visible-light driven photocatalytic conversion using [+] InP QDs operates under ambient conditions using nitrate as the nitrogen source. This approach has a high selectivity (94%) for ammonia formation and no direct carbon dioxide emissions, making it inherently more sustainable. However, its current quantum efficiency (1.45% for nitrate reduction) is significantly lower than the energy efficiency of Haber-Bosch. The process is limited to laboratory scale, with catalyst recyclability up to only six cycles before significant deactivation. Additionally, the requirement for ethanol as a sacrificial electron donor, which is oxidized to acetaldehyde, introduces further operational complexity and cost. While the InP QD photocatalytic method presents a promising, low-carbon alternative for decentralized and small-scale ammonia production, substantial improvements in efficiency, scalability, and catalyst stability are necessary before it can compete at an industrial level.

The Haber-Bosch process currently produces ammonia at an estimated cost of approximately 195197 per tonne, primarily due to its high energy consumption and the need for high-pressure, high-temperature operation using fossil fuel-derived hydrogen. The photocatalytic nitrate-to-ammonia approach using InP quantum dots offers significant potential cost advantages by operating under ambient conditions and harnessing visible light, including natural sunlight, thus potentially reducing energy expenditure. Moreover, the elimination of hydrogen gas feedstock and high-pressure reactors can lower capital and operational costs. However, current catalyst synthesis costs, moderate photocatalytic efficiency (apparent quantum yield of 1.45%), and limited scalability remain challenges that need addressing. Nonetheless, with ongoing improvements in catalyst design and process optimization, this method holds promise for more cost-effective, decentralized ammonia production. Comprehensive techno-economic assessments are recommended to validate and quantify economic feasibility at scale.

## 4 Conclusion

This study demonstrates that surface-engineered InP QDs achieve an exceptional 94% ammonia selectivity and an apparent quantum yield of 1.45% for nitrate reduction (and 3.7% for nitrite) under 450 nm visible light irradiation at room temperature. Under optimized conditions, ammonia yields of up to  $300 \mu\text{mol g}^{-1}\text{h}^{-1}$  were obtained, with robust performance even under natural sunlight. Despite these advances, several challenges remain. The photocatalyst's recyclability is currently limited to six cycles, with a gradual decline in activity attributed to surface oxidation and ligand degradation. Additionally, the need for ethanol as a sacrificial hole scavenger introduces operational complexity and cost, as ethanol is oxidized to acetaldehyde during the process. Future research should focus on improving QD stability, developing alternative, more sustainable hole scavengers, and scaling up the synthesis of InP QDs for industrial applications. The size-dependent optical properties of QDs offer unique opportunities for enhanced solar spectrum utilization. By employing multiple QDs with different sizes or compositions, it is possible to cover a broader range of the solar spectrum compared to a single QD system. For instance, smaller InP QDs absorb higher energy photons (blue/UV region), while larger QDs or different compositions (such as InAs or CdSe) can capture longer wavelengths. This approach, similar to tandem solar cell architectures, could potentially maximize photon absorption and improve overall photocatalytic efficiency for ammonia synthesis. Recent studies have demonstrated that heterostructured QD systems combining different materials show enhanced photocatalytic performance through complementary absorption ranges and improved charge separation. While the achieved selectivity and quantum yield represent a significant improvement over traditional UV-driven systems and other visible-light photocatalysts, they still fall short of the efficiency, durability, and cost-effectiveness required for commercial ammonia production. The Haber-Bosch process, for example, operates continuously for years with conversion efficiencies above 90% and established supply chains. To compete industrially, photocatalytic systems must demonstrate long-term stability, higher turnover numbers, and economic viability at scale. While recyclability remains limited (6 cycles), core/shell QDs with ethanol scavengers improve stability. Future work must address long-term catalyst degradation for industrial adoption. In summary, this work establishes InP QDs as a highly promising platform for visible-light-driven, selective ammonia synthesis from nitrate, achieving 94% selectivity and 1.45% quantum yield under ambient conditions. However, further innovations are needed to address limitations in catalyst durability, process scalability, and overall economic competitiveness. Bridging these gaps will be essential for translating this laboratory breakthrough into a practical, sustainable alternative to the energy-intensive Haber-Bosch process.

## Acknowledgement

I sincerely thank Prof. Pramod Pilai for the opportunity to work on this reading project and for his guidance through the selected research articles. I am also thankful to the Nano Alchemy Lab for making their published work accessible, which was crucial for this reading project.

## Author Information

Agam Baruah  
BSMS Student (20241017)  
Indian Institute of Science Education and Research (IISER), Pune 411008, India  
<https://orcid.org/0009-0007-2514-9994>  
Email: agam.baruah@students.iiserpune.ac.in

## A Technical Concepts and Background

### A.1 Anisotropy

Anisotropy refers to the property of being directionally dependent, i.e., a system exhibits different physical properties when measured along different directions. (in contrast to Isotropy) In a QD, the mobility of charge carriers and the efficiency of charge separation can vary with the direction, which affects its photocatalytic properties. The surface structure of QDs may be anisotropic, meaning that certain crystal facets/directions are more catalytically active than others.

### A.2 Carrier Mobility

Carrier mobility of a material refers to the property that allows the flow of charge carriers when an electric field or driving force is applied. Here, charge carriers are generated when QDs absorb light. For these photogenerated carriers to participate in the chemical reactions, they are required to reach the surface before recombination; thus, having high carrier mobility is important for the process<sup>44</sup>.

Modern Group	Old IUPAC	Examples
1	I A	H, Li, Na, K, Rb, Cs, Fr
2	II A	Be, Mg, Ca, Sr, Ba, Ra
3	III B	Sc, Y
4	IV B	Ti, Zr, Hf, Rf
5	V B	V, Nb, Ta, Db
6	VI B	Cr, Mo, W, Sg
7	VII B	Mn, Tc, Re, Bh
8	VIII	Fe, Ru, Os, Hs
9	VII H	Co, Rh, Ir, Mt
10	VIII	Ni, Pd, Pt, Ds
11	IB	Cu, Ag, Au, Rg
12	II B	Zn, Cd, Hg, Cn
13	III A	B, Al, Ga, In, Tl, Nh
14	IV A	C, Si, Ge, Sn, Pb, Fl
15	V A	N, P, As, Sb, Bi, Mc
16	VIA	O, S, Se, Te, Po, Lv
17	VII A	F, Cl, Br, I, At, Ts
18	0	He, Ne, Ar, Kr, Xe, Rn, Og

Table 7: Periodic table group numbering systems (modern vs. old)<sup>33</sup>

### A.3 Classes of QDs

- **II–VI QDs:** Made from group II and group VI elements. e.g., CdSe, ZnS
- **III–V QDs:** Made from group III and group V elements. e.g., InP, GaAs
- **I–III–VI QDs:** Made from elements in group I, group III, and group VI elements. e.g., CuInS<sub>2</sub>, AgInS<sub>2</sub>

### A.4 Core-only QDs

Core-only InP is used to enhance charge separation while minimizing interface trap states.

### A.5 Effective Mass

Electrons in a crystal experience forces not only from external forces but also from the lattice itself. The actual mass of an electron ( $m_e$ ) is  $9.1 \times 10^{-31}$  kg, whereas the effective mass of an electron is the mass it appears to have, accounting for the interactions, treating it as a free particle with a modified mass.

$$E = \frac{\hbar^2 k^2}{2m_e} \quad (16)$$

where,

E: Energy of the particle

k: wave vector

$m_e$ : mass of an electron

$\hbar$ : reduced Planck constant

From the dispersion relation,

$$\frac{\delta E}{\delta k} = \frac{\hbar^2 k}{m_e} \quad (17)$$

or,

$$\frac{\delta^2 E}{\delta k^2} = \frac{\hbar^2}{m_e} \quad (18)$$

so,

$$m^* = \frac{\hbar^2}{\frac{\delta^2 E}{\delta k^2}} \quad (19)$$

A flatter band results in a larger effective mass, while a sharply curved band leads to a smaller effective mass. Effective mass varies with crystallographic direction. A charge system with a more covalent nature will have a smaller effective mass, which enhances charge carrier mobility and reduces recombination losses. This also weakens the columbic interactions between the electrons and holes, thus enabling efficient carrier participation in redox transformation<sup>48</sup>.

### A.6 Growth of QDs

Growth is the process by which MSCs transform into larger QDs through the addition of monomers or aggregation. There are mainly two growth pathways:

1. Heterogeneous Growth is the direct transformation of MSCs to QDs without intermediate sizes, observed at high temperature.
2. Homogeneous Growth is the continuous growth of MSCs into monomers, which then add to existing QD, producing QDs with a continuum of sizes.

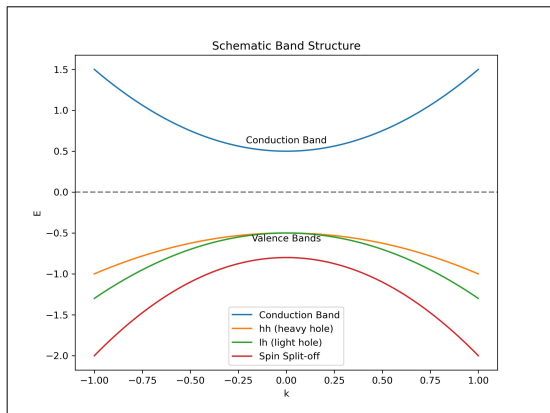


Figure 41: Band alignment in a semiconductor.

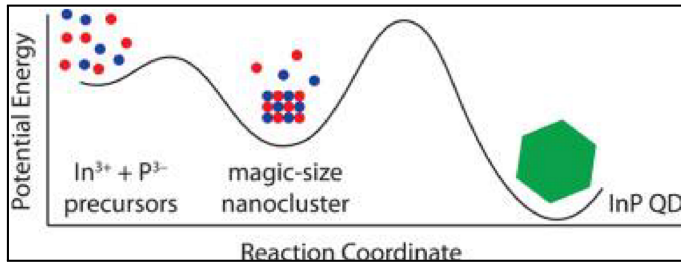
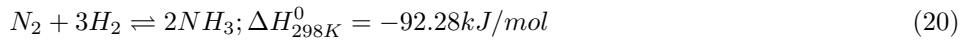


Figure 42: Two-step nucleation mechanism showing MSC intermediate pathway to InP QDs

## A.7 Haber-Bosch Process

The Haber-Bosch process synthesizes ammonia by combining nitrogen and hydrogen gases. Developed by Fritz Haber and later modified by Carl Bosch, the process involves combining nitrogen gas with hydrogen gas (primarily obtained from methane gas) in a 1:3 volume ratio, under a high pressure of 200 atm and a high temperature of 400 to 450°C in the presence of iron catalysts. Reaction mechanism of the Haber-Bosch process:



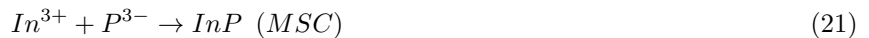
However, the Haber-Bosch process is energy-consuming and carbon-intensive. Sustainable NH<sub>3</sub> production requires discovering new methods for N<sub>2</sub> fixation under ambient conditions. In the past few decades, many efforts have been made to develop catalytic systems for N<sub>2</sub> fixation under mild synthesis conditions to generate NH<sub>3</sub> and other valuable nitrogen-containing materials.

## A.8 Long-lived Charge Separation

The material can keep the photogenerated electrons and holes apart. In QDs, especially when their surface chemistry or composition is engineered (for example, by doping with metals or modifying surface ligands), electrons and holes can become trapped at the surface. This spatial separation creates a kinetic barrier, making it much harder for the electron and hole to recombine, thus greatly extending their lifetimes, sometimes from nanoseconds up to minutes or longer. This enhancement increases the probability of redox participation by charge carriers<sup>68</sup>.

## A.9 Magic-Sized Clusters (MSCs)

MSCs are atomically precise, thermodynamically stable nanoclusters (1-2nm) that form during QD synthesis. They act as intermediaries between molecular precursors and mature QDs. They are stabilized by ligands. They play a crucial role in the nucleation and growth of InP.



They have specific sizes and are observed as a sharp peak in the UV-vis spectrum at a particular wavelength. They exhibit remarkable thermodynamic stability across a wide range of growth temperatures and precursor concentrations. This stability leads to a quantized growth (heterogeneous growth) rather than continuous growth (homogeneous growth) without any preference for a specific size. InP MSCs act as SSPs<sup>11</sup>. These clusters already contain the

<sup>11</sup>Single Source Precursors (SSP): are materials that contain all necessary elements in a single cluster/molecular compounds. They serve as self-contained precursors.



Figure 43: QD structure and size-dependent properties.

correct stoichiometry of In and P, enabling direct conversion of InP QDs under heat. When heated, they decompose or rearrange to release monomers, which nucleate and grow into larger QDs. This bypasses the need for separate  $\text{In}^{3+}$  and  $\text{P}^{3-}$  precursors<sup>23</sup>.

### A.10 Molar Extinction Coefficient

Molar extinction coefficient( $\varepsilon$ ) is the measure of how strongly it absorbs light at a specific wavelength. The higher the  $\varepsilon$ , the more efficient the absorbance of the light energy by the material. By Beer-Lambert law, absorbance(A) is related to the concentration of the material(c) and path length (L) as follows:

$$A = \varepsilon c L \quad (22)$$

where  $A$  is absorbance (dimensionless),  $c$  is concentration (M),  $\varepsilon$  is the molar extinction coefficient ( $\text{M}^{-1}\text{cm}^{-1}$ ) and  $L$  is path length (cm). For a QD, it is crucial to have a high molar extinction coefficient so that it can absorb more photons per unit concentration, making them excellent harvester. More absorbed photons mean higher photocatalytic activity. It also provides an economic advantage as less material will be needed to achieve the same light absorption.

### A.11 Nucleation

Nucleation is the initial step in forming QDs, where atoms/molecules assemble into small, stable clusters that initiate further growth. There are two types of nucleation based on the pathway followed:

Classical nucleation is the random aggregation of atoms/molecules until a critical nucleus size is reached. Once the nucleus exceeds this size, it grows into a larger particle. However, it does not account for stable intermediates like MSCs.

Non-classical nucleation occurs in two steps:

1. Formation of MSCs: Atoms and molecules precisely aggregate to form thermodynamically stable clusters (intermediates).
2. Growth: MSCs either dissolve into monomers or aggregate into QDs.

### A.12 Photostability

It refers to the property of resisting losing its brightness or breaking down, maintaining its structural and functional properties when exposed to light over time. It is crucial for the QDs, as unstable QDs break down under light, losing their catalytic activity. It is important for practical application, as only photostable materials can be used in real-world devices. InP QDs are more photostable than most of the organic dyes, as they often undergo photobleaching under intense light and are relatively environmentally friendlier. Although CdSe has high performance, it is not used due to its toxicity and instability.

### A.13 Quantum Dots (QDs)

QDs are nanometer-sized semiconductor crystals with unique, size-tunable optical and electronic properties due to quantum confinement. They are used in display screens, solar cells, and LEDs. QDs are made of materials such as Indium phosphide (InP) and Cadmium selenide (CdSe)<sup>3</sup>.

### A.14 Quantum Efficiency

The Stark-Einstein law (Photochemical equivalence law):

"Each atom or molecule absorbs a single quantum of light (photon) in the process of getting excited."<sup>43</sup>

Which means:



QDs	Elements	Electronegativity (Pauling scale)	$\Delta$ Electronegativity	Covalency
InP	In	1.78	Smaller (0.41)	High
	P	2.19		
CdSe	Cd	1.69	Large (0.86)	Low
	Se	2.55		
	Cu	1.90		
CuInS <sub>2</sub>	In	1.78	Moderate	Moderate
	S	2.58		

Table 8: Comparison of electronegativity, ionicity, and covalency for different QD materials<sup>12</sup>

where  $h\nu$  represents a photon of light and M\* is the excited molecule.

Quantum efficiency (quantum yield or photochemical equivalence) is defined as:

$$\phi(\%) = \left( \frac{\text{Number of product molecules} \times \text{no. of electrons required}}{\text{Number of absorbed photons}} \right) \times 100\% \quad (24)$$

If the Stark-Einstein law is strictly followed (ideal process), then  $\phi$  will be 100%, but in a real photochemical reaction, it differs.

- $\phi > 1$ : if secondary processes (like chain reactions) allow one photon to lead to the transformation of multiple molecules.
- $\phi < 1$ : if some excited molecules deactivate without producing the product.

Quantum efficiency can be experimentally determined by correlating the number of absorbed photons (measured via light calibration and absorption) with the number of product molecules (here, ammonia) produced (quantified analytically).

### A.15 Relation between Electronegativity and Charge Separation

In InP QDs, the difference in electronegativity between In and P is relatively small, which leads to a more equal sharing of electrons, leading to greater covalency and delocalization of electronic wavefunctions, compared to more ionic QDs such as TiO<sub>2</sub> and ZnS. Additionally, it has a smaller effective mass, i.e., charge carriers can move more freely. Due to higher covalency:

- The wavefunction is more delocalized, resulting in a lower effective mass for electrons and holes, which allows the charge carriers to move more freely, resulting in high charge mobility. High charge mobility means that the charge carriers can reach the surface faster before recombining, increasing the probability of the reduction.
- In QDs, photogenerated electrons and holes are bound by Coulombic interactions. The strength of the Coulombic forces between the electrons and holes depends on the distance between them:

$$F = \frac{e^2}{4\pi\epsilon_0 r^2} \quad (25)$$

Where r: the average separation between the charge carriers.

Delocalization of the wavefunction increases the average separation ( $r$ ) between charge carriers, which weakens the Coulombic interactions in InP compared to II-VI and I-III-VI QDs. This enables efficient charge separation and reduces recombination in the QD, which is critical for multi-electron processes like photocatalysis.

### A.16 Retention

Retention percentage is the measure of how much of the initial photocatalytic activity remains after a certain number of cycles:

$$\text{Retention} = \frac{\text{Absorbance after cycles}}{\text{Initial absorbance}} \quad (26)$$

A high retention percentage means the catalyst is stable and reusable. Absorbance quantifies how much light a material absorbs at a specific wavelength, which can be measured by UV-Vis spectroscopy to determine its light-harvesting capability.

### A.17 Surface Chemistry Tunability

The surface of QDs can be chemically modified by changing ligands and surface treatments to optimize interactions with reactants and suppress unwanted side reactions. This allows for the creation of a microenvironment that promotes high selectivity and efficiency in photocatalytic processes<sup>63</sup>.

## A.18 Tunable Electronic Properties

QDs have electronic and optical properties that can be precisely adjusted by changing their size, shape(spherical, rod-like, disk-shaped, or having more complex geometries), and composition. When the size of a QD is changed, the energy gap between its electronic states also changes. Smaller QDs have larger energy gaps and emit bluer (higher-energy) light, while larger dots emit redder (lower-energy) light. This is called "quantum confinement." This also allows scientists to design QDs for specific applications, such as different colors in display screens, targeted bioimaging, or efficient solar cells<sup>1,22,30,37</sup>.

## A.19 Valence Bond Theory

Valence Bond (VB) theory is based on the highest energy level filled with electrons at 0 K. The **Conduction Band (CB)** is the lowest energy level where electrons can move freely. The energy difference between the two levels is called the **Band gap ( $E_g$ )**.

# B Analytical and Instrumental Techniques

## B.1 Electrochemical Setup For Determination of Band Positions

Electrochemical setup:

- Working electrode [the reaction occurs here]: glassy carbon (coated with InP QDs).
- Reference electrode: Ag/AgNO<sub>3</sub> in acetonitrile (calibrated using ferrocene)
- Counter electrode [to complete the circuit]: Pt wire
- Internal standard: Ferrocene
- Electrolyte: 0.1 M tetrabutylammonium hexafluorophosphate (TBAF) in acetonitrile.

## B.2 Fourier Transform Infrared Spectroscopy (FTIR)

Fourier Transform Infrared Spectroscopy is a powerful analytical technique to identify chemical compounds based on their vibration while interacting with infrared light. In this report, it is described to be used in the confirmation of the binding mode of ligands on the InP QD surface<sup>56</sup>.

### B.2.1 Basic Principles of FTIR

The infrared light, corresponding to the energy needed to excite molecular vibrations, is a region of the electromagnetic spectrum. When molecules absorb infrared radiation, they undergo various vibrational motions as chemical bonds between any two atoms act as a spring. The vibrations can be stretching or bending.

## B.3 Gas Chromatography

### B.3.1 Principle

Gas chromatography separates compounds based on their volatility and interaction with a stationary phase<sup>46</sup>.

### B.3.2 Key Components

1. **Injection system:** Introduces the sample into the carrier gas system and controls sample volume and injection reproducibility. It is maintained at a high temperature (150°C–300°C) for sample vaporization.
2. **Carrier gas system:** Provides an inert mobile phase (to prevent reactions with analyte). It helps transport vaporized samples through the column.
3. **Separation column:** Consists of capillary columns (15–100 m) containing a stationary phase (liquid polymer) coated on the column walls.
4. **Detection system:** Measures compounds as they elute from the column.

### B.3.3 Thermal Conductivity Detector (TCD)

The TCD measures the change in thermal conductivity between the carrier gas and the column effluent. It can detect virtually any compound with thermal conductivity different from the carrier gas (reference)<sup>10</sup>.

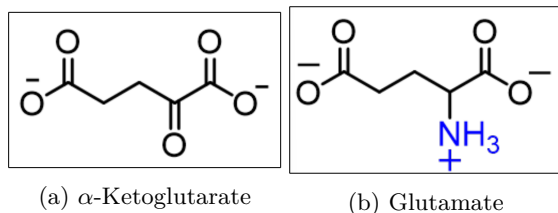


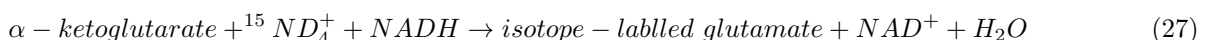
Figure 44: Structures of  $\alpha$ -Ketoglutarate and Glutamate.

## B.4 Glutamate dehydrogenase (GLDH) Assay

Glutamate dehydrogenase is a hexameric enzyme<sup>12</sup> that catalyzes the reversible conversion of glutamate to  $\alpha$ -ketoglutarate and ammonia while reducing NAD(P) to NAD(P)H<sup>45</sup>. In the context of photocatalytic conversion of nitrate to ammonia, it provides unambiguous evidence of water being the sole proton source<sup>36</sup>.

### B.4.1 Mechanism

The fundamental reaction catalyzed by GLDH<sup>18,45</sup>:



It is thermodynamically favorable because it operates in the reductive amination direction, where  $\alpha$ -ketoglutarate acts as an electron acceptor and ammonia as a nitrogen source<sup>47</sup>. The enzyme contains active binding sites for each of the substrates. The GLDH-catalyzed reaction proceeds through several discrete molecular steps<sup>7,47</sup>:

1. **Substrate binding:**  $\alpha$ -ketoglutarate first binds to the enzyme, inducing a conformational change that creates the ammonium binding site.
2. **coenzyme Recognition:** NADH binds to its specific active binding site in the enzyme
3. **Imine formation:** The ammonium ion attacks the carbonyl carbon of  $\alpha$ -ketoglutarate, forming an  $\alpha$ -iminoglutarate intermediate
4. **Hybride Transfer:** NADH transfers a hybrid ion to the imine carbon, simultaneously converting to NAD<sup>+</sup>
5. **Protonation:** The resulting carbanion is protonated to form the final glutamate product.

### B.4.2 Components and Their Roles

#### GLDH

It catalyzes the reversible conversion of glutamate to  $\alpha$ -ketoglutarate. The enzyme concentration of 1.2 units provides optimal catalytic activity for the assay<sup>13</sup>.

#### B.4.3 NADH

It serves as the reducing cofactor, providing electrons for the reductive amination reaction. The  $6\mu\text{M}$  concentration is carefully optimized for the conversion.

#### B.4.4 alpha-Ketoglutarate

It provides the carbon framework that will be transformed into glutamate<sup>11</sup>. The  $20\mu\text{M}$  concentration ensures adequate substrate availability.

#### B.4.5 Analysis

##### UV-Visible Spectroscopy

UV-Visible Spectroscopy is used for the monitoring of the reaction progress after incubation of the reaction mixture at  $25^\circ\text{C}$  for 6 hours for the formation of glutamate.

1.  $\lambda_{\text{NADH}} = 340 \text{ nm}$
2.  $\lambda_{\text{NAD}^+} = 259 \text{ nm}$

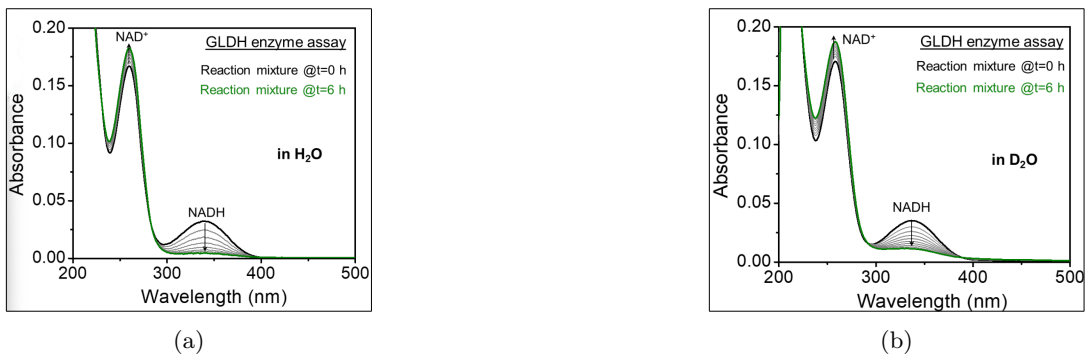


Figure 45: (a)UV-vis absorption spectra of GLDH assay proving the formation of glutamate in the presence of  $\text{NH}_4^+$  (in  $\text{H}_2\text{O}$ ) produced during the photocatalytic reaction. (b)UV-vis absorption spectra of GLDH assay proving the formation of glutamate in the presence of isotope-labeled  $^{15}\text{ND}_4^+$  (in  $\text{D}_2\text{O}$ ) produced during the photocatalytic reaction.

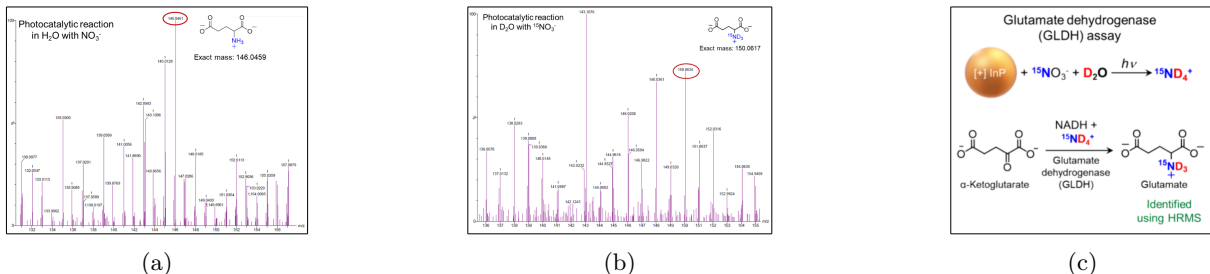


Figure 46: (a)HRMS of glutamate formed from photocatalytically generated  $\text{NH}_4^+$  with  $[+]$ -InP QDs and  $\text{NO}_3^-$  in  $\text{H}_2\text{O}$ . (b)HRMS of isotope-labeled glutamate formed from  $^{15}\text{ND}_4^+$  generated by reaction in  $\text{D}_2\text{O}$  with  $^{15}\text{NO}_3^-$ . (c)Schematic showing the photocatalytic reduction of  $^{15}\text{NO}_3^-$  to  $^{15}\text{ND}_4^+$  with  $[+]$ -InP QDs in  $\text{D}_2\text{O}$ .

As observed in the graph above, the peak at 340 nm corresponding to NADH decreases as NADH is consumed, whereas the peak at 259 nm corresponding to  $\text{NAD}^+$  increases as  $\text{NAD}^+$  accumulates, thereby proving the formation of glutamate. **High-Resolution Mass Spectrometry (HRMS)**

High-resolution mass spectrometry studies provide the ultimate confirmation of isotopic incorporation by detecting the mass differences with precision sufficient to differentiate among the isotopic variants<sup>65</sup>. The natural abundance Glutamate ( $\text{C}_5\text{H}_9\text{NO}_4$ ) has the exact mass<sup>14</sup> of 147.0532 Da whereas the  $^{15}\text{N}$ -labeled Glutamate ( $\text{C}_5\text{H}_{15}\text{NO}_4$ ) has the exact mass of 148.0503 Da. When the reaction is performed in  $\text{D}_2\text{O}$ , the glutamate can also incorporate deuterium atoms with each deuterium adding approx. 1.0063 Da to the exact mass. The HRMS instrument analyzes the glutamate and looks for an isotopic pattern. The graph 46a provides a definite proof that the protons came from  $\text{D}_2\text{O}$  and the nitrogen came from  $^{15}\text{NO}_3^-$  as researchers observe the base peak shifts from 147.0532 Da to 148.0503 Da.

## B.5 $^1\text{H-NMR}$ Spectroscopy

Proton nuclear magnetic resonance spectroscopy is a powerful analytical technique used to determine the molecular structure of organic compounds by analyzing the behavior of protons in a magnetic field. Protons possess an intrinsic quantum property called spin, which generates their magnetic moment. In the presence of a magnetic field, these nuclei align in certain directions. The energy difference between these energy states depends on the magnetic field strength:

$$\Delta E = \gamma \hbar B_0 \quad (28)$$

where  $\gamma$  is the gyromagnetic ratio and  $\hbar$  is the reduced Planck's constant.  $\gamma B_0 (= w)$  is called Larmor frequency. When exposed to radio wave pulses matching the Larmor frequency, protons absorb energy, and the transition between the spin states occurs, which is detected as a signal.

## B.6 Ion Chromatography (IC)

Ion chromatography, or IC, separates and quantifies ions (charged particles) in a solution. It has two flow paths:

- One that analyses anions like  $\text{NO}_2^-$ ,  $\text{NO}_3^-$

<sup>12</sup>hexameric enzyme is a protein catalyst composed of six subunits to form a functional complex.

<sup>13</sup>One unit of GLDH is defined as the amount that is required to catalyze the conversion of 1  $\mu\text{mol}$  of glutamate to  $\alpha$ -ketoglutarate per minute at pH of 8.2<sup>54</sup>

<sup>14</sup>Exact mass is the precise mass of a molecule calculated using the mass of the most abundant isotope of each element in its chemical formula.

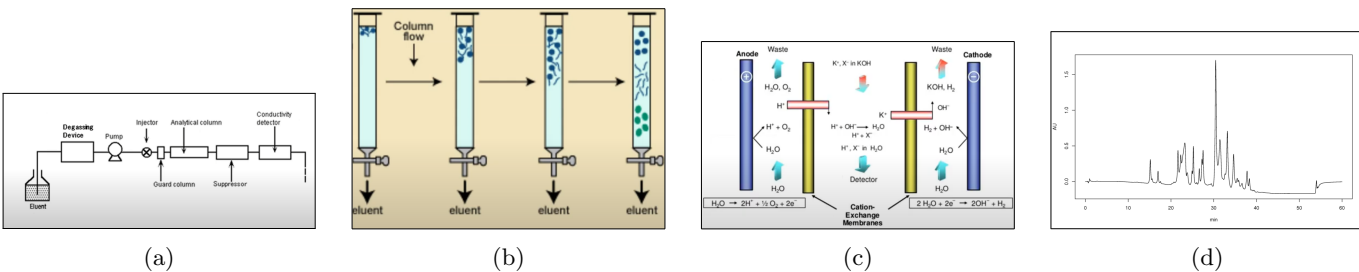


Figure 47: (a)Basic overview (b)Analytical column (c)Suppressor (d)Sample chromatogram

- One that analyses cations like  $\text{K}^+$ ,  $\text{NH}_4^+$

While preparing the samples, it is important to make sure they are in the appropriate concentration range. Normal IC operation measures most ions between 1 ppb and 100 ppm. The IC measures more accurately for lower concentrations than higher concentrations, as very high concentrations may overload the column, resulting in bad results and potentially damaging the device. High concentrations of undesired ions can also interfere with the measurement of the desired ion concentration. Thus, it is always important to dilute with water based on the ion having the highest concentration. It is essential to filter them. For filtration,  $0.45 \mu\text{m}$  or lower syringe filters are usually used. Centrifugation is also sometimes used. The Eluent goes through a degasser, which removes gas to avoid air bubbles in the system, then the pump, which forces the flow of the eluent through the system, then the injector, guard column, which removes the undesired species like heavy metals, an analytical column, a suppressor, and a conductivity detector. The eluent is the mobile phase that flows through the system as it is pushed by the pumps. Some ICs require the eluent to be made before use, while some require nanopure water that flows through an EGC or eluent generator cartridge, which uses an electrolytic chamber to turn very concentrated eluent into a more diluted eluent. Anion columns use a base eluent (eg, KOH), whereas cation columns use an acid eluent (eg, MSA(methanesulfonic acid)). Carbonate or bicarbonate eluents are also common. It acts as a liquid magnet to push ions out of the column. The autosampler is a tray and needle system that draws the sample into the sample loop. The injector is a multi-port device that will change positions when the sample is ready to be injected into the column. The analytical column is made up of either anion exchange or cation exchange resin. The ions bind to the resin, and the eluent pushes ions off the resin. Ions with higher affinity take a longer time to come out, which depends on their size, charge, and electronegativity. Increase eluent concentrations over time to elute(push them off) ions. The ions can be identified, based on the time at which they will come out.

A suppressor is used to remove background conductivity from the eluent due to the acids and bases added. It uses various electrolytic reactions and semi-permeable membranes that convert the eluent into water and waste. The only thing passing through the suppressor is nanopure water and separated ions. Setting the suppressor current too high can result in seeing no peaks at all, and setting the suppressor current too low can result in ridiculous-looking massive peaks and a ton of background noise. The conductivity detector measures conductivity as ions pass through the column to make peaks. The area under the peaks corresponds to the concentration of that ion, based on the calibration curves. Chromatograms (graphs of peaks vs. time) are used to get the results.

## B.7 Mass Spectrometric (MS) Analysis

It is a powerful technique that identifies and quantifies molecules by measuring their mass-to-charge ratio ( $m/z$ ). With the help of an ionization source, neutral molecules are converted into charged ions by bombarding molecules with electrons or using high voltage to spray charged droplets. Ions often break apart into fragments. Using a mass analyzer, the molecules are separated based on their  $m/z$  using electromagnetic fields while the detector records the number of ions at each  $m/z$  value to produce a mass spectrum.

## B.8 X-ray Photoelectron Spectroscopy (XPS)

X-ray Photoelectron Spectroscopy (XPS) is an analytical technique used to determine the elemental composition and chemical state of a material by measuring the kinetic energy of the electrons ejected when illuminated with X-rays.

### B.8.1 Fundamental Principles

When a material is irradiated by X-rays, photoelectrons are ejected as they overcome the work function associated with the material. The kinetic energy of each ejected electron is given by

$$KE = h\nu - E_{Binding} - \phi \quad (29)$$

where,

- $h\nu$ : X-ray photon energy

- $E_{\text{Binding}}$ : Binding energy of the electron, which is a characteristic of each element, electronic orbital, and its electronic environment
- $\phi$ : Work function associated with the material

### B.8.2 Instrumentation

- **X-ray source:** It provides the monochromatic X-rays for irradiation of the material.
- **Sample Stage:** It holds and positions the vacuum-compatible sample.
- **Analyzer:** It separates photoelectrons based on their kinetic energy using electrostatic and magnetic fields.
- **Detectors:** It records the electron spectrum of counts per binding energy value.
- **Vacuum system:** It maintains an ultra-high vacuum to prevent scattering of the ejected electrons.

### B.8.3 Analysis

Each element produces characteristic peaks. The area under each peak, after background subtraction<sup>15</sup>, is proportional to the number of atoms in that chemical state.

## C Experimental Supplements

### C.1 Calculations for the Determination of Band Positions

The following relation can be used to find the absolute energies of the valence and conduction band levels of the QDs.

$$VB = -(E_{\text{peak}} + E_{\text{ref}}) \quad (30)$$

where,

- VB is the valence band position wrt vacuum
- $E_{\text{peak}}$  is the energy corresponding to the oxidation potential peak
- $E_{\text{ref}}$  is the energy corresponding to the relative reference electrode potential

Using the relation,

$$VB_{OAm-InP} = -(0.94 + 4.65) = -5.59 \text{ eV vs vacuum} \quad (31)$$

and,

$$VB_{[+]TMA-InP} = -(0.92 + 4.65) = -5.57 \text{ eV vs vacuum} \quad (32)$$

From the Tauc plots, the band gap of OAm-InP QDs was found to be 2.02 eV and 2.03 eV for [+] TMA-InP QDs. The following relation can be used to calculate the conduction band position:

$$CB = VB + E_g \quad (33)$$

where,

- CB is the conduction band position
- VB is the valence band position
- $E_g$  is the band gap

Thus,

$$CB_{OAm-InP} = -5.59 + 2.02 = -3.57 \text{ eV vs vacuum} \quad (34)$$

$$CB_{[+]TMA-InP} = -5.57 + 2.03 = -3.54 \text{ eV vs vacuum} \quad (35)$$

---

<sup>15</sup>Background subtraction isolates the true photoelectron signal from the extraneous electron counts due to inelastic scattering or noise in the detector.

## C.2 Boltzmann Distribution and Ion Concentration Theory

Boltzmann distribution describes the concentration of  $\text{K}^+$  and  $\text{NO}_3^-$  in the diffused layer of the QDs as follows:

$$c_{\pm} = c_0 e^{\mp \frac{ze\phi}{k_B T}} \quad (36)$$

where,

- $c_+$ : concentration of  $\text{K}^+$
- $c_-$ : concentration of  $\text{NO}_3^-$
- $c_0$ : concentration of  $\text{KNO}_3$  in the bulk, 0.5 mM
- $z$ : valency of the ions
- $\phi$ : surface potential at a given point
- $k_B T$ : thermal energy

Also, the Poisson-Boltzmann equation gives us the variation of the surface potential as a function of distance ( $x$ ) in the diffused layer:

$$\frac{d^2\phi}{dx^2} = -\frac{\rho}{\epsilon} \quad (37)$$

where,

- $\rho$ : charge density
- $\epsilon$ : permittivity of the medium

In a solution containing ions, the charge density arises from the concentration of cations ( $c_+$ ) and anions ( $c_-$ ):

$$\rho = zF(c_+ - c_-) \quad (38)$$

where, F: Faraday constant = 96485 C/mol So, the above equation transforms into:

$$\frac{d^2\phi}{dx^2} = -\frac{zF(c_+ - c_-)}{\epsilon} = \frac{c_0 zF(e^{\frac{ze\phi}{k_B T}} - e^{-\frac{ze\phi}{k_B T}})}{\epsilon} = \frac{2c_0 zF}{\epsilon} \cdot \frac{e^{\frac{ze\phi}{k_B T}} - e^{-\frac{ze\phi}{k_B T}}}{2} = \frac{2c_0 zF}{\epsilon} \sinh\left(\frac{ze\phi}{k_B T}\right) \quad (39)$$

Boundary conditions:

$$\phi(x=0) = \zeta \quad (40)$$

$$\phi(x=\infty) = 0 \quad (41)$$

where,  $\zeta$ : zeta potential and,  $\zeta_{[+]InP} = +25$  mV and  $\zeta_{[-]InP} = -37$  mV Applying Debye-Hückel approximation for dilute solution,  $(\frac{ze\phi}{k_B T}) \ll 1$ , it can be written:

$$\frac{d^2\phi}{dx^2} = \frac{c_0 zF}{\epsilon} \cdot \left[ \left(1 + \frac{ze\phi}{k_B T}\right) - \left(1 - \frac{ze\phi}{k_B T}\right) \right] = \frac{c_0 zF}{\epsilon} \left[ \frac{2ze\phi}{k_B T} \right] = \frac{2c_0 z^2 e F \phi}{\epsilon k_B T} \quad (42)$$

where  $F = eN_A$

so,

$$\frac{d^2\phi}{dx^2} = \frac{2(ze)^2 N_A c_0 \phi}{\epsilon k_B T} \quad (43)$$

where,

$$\kappa^{-1} = \sqrt{\frac{\epsilon k_B T}{2(ze)^2 N_A c_0}} \quad (44)$$

Thus,

$$\frac{d^2\phi}{dx^2} = \frac{\phi}{\kappa^{-2}} \quad (45)$$

where,  $\kappa^{-1}$ : Debye length<sup>64</sup>

Thus,

$$\phi = \zeta e^{-\frac{x}{\kappa^{-1}}} = \zeta e^{-x\kappa} \quad (46)$$

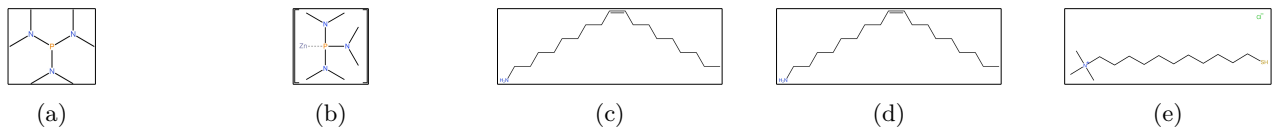


Figure 48: (a)P(DMA)<sub>3</sub> (b)Activated complex (c)OAm structure (d)MUA structure (e)TMA structure

### C.3 Errors and Corrections

#### 1. Typing Error

- **Error:**  $\frac{d^2\phi}{dx^2} = c_0xF\epsilon \left[ \exp\left(\frac{ze\phi}{k_B T}\right) - \exp\left(-\frac{ze\phi}{k_B T}\right) \right]$
- **Page number:** S10, Mathematical expression S9
- **Correction:**  $\frac{d^2\phi}{dx^2} = \frac{c_0zF}{\epsilon} \left[ \exp\left(\frac{ze\phi}{k_B T}\right) - \exp\left(-\frac{ze\phi}{k_B T}\right) \right]$

#### 2. Dimensional Error

- **Error:**  $\frac{d^2\phi}{dx^2} = -\frac{\rho}{\epsilon}$ , where  $\epsilon$  is the dielectric constant of the medium
- **Page number:** S10, Mathematical expressions S9-S10
- **Correction:**  $\frac{d^2\phi}{dx^2} = -\frac{\rho}{\epsilon}$ , where  $\epsilon$  is the permittivity of the medium. And,  $\epsilon = \epsilon_0\epsilon_r$  where  $\epsilon_0$  and  $\epsilon_r$  are the permittivity in free space and dielectric constant of the medium.

#### 3. Symbol Error

- **Error:**  $\kappa$  symbol is used for Debye-length
- **Page number:** S10, Mathematical expressions S11 and S12
- **Correction:**  $\kappa^{-1}$  is the standard symbol used for Debye-length<sup>64</sup>

#### 4. Calculation Error

- Original statement:

"The NH<sub>4</sub><sup>+</sup> production increased by ~48%, with an increase in KNO<sub>3</sub> from 0.25 to 0.5 mM (Figures 2c, S10, and S11)."

- **Issue:** The percentage increase in ammonia was calculated using the final value as the denominator instead of the initial value.

- **Incorrect formula used:**

$$\text{Percentage increase} = \frac{\text{Change in ammonia}}{\text{Final ammonia}} \times 100 = \frac{0.68 - 0.35}{0.68} \times 100 = 48.5\% \quad (47)$$

- **Corrected calculation:**

$$\text{Ammonia at } 0.25 \text{ mM} = 0.35 \mu\text{Smin}, \quad \text{Ammonia at } 0.50 \text{ mM} = 0.68 \mu\text{Smin} \quad (48)$$

$$\text{Increase} = 0.68 - 0.35 \mu\text{Smin} = 0.33 \mu\text{Smin} \quad (49)$$

$$\text{Percentage increase} = \frac{0.33}{0.35} \times 100 = \mathbf{94.29\%} \quad (50)$$

- **Similarly for nitrate conversion:**

$$\text{Nitrate conversion at } 0.25 \text{ mM} = 0.51 \mu\text{Smin}, \quad \text{at } 0.50 \text{ mM} = 1.07 \mu\text{Smin} \quad (51)$$

$$\text{Increase} = 1.07 - 0.51 \mu\text{Smin} = 0.56 \mu\text{Smin} \quad (52)$$

$$\text{Percentage increase} = \frac{0.56}{0.51} \times 100 = \mathbf{109.8\%} \quad (53)$$

### C.4 Materials and Reagents

#### C.4.1 InCl

It acts as a precursor, providing In ions for the synthesis of InP QDs.

#### C.4.2 ZnCl

It serves a dual role in precursor activation and surface passivation. It provides  $Zn^{2+}$  ion, which acts as a Lewis acid, accepting electron pairs from the lone pair of the phosphorus precursor. This coordination polarizes the P-N bonds in the precursor, weakening them and making the phosphorus more electrophilic. The weakened P-N bonds lead to the controlled release of reactive  $P^{3-}$  species into the reaction mixture. The liberated  $P^{3-}$  reacts with  $In^{3+}$  ions to form InP nuclei



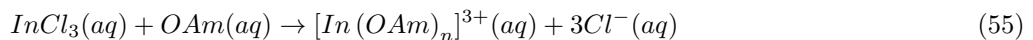
$Zn^{2+}$  coordinates to the InP QD surfaces passivate defects. It also slows the  $In^{3+}$  release for controlled growth, ensuring monodisperse QDs, thereby ensuring uniform, high-quality QDs.

#### C.4.3 Tris(dimethylamino)phosphine

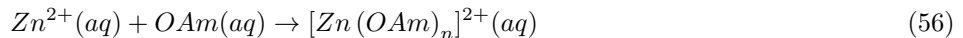
It serves as the phosphorus precursor in the InP QD synthesis. In the presence of a Lewis acid, it forms an activated complex as the Lewis acid coordinates to the lone pair on the phosphorus atom. This weakens the P-N bonds, making them susceptible to cleavage, generating reactive  $P^{3-}$  species. It is less toxic and easier to handle, without requiring any harsh reducing agent, compared to other air-stable alternatives.

#### C.4.4 Oleylamine

Oleylamine( $C_{18}H_{35}NH_2$ ) is a large & heavy (~267.5 g/mol) fatty amine. It has a long hydrocarbon chain with strong van der Waals forces between the molecules. The  $-NH_2$  group can participate in hydrogen bonding, which adds to the intermolecular attractions. This overall increases the boiling point of the molecule. It can be used as a solvent in high-temperature synthesis. It dissolves In and Zn precursors by forming coordination complexes with metal ions to ensure homogeneous mixing and controlled release of  $In^{3+}$  during QD growth. The amine group donates its lone pairs to surface  $In^{3+}$  ions on InP QDs, forming In-N coordination bonds. This reduces surface defects and recombination. The bulky hydrophobic tail creates a steric barrier around the QDs, preventing aggregation and ensuring colloidal stability. Modulating the binding strength of  $In^{3+}$  ions slows the QD growth kinetics, enabling the formation of monodisperse nanoparticles with narrow size distributions.



The amine group in OAm donates its lone pairs to  $Zn^{2+}$ , forming a Zn-OAm complex, preventing it from precipitation and increasing its availability to interact with  $P(DAM)_3$ . OAm coordinates to  $Zn^{2+}$  via its amine group in the complex, increasing the electron-withdrawing capability. The amine group partially withdraws electron density from  $Zn^{2+}$  by inductive effects, making it a stronger Lewis acid. It also stabilizes the transition state during the decomposition of the phosphorus precursor.



#### C.4.5 11-Mercaptoundecanoic acid (MUA)

MUA acts as a bifunctional negative ligand with:

- Thiol group (-SH): binds strongly to the metal surface of InP QDs.
- Carboxylic acid group (-COOH): provides a negatively charged ion when deprotonated due to high pH, providing stability in water.
- 11-Carbon alkyl chain: balances hydrophobicity and ensures colloidal stability<sup>16</sup>.

Thiol forms strong bonds with the QD surface. The negative charge creates repulsion between QDs, preventing aggregation in water.

#### C.4.6 Potassium nitrate

Potassium nitrate and potassium nitrite act as reactants for photocatalytic ammonia synthesis.

#### C.4.7 TMA

N,N,N-Trimethyl(11-mercaptoundecyl) ammonium chloride (TMA) acts as a cationic ligand for QDs with:

- Thiol (-SH): binds covalently to the surface of InP QDs via In-S bonds
- Quaternary ammonium group ( $-N^+(CH_3)_3$ ) provides a permanent positive charge
- 11-Carbon alkyl chain: balances hydrophobicity and ensures colloidal stability

It imparts a positive charge to the QD surface, which is critical for attracting anionic reactants.

<sup>16</sup> Colloidal stability is the ability of nanoparticles to remain uniformly dispersed without aggregating or settling out over time<sup>26</sup>

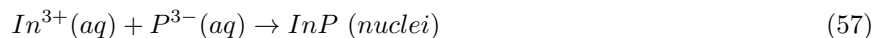
## C.5 Synthesis of Red Emitting InP Core QDs

### C.5.1 Mixing Procedure

1. In(III)Cl(100 mg, 0.45 mmol), ZnCl(300 mg, 2.2 mmol) and oleylamine (5.0 mL, 15 mmol) are combined in a three-neck round-bottom flask with a stir bar.
2. Heat it at 120°C under an Argon (Ar) atmosphere. This creates an inert atmosphere to prevent oxidation, and heating dissolves the precursors. Gently stir it until a clear solution is obtained.
3. Degas it at 120°C for about 60 minutes to remove volatile impurities and moisture, as InP is highly sensitive to oxidation, and the incorporation of water during synthesis<sup>27</sup>.

### C.5.2 Reaction at High Temperature

1. The temperature is raised to about 200°C.
2. 350μL of tris(dimethylamino)-phosphine (1.93 mmol) in 1.0 mL of Oleylamine was quickly injected.
3. The temperature was maintained at 200°C for 60 min. This allows controlled nucleation and growth of InP QDs.



Molarity of the tris(dimethylamino)-phosphine solution =  $\frac{\text{Number of moles of tris(dimethylamino)-phosphine}}{\text{Volume of Oleylamine}} = \frac{1.93 \text{ mmol}}{1.0 \text{ mL}} = 1.93 \text{ M}$

Number of moles of tris(dimethylamino)-phosphine injected = Molarity of the solution injected × Volume of solution injected = 1.93 M × 350 μL = 0.6755 mmol

### C.5.3 Quenching and Purification

1. Quenching with a water bath quickly lowers the temperature of the reaction system. Since the growth of QDs is a temperature-dependent process and requires high temperatures for atoms and molecules to collide, the molecular motion slows down when the temperature drops. Rapid cooling halts further growth, preserving the desired QD size.
2. Hexane is added. Hexane is a non-polar solvent that dissolves hydrophobic QDs (Oleylamine capped) but not ionic precursors and byproducts. Oleylamine hydrophobic tail interacts favorably with hexane.
3. The as-synthesized solution is centrifuged at 8000 rpm for 10 min to remove large aggregates/ unreacted solids. Denser unreacted precursors form a pellet at the bottom, whereas QDs stay dissolved in the hexane supernatant.
4. Ethanol is added to the solution. QDs (capped with hydrophobic ligands) are soluble in non-polar solvents but insoluble in polar solvents like ethanol, causing them to precipitate out of the solution. It isolates the QDs from the excess ligands, unreacted precursors, and other impurities that might remain after centrifugation.
5. Redispersion in toluene: Toluene is a good non-polar solvent for hydrophobic QDs and helps maintain their stability and optical properties.

## C.6 Ligand Exchange for Aqueous Dispersion

### C.6.1 Objective

The process aims to replace the hydrophobic Oleylamine ligands capped to QDs with charged, hydrophilic ligands like TMA<sup>+</sup> & MUA<sup>-</sup> for water solubility. The process is called Ligand exchange. This is essential for colloidal stability in aqueous medium, for water-based applications<sup>13</sup>.

### C.6.2 Procedure for [+]InP QDs

1. Dissolve TMA (50 mg) in water (2 mL). It is soluble in water due to its positively charged ammonium group.
2. Add 800 μL of OAm-capped InP QDs (in toluene).
3. Vigorously shake the solution for 5 min to ensure the mixing of the organic and aqueous phases and initiate ligand exchange. The thiol (-SH) group in TMA displaces weaker OAm ligands, coating the QD surface with TMA.
4. Add 1 mL of water and 10 mL of toluene.
5. The solution is stirred overnight. This will allow TMA ligands to replace OAm on QD surfaces and QDs to transfer from the toluene (organic) to the water (aqueous) phase.

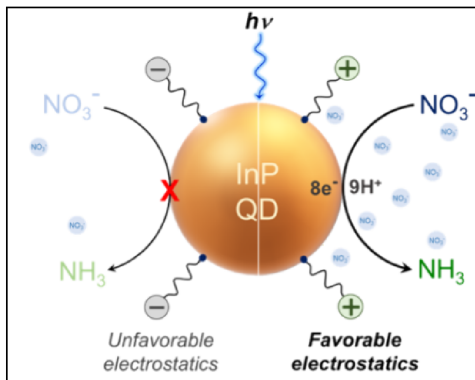


Figure 49: Schematics showing the regulation of catalyst (InP QD)-reactant ( $\text{NO}_3^-$ ) interactions through electrostatic forces emanating from QD surface ligands. A favorable catalyst-reactant interaction between [+] InP and  $\text{NO}_3^-$  ions enables efficient and selective  $\text{NH}_4^+$  formation.

Solvent	Dielectric constant (dimensionless) at room temperature ( $20^\circ\text{C}$ )
Water	78.4
Toluene	2.38
Acetone	20.7
2-Propanol	18.2

## 6. Purification:

- Separate the aqueous phase (contains [+] InP QDs) carefully.
  - Add 10 mL of 2-Propanol. It acts as a precipitating agent. Precipitation works by reducing the solubility of QDs in the solvent, causing them to aggregate and form a solid phase. The charged TMA+Cl- complex is highly water-soluble due to strong ion-dipole interactions with water. The addition of 2-propanol (less polar than water) weakens the water's ability to stabilize the charged QDs, resulting in a decrease in the solubility of the hydrophobic alkyl chains of the TMA ligands, driving precipitation. ( Acetone is avoided in this case as it may cause over-aggregation of [+] QDs, potentially compromising structural integrity.)
7. Centrifuge it to remove excess TMA and impurities.
- Redisperse it in water for stable [+] InP for photocatalysis.

### C.6.3 Procedure for [-]InP QDs

- Dissolve MUA (100 mg) in a 1:4 ratio of water: methanol (0.3 and 1.2 mL, respectively).
  - Adjust the pH to 10 using NaOH. It converts COOH to  $\text{COO}^-$  (negative charge) by fully deprotonating. Charged groups interact strongly with water molecules, making the QDs water-dispersible.
  - Add  $800\mu\text{L}$  parent InP QDs (in toluene)
  - Add 2 mL of water and 10 mL of toluene.
  - Stir the solution overnight to allow MUA to replace OAm ligands and QDs to transfer from the organic phase to the aqueous phase.
6. Purification:
- Separate the aqueous phase (contains [-] InP QDs) carefully.
  - Add 15 mL of Acetone. The charged MUA $\cdot\text{Na}^+$  complex is water soluble but forms less soluble ion pairs in acetone. Acetone acts as a dehydrating agent and effectively removes water molecules, solvating the  $\text{COO}^-$  groups, reducing solubility. Acetone achieves faster and more complete (compared to 2-propanol) for [-] InP QDs due to their much lower dielectric constant.
  - Centrifuge it to remove excess MUA ligands and impurities.
  - Redisperse it in water for stable [-] InP for photocatalysis.

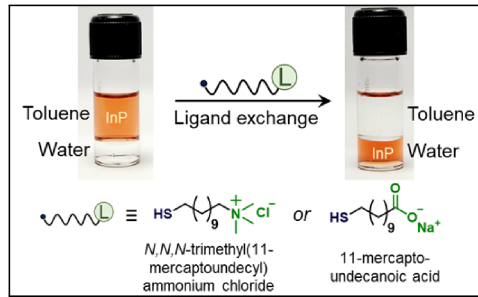


Figure 50: The native OAm ligands on InP QDs were place-exchanged with cationic TMA ligands to achieve colloidal stability in aqueous medium as well as to install favorable catalyst-reactant interactions. The successful transfer from toluene to water confirms complete ligand exchange.

## C.7 Quantum Yield Calculations

Apparent quantum yield,

$$AQY(\%) = \frac{\text{no. of } NH_4^+ \text{ formed} \times n_e}{\text{number of incident photons}} \times 100 \quad (58)$$

where,

$$\text{The number of electrons required to form a molecule of ammonia} = n_e = 8 \quad (59)$$

$$\text{The number of incident photons} = n_{photons} = \frac{P_0 \times \lambda(m) \times t(s)}{hc} \quad (60)$$

For  $\text{NO}_3^-$  to  $\text{NH}_4^+$ ,

$$P_0 = 200mW = 0.2J/s^{17} \quad (61)$$

$$\lambda(m) = 450 \text{ nm} \quad (62)$$

$$t(s) = 2\text{ hours} = 2 \times 60 \times 60s = 7200s \quad (63)$$

so,

$$n_{photons} = \frac{(0.2 \text{ J/s}) \times (450 \times 10^{-9} \text{ m}) \times (7200 \text{ s})}{(3 \times 10^8 \text{ m/s}) \times (6.626 \times 10^{-34} \text{ J.s})} = 3.26 \times 10^{21} \quad (64)$$

The number of product molecules formed was found to be  $5.90 \times 10^{18}$

so,

$$AQY_{450} = \frac{5.90 \times 10^{18} \times 8}{3.26 \times 10^{21}} \times 100 = 1.45\% \quad (65)$$

whereas, for  $\text{NO}_2^-$  to  $\text{NH}_4^+$ ,

$$t(s) = 1\text{ hour} = 3600s \quad (66)$$

$$n_{photon} = \frac{(0.2 \text{ J/s}) \times (450 \times 10^{-9} \text{ m}) \times (3600s)}{(3 \times 10^8 \text{ m/s}) \times (6.626 \times 10^{-34} \text{ J.s})} = 1.62 \times 10^{21} \quad (67)$$

The number of product molecules formed was found to be  $9.99 \times 10^{18}$ .

so,

$$AQY_{450} = \frac{9.99 \times 10^{18} \times 6}{1.62 \times 10^{21}} \times 100 = 3.7\% \quad (68)$$

## List of Figures

1	(a) Spectral distribution of solar radiation at the Earth's surface, showing the relative intensity across UV, visible, and IR regions. (b) Geographic distribution of nitrogen fertilizer demand in 2023, highlighting regions with the highest agricultural $\text{NH}_3$ consumption. The map uses color coding to indicate demand intensity (million tonnes/year). This rising demand underlines the urgent need for sustainable and decentralized $\text{NH}_3$ production routes.	2
2	Photoluminescence studies revealing the enhancement in PL intensity of core-only $[+]$ InP QD upon addition of 0.5 mM $\text{NO}_3^-$ ions.	3
3	Mechanism of visible-light-driven ammonia synthesis using InP QDs.	4
4	Overview of the experimental methodology for visible-light-driven nitrate reduction using InP QDs.	5
5	Bending of light by quartz	7

<sup>17</sup>assuming all incident photons are absorbed by the sample

6	(a–c) Ion chromatography calibration curves for (a) $\text{NH}_4^+$ , (b) $\text{NO}_3^-$ , and (c) $\text{NO}_2^-$ , respectively. Each plot was generated using standard solutions with varying concentrations. . . . .	7
7	(a–h) Ion chromatograms of photocatalytic reactions with varying InP QD concentrations (0.1, 0.3, 0.5, and 1.0 mol%). Each sub-figure shows cation or anion detection corresponding to the respective QD loading. (Note: The original article <sup>29</sup> does not report replicate number ( <i>n</i> ), error bars, or statistical analysis. For reproducibility, such details should be included in future studies.) . . . . .	8
8	(a) $\text{NH}_4^+$ concentration and $\text{NO}_3^-$ conversion vs. InP QD amount. (b)–(c) Cation and anion chromatograms for 0.25 mM $\text{KNO}_3$ . (d)–(e) Cation and anion chromatograms for 0.50 mM $\text{KNO}_3$ . (f)–(g) Cation and anion chromatograms for 0.75 mM $\text{KNO}_3$ . (h)–(i) Cation and anion chromatograms for 1.00 mM $\text{KNO}_3$ . (j) Total $\text{NO}_3^-$ conversion vs. $\text{KNO}_3$ concentration. (k) $\text{NH}_4^+$ yield vs. $\text{KNO}_3$ . (l) $\text{NH}_4^+$ peak growth with time. (m) $\text{NO}_3^-$ decrease over time. (n) Final product $\text{NH}_4^+$ concentration over 2 hours. . . . .	9
9	Temperature-based Heat map of India <sup>28</sup> . . . . .	10
10	(a) As the [+] InP QD film was made from an aqueous suspension, a water oxidation peak was observed at 0.65 V in addition to the peak corresponding to the valence band of [+] InP. The water oxidation peak was validated by recording the CV of the electrolyte in the water–acetonitrile mixture (green voltammogram). (b) Tauc plot of OAm-InP QDs. (c) Tauc plot of [+] TMA-InP QDs. . . . .	10
11	(a–d) Surface potential and ion concentration distributions near [+] and [-] InP QDs. (e–f) Anion chromatograms for $\text{NO}_3^-$ quantification with respective QDs. (g) Comparative $\text{NO}_3^-$ reduction efficiency under visible light (450 nm, 2 h). . . . .	11
12	(a–d) Control experiments highlighting the necessity of both light and [+] InP QDs for $\text{NH}_4^+$ generation. . . . .	11
13	(a) Ion chromatogram showing the formation of $^{15}\text{NH}_4^+$ from isotope-labeled $^{15}\text{NO}_3^-$ . (b) $^1\text{H}$ NMR spectra of $^{14}\text{NH}_4^+$ and $^{15}\text{NH}_4^+$ from photocatalytic reduction by [+] InP QDs. (c) Bar diagram comparing $^{14}\text{NH}_4^+$ and $^{15}\text{NH}_4^+$ , confirming $\text{NO}_3^-$ as the sole N source. . . . .	12
14	(a) Gas-phase mass analysis of standard $\text{NH}_3$ gas (conc. 101141 ppm). (b) Gas-phase mass analysis of photocatalytic reaction performed with [+] InP QDs and $\text{NO}_3^-$ . (c) Gas-phase mass analysis of photocatalytic reaction performed with [+] InP QDs and $\text{NO}_2^-$ . (d) Mass analysis of gases in the headspace after the photocatalytic reaction using $^{14}\text{NO}_3^-$ . <i>m/z</i> = 17 confirms presence of $^{14}\text{NH}_3$ . . . . .	12
15	Mass analysis of the gases in the headspace after the photocatalytic reaction was performed with $^{15}\text{NO}_3^-$ as the N-source. <i>m/z</i> = 18 indicate the presence of $^{15}\text{NH}_3$ in the gaseous phase from $^{15}\text{NO}_3^-$ . . . . .	13
16	(a) Cation chromatograms under 532 nm light (2 × 10 W LEDs, 200 mW/cm <sup>2</sup> ). (b) Anion chromatograms under 532 nm light (same conditions) (c) Cation chromatograms under 580 nm light (same conditions) (d) Anion chromatograms under 580 nm light (same conditions) (e) Action spectra showing $\text{NH}_4^+$ formation vs. wavelength with [+] InP QDs. Inset: Solar feasibility. . . . .	13
17	(a) IC for $\text{NH}_4^+$ quantification after photocatalytic reaction with [+] InP QDs under natural sunlight (2 h). (b) IC for $\text{NO}_3^-$ quantification after photocatalytic reaction with [+] InP QDs under natural sunlight (2 h). . . . .	14
18	Schematic representation of probable products formed during nitrate reduction . . . . .	14
19	(a) Analysis of common gaseous side product $\text{N}_2$ through mass spectrometry. (b) Analysis of isotopically labeled $^{15}\text{N}_2$ through mass spectrometry. . . . .	15
20	Analysis of the common gaseous side product NO through mass spectrometry . . . . .	15
21	8-Hydroquinoline . . . . .	16
22	(a) Absorption spectra of the reaction mixture with a known concentration (0–250 $\mu\text{M}$ ) of $\text{NH}_2\text{OH}$ . (b) Absorption spectrum of the reaction mixture after photocatalytic reduction of $\text{NO}_3^-$ to $\text{NH}_4^+$ with [+] InP QDs. . . . .	16
23	(a) Absorption spectra of the reaction mixture with a known concentration (0–3 ppm) of $\text{N}_2\text{H}_2$ . (b) Calibration plot obtained from absorption data. (c) Absorption spectrum of the photocatalytic reaction mixture consisting of [+] InP QDs and $\text{KNO}_3$ after 2 h of light irradiation. . . . .	16
24	(a) Cation ion chromatogram for the reaction mixture. (b) Anion ion chromatogram for the reaction mixture. The $\text{NO}_2^-$ peak disappeared completely, indicating 100% conversion. . . . .	17
25	(a) Cation ion chromatograms depicting the formation of $\text{NH}_4^+$ and conversion of $\text{NO}_2^-$ and $\text{NO}_3^-$ . (b) Anion ion chromatograms depicting the formation of $\text{NH}_4^+$ and conversion of $\text{NO}_2^-$ and $\text{NO}_3^-$ . No $\text{NO}_2^-$ accumulates as it is consumed. (c) Ion chromatograms for competitive photocatalytic experiments with an equimolar mixture of $\text{NO}_2^-$ and $\text{NO}_3^-$ as N-source. The asterisk marks $\text{Cl}^-$ ions. [+] InP QDs preferentially reduce nitrite over nitrate. . . . .	17
26	$^1\text{H}$ -NMR spectra for competitive photocatalytic experiments performed with an equimolar mixture of and $^{14}\text{NO}_2^- + ^{15}\text{NO}_3^-$ as the N-source, respectively . . . . .	18
27	(a) Schematics of energy level diagrams representing the thermodynamic feasibility of possible reduction reactions with [+] InP QDs. (b) Schematics of the proposed reaction mechanism for the visible-light photocatalyzed reduction of $\text{NO}_3^-$ to $\text{NH}_4^+$ by [+] InP QDs. . . . .	18
28	(a) Cation ion chromatogram in the absence of light after the addition of $\text{KNO}_3$ in the pre-irradiated reaction mixture containing [+] InP QDs. (b) Cation ion chromatogram in the presence of light after the addition of $\text{KNO}_3$ in the pre-irradiated reaction mixture containing [+] InP QDs. . . . .	19

29	(a)Ion chromatogram of reaction mixture purged with H <sub>2</sub> gas in absence of light. (b)Ion chromatogram of reaction mixture purged with H <sub>2</sub> gas in the presence of light. . . . .	20
30	(a)Cation ion chromatogram in the absence of light after the addition of KNO <sub>2</sub> to the pre-irradiated reaction mixture containing [+] InP QDs. (b)Cation ion chromatogram in the presence of light after the addition of KNO <sub>2</sub> to the pre-irradiated reaction mixture containing [+] InP QDs. . . . .	20
31	Betaine . . . . .	21
32	(a)Schematics showing the ligand exchange of InP QDs with non-thiolated betaine ligand. (b)Cation chromatograms comparing [+] -InP QDs in D <sub>2</sub> O and non-thiolated betaine-capped InP QDs with [+] -InP QDs in H <sub>2</sub> O. . . . .	21
33	Comparison of <sup>1</sup> HNMR under different reaction conditions performed with <sup>15</sup> NO <sub>3</sub> <sup>-</sup> as the N-source. . . . .	22
34	(a)Gas-phase mass analysis with <sup>15</sup> NO <sub>3</sub> <sup>-</sup> in D <sub>2</sub> O. <i>m/z</i> = 21 ( <sup>15</sup> ND <sub>3</sub> ) confirms water as proton source. (b)Gas-phase mass analysis with <sup>15</sup> NO <sub>3</sub> <sup>-</sup> in D <sub>2</sub> O. <i>m/z</i> = 19 ( <sup>15</sup> ND <sub>2</sub> ) supports deuterium incorporation. . . . .	22
35	Time-dependent absorption profile of [+] InP QDs in the photocatalytic reaction mixture. . . . .	23
36	(a)XPS spectra for as-synthesized OAm-InP QDs before the photocatalytic reaction. (b)XPS spectra for as-synthesized OAm-InP QDs before the photocatalytic reaction. (c)XPS spectra for [+] InP QDs before the photocatalytic reaction. (d)XPS spectra for [+] InP QDs before the photocatalytic reaction. (e) XPS spectra for [+] InP QDs after the photocatalytic reaction. (f)XPS spectra for [+] InP QDs after the photocatalytic reaction. . . . .	24
37	(a)Recyclability for NO <sub>2</sub> <sup>-</sup> conversion up to three cycles. (b)Recyclability for NH <sub>4</sub> <sup>+</sup> production up to three cycles. (c)Optical photographs of the InP QDs-loaded paper film after each cycle. (d)Anion chromatograms after each cycle. (e)Cation chromatograms after each cycle. . . . .	25
38	(a)Effect of ethanol (additional hole scavenger) on the photocatalytic activity. (b)Schematics of reduction and oxidation half-cycles with InP/ZnS QDs in the presence of ethanol. (c)Gas-phase mass analysis of the reaction was performed with ethanol. (d)Time-dependent absorption spectra of the reaction mixture with [+] InP/ZnS, KNO <sub>3</sub> , and ethanol. (e)Recyclability studies with a paper-based dip-catalyst system. . . . .	26
39	Schematic representation of the three major pathways involved in photocatalytic reduction of NO <sub>3</sub> <sup>-</sup> . . . . .	26
40	(a)Cation chromatograms showing the [+] InP photocatalyzed formation of NH <sub>4</sub> <sup>+</sup> from N <sub>2</sub> H <sub>2</sub> as the starting reactant. (b)Cation chromatograms showing the [+] InP photocatalyzed formation of NH <sub>2</sub> OH from N <sub>2</sub> H <sub>2</sub> as the starting reactant. . . . .	27
41	Band alignment in a semiconductor. . . . .	30
42	Two-step nucleation mechanism showing MSC intermediate pathway to InP QDs . . . . .	30
43	QD structure and size-dependent properties. . . . .	31
44	Structures of $\alpha$ -Ketoglutarate and Glutamate. . . . .	34
45	(a)UV-vis absorption spectra of GLDH assay proving the formation of glutamate in the presence of NH <sub>4</sub> <sup>+</sup> (in H <sub>2</sub> O) produced during the photocatalytic reaction. (b)UV-vis absorption spectra of GLDH assay proving the formation of glutamate in the presence of isotope-labeled <sup>15</sup> ND <sub>4</sub> <sup>+</sup> (in D <sub>2</sub> O) produced during the photocatalytic reaction. . . . .	35
46	(a)HRMS of glutamate formed from photocatalytically generated NH <sub>4</sub> <sup>+</sup> with [+] InP QDs and NO <sub>3</sub> <sup>-</sup> in H <sub>2</sub> O. (b)HRMS of isotope-labeled glutamate formed from <sup>15</sup> ND <sub>4</sub> <sup>+</sup> generated by reaction in D <sub>2</sub> O with <sup>15</sup> NO <sub>3</sub> <sup>-</sup> . (c)Schematic showing the photocatalytic reduction of <sup>15</sup> NO <sub>3</sub> <sup>-</sup> to <sup>15</sup> ND <sub>4</sub> <sup>+</sup> with [+] InP QDs in D <sub>2</sub> O. . . . .	35
47	(a)Basic overview (b)Analytical column (c)Suppressor (d)Sample chromatogram . . . . .	36
48	(a)P(DMA) <sub>3</sub> (b)Activated complex (c)OAm structure (d)MUA structure (e)TMA structure . . . . .	39
49	Schematics showing the regulation of catalyst (InP QD)-reactant (NO <sub>3</sub> <sup>-</sup> ) interactions through electrostatic forces emanating from QD surface ligands. A favorable catalyst-reactant interaction between [+] InP and NO <sub>3</sub> <sup>-</sup> ions enables efficient and selective NH <sub>4</sub> <sup>+</sup> formation. . . . .	42
50	The native OAm ligands on InP QDs were place-exchanged with cationic TMA ligands to achieve colloidal stability in aqueous medium as well as to install favorable catalyst-reactant interactions. The successful transfer from toluene to water confirms complete ligand exchange. . . . .	43

## List of Tables

1	Comparative analysis of InP QDs against other QDs.(Wavelength of the photon absorbed by the nanoparticles is given by: $\lambda = \frac{1240}{E_g}$ , where $\lambda$ and $E_g$ are the wavelength (nm) and band gap energy (eV), respectively.) . . . . .	3
2	Energy (eV) of photons with different wavelengths (nm) . . . . .	6
3	Variation in NH <sub>3</sub> production with different catalyst loading concentrations. (Original data didn't include error metrics; values represent mean observations) . . . . .	8
4	Variation in NH <sub>3</sub> production with different concentrations of KNO <sub>3</sub> <sup>+</sup> .(Original data did not include error metrics; values represent mean observations.) . . . . .	8

5	Table summarizing the reactions performed to identify the probable proton source and hole scavenger in the photocatalytic $\text{NO}_3^-$ reduction to $\text{NH}_3$ by [+] InP QDs. . . . .	22
6	Comparison of various photocatalysts and their respective performances. . . . .	27
7	Periodic table group numbering systems (modern vs. old) <sup>33</sup> . . . . .	29
8	Comparison of electronegativity, ionicity, and covalency for different QD materials <sup>12</sup> . . . . .	32

## References

- [1] AJEEL, F. N., MOHSIN, K. H., SHAKIER, H. G., KHAMEES, S. K., AND MUTIER, M. N. Theoretical insights into tunable electronic properties of graphene quantum dots through ZnO doping. *Chemical Physics Impact* 7 (dec, pages=100305 2023).
- [2] ALLEN, P., WALKER, B., AND BAWENDI, M. Mechanistic Insights into the Formation of InP Quantum Dots. *Angewandte Chemie International Edition* 49, 4 (jan, pages=760–762 2010).
- [3] ATHAYIL, M. P. The Role of Quantum Dots in Semiconductor Evolution. <https://orbitsky-line.com/blog/semiconductor-evolution-with-quantum-dots/>. Accessed on Sun, May 11, 2025.
- [4] BRYDEN, M. A., AND ZYSMAN-COLMAN, E. Organic thermally activated delayed fluorescence (tadf) compounds used in photocatalysis. *Chem. Soc. Rev.* 50 (2021), 7587–7680.
- [5] CHALLAGULLA, S., TARAFDER, K., GANESAN, R., AND ROY, S. All that glitters is not gold: A probe into photocatalytic nitrate reduction mechanism over noble metal doped and undoped  $\text{TiO}_2$ . *The Journal of Physical Chemistry C* 121, 49 (2017), 27406–27416.
- [6] CHAMOUSIS, R. L., AND OSTERLOH, F. E. Use of potential determining ions to control energetics and photochemical charge transfer of a nanoscale water splitting photocatalyst. *Energy Environ. Sci.* 7 (2014), 736–743.
- [7] COLEN, A. H. Transient-state kinetics of L-glutamate dehydrogenase: mechanism of -ketoglutarate inhibition in the burst phase. *Biochemistry* 17, 3 (1978), 528–533. PMID: 563727.
- [8] COLLADO, L., PIZARRO, A. H., BARAWI, M., GARCÍA-TECEDOR, M., LIRAS, M., AND DE LA PENA O SHEA, V. A. Light-driven nitrogen fixation routes for green ammonia production. *Chemical Society Reviews* 53, 23 (2024), 11334–11389.
- [9] CONTRERAS, E., NIXON, R., LITTS, C., ZHANG, W., ALCORN, F. M., AND JAIN, P. K. Plasmon-Assisted Ammonia Electrosynthesis. *Journal of the American Chemical Society* 144, 24 (jun, pages=10743–10751 2022).
- [10] CONTRIBUTORS, W. Thermal conductivity detector — Wikipedia, the free encyclopedia, 2025.
- [11] COOPER AJ, K. T. -ketoglutaramate: an overlooked metabolite of glutamine and a biomarker for hepatic encephalopathy and inborn errors of the urea cycle. *Metab Brain Dis.* (2014).
- [12] CRC. *CRC Handbook of Chemistry and Physics, 104th Edition* (2023), Section 9, Table of Electronegativity Values. CRC, 2024.
- [13] DEVATHA, G., ROY, S., RAO, A., MALLICK, A., BASU, S., AND PILLAI, P. P. Electrostatically driven resonance energy transfer in “cationic” biocompatible indium phosphide quantum dots. *Chemical Science* 8, 5 (2017), 3879–3884.
- [14] DOUDRICK, K., YANG, T., HRISTOVSKI, K., AND WESTERHOFF, P. Photocatalytic nitrate reduction in water: Managing the hole scavenger and reaction by-product selectivity. *Applied Catalysis B: Environmental* 136–137 (2013), 40–47.
- [15] D.S. FREAR, R. B. Spectrophotometric method for determining hydroxylamine reductase activity in higher plants. *Analytical Chemistry* (1665).
- [16] DÜMBGEN, K. C., LEEMANS, J., DE ROO, V., MINJAUW, M., DETAVERNIER, C., AND HENS, Z. Surface chemistry of InP quantum dots, amine–halide co-passivation, and binding of Z-type ligands. *Chemistry of Materials* 35, 3 (2023), 1037–1046.
- [17] EREN, G. O., SADEGHI, S., BAHMANI JALALI, H., RITTER, M., HAN, M., BAYLAM, I., MELIKOV, R., ONAL, A., OZ, F., SAHIN, M., OW-YANG, C. W., SENNAROGLU, A., LECHNER, R. T., AND NIZAMOGLU, S. Cadmium-free and efficient type-II InP/ZnO/ZnS quantum dots and their application for LEDs. *ACS Applied Materials & Interfaces* 13, 27 (2021), 32022–32030. PMID: 34196177.
- [18] FAHIEN, L. A., AND MACDONALD, M. J. The complex mechanism of glutamate dehydrogenase in insulin secretion. *Diabetes* 60, 10 (09 2011), 2450–2454.

- [19] FANG, Y., AND FLAKE, J. C. Electrochemical reduction of co<sub>2</sub> at functionalized au electrodes. *Journal of the American Chemical Society* 139, 9 (2017), 3399–3405. PMID: 28182409.
- [20] FONASH, S. J. Solar spectra.
- [21] GAN, G., HONG, G., AND ZHANG, W. Active Hydrogen for Electrochemical Ammonia Synthesis. *Advanced Functional Materials* (apr 2024).
- [22] GARCÍA DE ARQUER, F. P., TALAPIN, D. V., KLIMOV, V. I., ARAKAWA, Y., BAYER, M., AND SARGENT, E. H. Semiconductor quantum dots: Technological progress and future challenges. *Science* 373, 6555 (aug 2021).
- [23] GARY, D. C., TERBAN, M. W., BILLINGE, S. J. L., AND COSSAIRT, B. M. Two-Step Nucleation and Growth of InP Quantum Dots via Magic-Sized Cluster Intermediates. *Chemistry of Materials* 27, 4 (feb, pages=1432–1441 2015).
- [24] G.W. WATT, J. C. Spectrophotometric method for determination of hydrazine. *Analytical Chemistry* (1995).
- [25] HALDER, G., GHOSH, D., ALI, M. Y., SAHASRABUDHE, A., AND BHATTACHARYYA, S. Interface engineering in quantum-dot-sensitized solar cells. *Langmuir* 34, 35 (2018), 10197–10216. PMID: 29584956.
- [26] HIEMSTRA, G. Colloidal stability: Significance and symbolism. <https://www.wisdomlib.org/concept/colloidal-stability>. Accessed on Mon, May 19, 2025.
- [27] INSTITUTE, U. C. E. Synthesis of CdSe and InP Quantum Dots. <https://youtu.be/Fi055GP-Bof0?si=KA5vsx9CottQonnM>. Accessed on Mon, May 19, 2025.
- [28] ISRO, 2025.
- [29] JAIN, V., TYAGI, S., ROY, P., AND PILLAI, P. Ammonia Synthesis with Visible Light and Quantum Dots. *J Am Chem Soc* 146 (Nov 2024), 32356–32365.
- [30] KIM, S. H., MAN, M. T., LEE, J. W., PARK, K.-D., AND LEE, H. S. Influence of Size and Shape Anisotropy on Optical Properties of CdSe Quantum Dots. *Nanomaterials* 10, 8 (aug, pages=1589 2020).
- [31] KIM, Y., WILSON, A. J., AND JAIN, P. K. The Nature of Plasmonically Assisted Hot-Electron Transfer in a Donor–Bridge–Acceptor Complex. *ACS Catalysis* 7, 7 (may, pages=4360–4365 2017).
- [32] KUO, D.-Y., NISHIWAKI, E., RIVERA-MALDONADO, R. A., AND COSSAIRT, B. M. The role of hydrogen adsorption site diversity in catalysis on transition-metal phosphide surfaces. *ACS Catalysis* 13, 1 (2023), 287–295.
- [33] LEBRICOEUR64. Group (periodic table) - wikipedia. Accessed on Sat, May 17, 2025.
- [34] LI, L., CHEN, Y., XU, G., LIU, D., YANG, Z., CHEN, T., WANG, X., JIANG, W., XUE, D., AND LIN, G. &lt;p&gt; In vivo Comparison of the Biodistribution and Toxicity of InP/ZnS Quantum Dots with Different Surface Modifications&lt;/p&gt;. *International Journal of Nanomedicine Volume* 15 (mar, pages=1951–1965 2020).
- [35] LI, X.-B., LI, Z.-J., GAO, Y.-J., MENG, Q.-Y., YU, S., WEISS, R. G., TUNG, C.-H., AND WU, L.-Z. Mechanistic insights into the interface-directed transformation of thiols into disulfides and molecular hydrogen by visible-light irradiation of quantum dots. *Angewandte Chemie International Edition* 53, 8 (2014), 2085–2089.
- [36] LIN, H., LIU, Y., YANG, C., ZHAO, G., SONG, J., ZHANG, T., AND HUANG, X. Microfluidic artificial photosynthetic system for continuous nadh regeneration and l-glutamate synthesis. *Catal. Sci. Technol.* 12 (2022), 4057–4065.
- [37] MARUSAK, K. E., FENG, Y., EBEN, C. F., PAYNE, S. T., CAO, Y., YOU, L., AND ZAUSCHER, S. Cadmium sulphide quantum dots with tunable electronic properties by bacterial precipitation. *RSC Advances* 6, 80 (2016), 76158–76166.
- [38] MEDFORD, A. J., AND HATZELL, M. C. Photon-Driven Nitrogen Fixation: Current Progress, Thermodynamic Considerations, and Future Outlook. *ACS Catalysis* 7, 4 (mar, pages=2624–2643 2017).
- [39] MENG, S., LI, J., YE, C., YIN, Y., ZHANG, X., ZHANG, C., LI, X., TUNG, C., AND WU, L. Concurrent Ammonia Synthesis and Alcohol Oxidation Boosted by Glutathione-Capped Quantum Dots under Visible Light. *Advanced Materials* 36, 24 (mar 2024).
- [40] MIĆIĆ, O. I., NOZIK, A. J., LIFSHITZ, E., RAJH, T., POLUEKTOV, O. G., AND THURNAUER, M. C. Electron and hole adducts formed in illuminated inp colloidal quantum dots studied by electron paramagnetic resonance. *The Journal of Physical Chemistry B* 106, 17 (2002), 4390–4395.

- [41] NANOGRIFI. Indium Phosphide Quantum Dots: Advancements in Properties, Synthesis, and Applications - Nanografi. <https://shop.nanografi.com/blog/indium-phosphide-quantum-dots-advancements-in-properties-synthesis-and-applications-nanografi/>. Accessed on Sun, May 11, 2025.
- [42] NEXANTECA. Global ammonia market snapshot, 2024.
- [43] NIGUDKAR, G. 167. LAWS OF PHOTOCHEMISTRY (13). <https://madoverchemistry.com/2021/09/13/167-laws-of-photochemistry-13/>. Accessed on Thu, May 15, 2025.
- [44] PARK, Y. H., MURALI, G., MODIGUNTA, J. K. R., IN, I., AND IN, S.-I. Recent Advances in Quantum Dots for Photocatalytic CO<sub>2</sub> Reduction: A Mini-Review. *Frontiers in Chemistry* 9 (sep 2021).
- [45] PLAITALAKIS, A. The glutamate dehydrogenase pathway and its roles in cell and tissue biology in health and disease. *NLM* (2017).
- [46] POOLE, C. F. Conventional gas chromatography: Basic principles and instrumental aspects. In *Advanced Gas Chromatography in Food Analysis*. The Royal Society of Chemistry, 10 2019.
- [47] PRAKASH PREM, N. S. P., AND BHAUMIK, P. Structural basis for the catalytic mechanism and ketoglutarate cooperativity of glutamate dehydrogenase. *Journal of Biological Chemistry* (2018).
- [48] REMILLARD, S. Carrier Effective Mass in a Semiconductor, Lecture 10. <https://www.youtube.com/watch?v=rVeIvRStx8g>. Accessed on Fri, May 16, 2025.
- [49] REN, Y., YU, C., TAN, X., HUANG, H., WEI, Q., AND QIU, J. Strategies to suppress hydrogen evolution for highly selective electrocatalytic nitrogen reduction: challenges and perspectives. *Energy & Environmental Science* 14, 3 (2021), 1176–1193.
- [50] ROBEL, I., SUBRAMANIAN, V., KUNO, M., AND KAMAT, P. V. Quantum dot solar cells. harvesting light energy with cdse nanocrystals molecularly linked to mesoscopic tio2 films. *Journal of the American Chemical Society* 128, 7 (jan, pages=2385–2393 2006).
- [51] ROY, P., DEVATHA, G., ROY, S., RAO, A., AND PILLAI, P. P. Electrostatically driven resonance energy transfer in an all-quantum dot based donor–acceptor system. *The Journal of Physical Chemistry Letters* 11, 13 (2020), 5354–5360. PMID: 32539403.
- [52] ROY, P., VIRMANI, M., AND PILLAI, P. P. Blue-emitting inp quantum dots participate in an efficient resonance energy transfer process in water. *Chem. Sci.* 14 (2023), 5167–5176.
- [53] ROY, S., ROY, S., RAO, A., DEVATHA, G., AND PILLAI, P. P. Precise Nanoparticle–Reactant Interaction Outplays Ligand Poisoning in Visible-Light Photocatalysis. *Chemistry of Materials* 30, 23 (nov, pages=8415–8419 2018).
- [54] SIGMA-ALDRICH. Glutamate dehydrogenase assay kit.
- [55] SINGH, A. R., ROHR, B. A., SCHWALBE, J. A., CARGNELLO, M., CHAN, K., JARAMILLO, T. F., CHORK-ENDORFF, I., AND NØRSKOV, J. K. Electrochemical Ammonia Synthesis-The Selectivity Challenge. *A C S Catalysis* 7 (2017).
- [56] THERMO SCIENTIFIC. Introduction to fourier transform infrared spectroscopy.
- [57] THOMAS, A., SANDEEP, K., SOMASUNDARAN, S. M., AND THOMAS, K. G. How trap states affect charge carrier dynamics of cdse and inp quantum dots: Visualization through complexation with viologen. *ACS Energy Letters* 3, 10 (2018), 2368–2375.
- [58] TIAN, Y., AND TATSUMA, T. Mechanisms and Applications of Plasmon-Induced Charge Separation at TiO<sub>2</sub> Films Loaded with Gold Nanoparticles. *Journal of the American Chemical Society* 127, 20 (apr, pages=7632–7637 2005).
- [59] TIEN, J., TERFORT, A., AND WHITESIDES, G. M. Microfabrication through Electrostatic Self-Assembly. *Langmuir* 13, 20 (oct, pages=5349–5355 1997).
- [60] VIRIEUX, H., LE TROEDEC, M., CROS-GAGNEUX, A., OJO, W. S., DELPECH, F., NAYRAL, C., MARTINEZ, H., AND CHAUDRET, B. Inp/zns nanocrystals: coupling nmr and xps for fine surface and interface description. *Journal of the American Chemical Society* (2012).
- [61] WANG, J., YANG, R., LIU, Q., YANG, Y., AND WANG, X. Enhancing electrocatalytic ammonia synthesis through theoretical design of cluster catalysts supported on TiO<sub>2</sub> surface. *Materials Today Energy* 39 (jan, pages=101466 2024).

- [62] WANG, Z., RICHARDS, D., AND SINGH, N. Recent discoveries in the reaction mechanism of heterogeneous electrocatalytic nitrate reduction. *Catal. Sci. Technol.* 11 (2021), 705–725.
- [63] WEISS, E. A. Designing the Surfaces of Semiconductor Quantum Dots for Colloidal Photocatalysis. *ACS Energy Letters* 2, 5 (apr, pages=1005–1013 2017).
- [64] WIKIPEDIA CONTRIBUTORS. Debye length — Wikipedia, the free encyclopedia, 2025. [Online; accessed 4-July-2025].
- [65] WIKIPEDIA CONTRIBUTORS. Isotopic labeling — Wikipedia, the free encyclopedia, 2025. [Online; accessed 18-June-2025].
- [66] YAMAUCHI, M., ABE, R., TSUKUDA, T., KATO, K., AND TAKATA, M. Highly selective ammonia synthesis from nitrate with photocatalytically generated hydrogen on cupd/tio2. *Journal of the American Chemical Society* 133, 5 (2011), 1150–1152. PMID: 21204553.
- [67] YANG, W., WANG, J., CHEN, R., XIAO, L., SHEN, S., LI, J., AND DONG, F. Reaction mechanism and selectivity regulation of photocatalytic nitrate reduction for wastewater purification: progress and challenges. *J. Mater. Chem. A* 10 (2022), 17357–17376.
- [68] ZHANG, M., LIU, Z., WANG, J., CHEN, Z., JIANG, G., ZHANG, Q., AND LI, Z. Generating Long-Lived Charge Carriers in CdS Quantum Dots by Cu-Doping for Photocatalytic CO<sub>2</sub> Reduction. *Inorganic Chemistry* 63, 4 (jan, pages=2234–2240 2024).
- [69] ZUMDAHL, S. S. Haber-bosch process | definition, conditions, importance, & facts | britannica, 2024.